



Département de physique - Unité de recherche CESAM  
Group for Research and Applications in Statistical Physics

# Influence of the triboelectric effect on the flow of granular materials

Dissertation présentée par

**Nicolas Preud'homme**

en vue de l'obtention du titre de

**Docteur en Sciences**

Année académique 2023-2024

**Président:** Pr. Thierry Bastin

**Secrétaire:** Pr. Nicolas Vandewalle

Dr. Luisa Orozco

Pr. Thorsten Pöschel

Pr. Thomas Andrianne

**Promoteur:** Pr. Geoffroy Lumay

**Co-promoteur:** Dr. Eric Opsomer



# Acknowledgements

This PhD thesis is the final destination of a long road that has been a real challenge to travel to me. A road I started 5 years ago without really knowing where I would end up as I was literally throwing myself into the unknown. A problem on which I did not know many had already stumbled. The road has been long, strewn with obstacles, but there I am now and this would not have been possible without all the wonderful people that accompanied me since the beginning or that I met along the way. I would first like to thank my promoter, Geoffroy Lumay, who believed in me since the beginning. He punctuated my travel on this long road by his wise advices while letting me the freedom to go my way. I am grateful for the fact that he always encouraged me and pushed me to move forward. All of his advices naturally guided me to my final destination which makes me very proud. I would also like to thank him for looking after the positive working atmosphere I have experienced since my first day as a PhD student. I also had the chance to be supervised by Eric Opsomer who considerably helped me reach my objectives. He never hesitated to travel long stretches of this road by my side when there were challenges to overcome. His regular monitoring of my progress has been a great help. Some of the results I obtained during this thesis, which I am most proud of, would never have seen the light of day without his relevant comments and our long passionate discussions. I would also like to thank Nicolas Vandewalle and Stéphane Dorbolo from the lab. Professor Vandewalle's enthusiasm in every interaction we have had has been a great source of motivation for me. On the other hand, Professor Dorbolo, with his experience and clear vision of physics, sparked my curiosity and inspired many intriguing ideas. I also want to thank all my current colleagues—Florence, Thomas, Cyril, Joséphine, Megan, Adrien, Matteo, Martial, and Christophe—as well as those who have moved on: Salvatore, Jean, Nathan, Ylona, and Sébastien. Each of you contributed to a pleasant atmosphere in the lab and supported me with his own sharp knowledge of physics. I am finally thankful to the Members of the Jury, Professor Bastin, Professor Vandewalle, Doctor Orozco, Professor Pöschel and Professor Andrianne who accepted to review this thesis and travel hundreds of kilometers to attend the defense.

As you will see, this thesis is almost entirely based on numerical simulations. To generate only the results presented in this thesis, if the simulations were run successively one after the other, a total of more than 30,000 hours—or approximately 3,5 years—of continuous simulation time would have been required. I would definitely not have reached my objectives without the computational resources provided by the Consortium des Équipements de Calcul Intensif (CÉCI).

I certainly could not have got this far without all the people who mean the most to me and have been supporting me from the start: my friends and family. Thank you Thomas, Alix, Grégoire, Élixa and our little *piou-piou* Ambre for all the moments of joy and laughter we have shared together that allowed me to escape for an evening or a weekend to refocus and start afresh. Thank you to my exceptional family-in-law Alain, Anne, Julie, Jérôme, Auguste and Margot for your endless support and interest in everything I undertake. Thank you to my wonderful family, dad, mum, Youyou, Mimi and Kek simply for everything. You are the reason why I became the person I am today and I would not be where I am now without you. I am immensely thankful for everything you have done for me. Finally, the only one who helped me go through every ups and downs, the only one who knows how to cheer me up, the only one who brightens my days with her smile, the only one I look forward to seeing every evening when I come home, my wonderful wife.

*This one's for you, my little boy.*





---

# Contents

---

<b>1</b>	<b>Introduction</b>	<b>13</b>
<b>2</b>	<b>State of the art</b>	<b>18</b>
2.1	The triboelectric effect . . . . .	18
2.1.1	History . . . . .	18
2.1.2	Triboelectric series . . . . .	24
2.1.3	Asymmetry of rubbing and the effect of size . . . . .	25
2.1.4	Role of trapped electrons . . . . .	28
2.1.5	Patch model . . . . .	30
2.1.6	Capacitor model . . . . .	33
2.1.7	Role of strain . . . . .	34
2.1.8	Role of ions and humidity . . . . .	35
2.2	Granular materials . . . . .	38
2.2.1	Solid phase . . . . .	39
2.2.2	Gaseous phase . . . . .	45
2.2.3	Liquid phase . . . . .	49
2.3	Granular flow in a rotating drum . . . . .	54
2.3.1	Flow regimes . . . . .	54
2.3.2	Velocity profiles and angle of flow . . . . .	55

2.3.3	End walls effect . . . . .	59
2.3.4	Influence of cohesion . . . . .	59
2.3.5	Mixing/segregation . . . . .	62
<b>3</b>	<b>Motivations</b>	<b>64</b>
<b>4</b>	<b>Numerical simulations</b>	<b>67</b>
4.1	The Discrete Element Model (DEM) . . . . .	68
4.1.1	Normal force / repulsion . . . . .	68
4.1.2	Tangential force / friction . . . . .	70
4.1.3	Rolling friction . . . . .	71
4.1.4	Spinning friction . . . . .	73
4.1.5	Displacement of the grains . . . . .	74
4.2	Tribocharging . . . . .	76
4.3	Analysis of granular flow . . . . .	81
<b>5</b>	<b>Influence of cohesion on granular flow</b>	<b>84</b>
5.1	Motivations . . . . .	85
5.2	Results . . . . .	87
5.3	Conclusions . . . . .	99
5.4	Toy project: the recoater . . . . .	100
<b>6</b>	<b>The triboelectric effect in granular materials</b>	<b>104</b>
6.1	Motivations . . . . .	105
6.2	Results . . . . .	106
6.2.1	Mono-disperse granular materials . . . . .	106
6.2.2	Bi-disperse granular materials . . . . .	110
6.2.3	Different materials tribocharging . . . . .	116
6.3	Conclusions . . . . .	126
<b>7</b>	<b>Influence of electrostatic charges on granular flow</b>	<b>129</b>
7.1	Motivations . . . . .	130
7.2	Results . . . . .	131
7.3	Conclusions . . . . .	136



<b>8</b>	<b>Influence of grain shape on granular flow</b>	<b>139</b>
8.1	Motivations . . . . .	140
8.2	Experimental setup . . . . .	140
8.3	Results . . . . .	142
8.4	Conclusions . . . . .	144
<b>9</b>	<b>Conclusions and perspectives</b>	<b>145</b>



# Publications

**Nicolas Preud'homme**, Eric Opsomer and Geoffroy Lumay. Tribocharging of granular materials in grounded inclined tubes. *Soft Matter*. (Submitted)

**Nicolas Preud'homme**, Geoffroy Lumay, Nicolas Vandewalle and Eric Opsomer. Tribocharging of granular materials and influence on their flow. *Soft Matter*, 19(45):8911–8918, 2023.

**Nicolas Preud'homme**, Geoffroy Lumay and Eric Opsomer. Numerical analysis of cohesive granular materials' flow. *Belgian Journal of Physics*, 2022.

**Nicolas Preud'homme**, Geoffroy Lumay, Nicolas Vandewalle and Eric Opsomer. Numerical measurement of flow fluctuations to quantify cohesion in granular materials. *Physical Review E*, 104(6):064901, 2021.

**Nicolas Preud'homme**, Eric Opsomer, Nicolas Vandewalle and Geoffroy Lumay. Effect of grain shape on the dynamics of granular materials in 2D rotating drums. *EPJ Web of Conferences*, 249:06002, 2021.

**Nicolas Preud'homme**, Aurélien Neuveu, Filip Francqui, Eric Opsomer, Nicolas Vandewalle and Geoffroy Lumay. Simulating powder bed based additive manufacturing processes: from DEM calibration to experimental validation. *ECCOMAS Congress*, 2020.



---

# 1 Introduction

---

Granular materials include a large variety of materials. Their only defining characteristic is that they are composed of large agglomerations of macroscopic particles [1]. Sand, corn kernels, rocks or even asteroids are all considered as granular materials. The term powder is also sometimes used to refer to such materials. Powders are granular materials except that they represent a class of granular materials whose particles are commonly smaller. The reason why we gather such a broad variety of materials together is because they all seem to have the same properties when observed at the appropriate scale. This is illustrated in figure 1 which shows that sugar, pepper seeds and rocks all seem to flow similarly out of a container on different scales. Even though these materials are very different in density, roughness or shape, they just look like identical large agglomerations of macroscopic particles which makes them granular materials by definition.

This common feature is highly interesting from a physical perspective as theories and interpretations derived from one type of granular material can be transposed and scaled to other types of granular materials. Physicists that are doing experiments on glass beads, sand or flour in laboratories are not investigating the properties of that specific granular material but rather the properties of every granular material simultaneously as the results they obtain apply for all of them.

The terms granular materials are thus widely employed in the physics community as they refer to a vast diversity of materials that all share the same physical properties.



**Figure 1:** Granular materials at different scales. From left to right: sugar, pepper and rocks flowing out of a container. Illustrations generated using Bing Image Creator.

Granular materials are found in many different natural environments such as landslides, avalanches, dunes or asteroid belts but they are also ubiquitous in our everyday lives. Among all the different materials that Man handles, granular materials are the second most handled one after water [2]. We find them in almost everything we eat with for example flour, sugar, coffee or powdered milk. In agriculture, fertilizers are in the form of granular materials, as are all the products of this sector, such as corn or potatoes. Subsequently, all the factories involved in post-processing must store these granular materials in silos or packages, transport them, and, in some cases, convey them using pneumatic conveyors. These seemingly simple operations turned out to be very challenging when implemented for granular materials and required extensive research. In construction, the massive use of concrete cannot be dissociated from other types of granular materials: sand and gravels. In the pharmaceutical industry, excipients and active ingredients are mostly granular materials that need to be mixed and compacted very precisely for encapsulation and tableting. The recent progresses in the pharmaceutical industry with dry powder inhalers (DPI) would also not have been possible without in-depth knowledge of granular materials.

All the research on granular materials also paved the way to innovative high-precision manufacturing techniques such as selective laser melting (SLM).

The SLM is a sort of 3D printing technique consisting in melting locally a metallic powder layer after layer using a laser. This technique can be used to produce small and very complex metallic parts without generating any waste as the unused powder can be recycled for further use. Engineering also led to groundbreaking applications with granular materials such as powder coating that allows us to create highly durable and customizable finishing layers on metallic parts. In recent years, automotive engineering has had to address the challenges posed by granular materials, particularly because lithium carbonate, the main component of electric vehicle batteries, is a powder.

This non-exhaustive list just gives a glimpse of all the applications of granular materials and demonstrates why so much effort has been put in understanding granular materials over the last decades. Indeed, each of these situations is difficult to interpret because complex phenomena (which will be part of this thesis' state of the art) occur in each of them. Studies on granular materials consider in most cases simple model systems with ideal granular materials *i.e.* made of hard and spherical particles that do not interact with each other. As will be shown later in this thesis, the physics of these granular materials is relatively well understood to date and has provided helpful information on our understanding of granular materials. However, the behavior of real granular materials is significantly influenced by many parameters such as the particles' roughness, size, shape or softness and the effect of these parameters makes the dynamics of granular materials even more complex. In particular, cohesive granular materials represent a large amount of granular materials found in many applications and have really specific flowing properties. Cohesive granular materials are characterized by an attraction between the particles which leads for instance to the formation of aggregates as shown in figure 2. The most common cohesive granular materials in our everyday life are flour, cornstarch or powdered sugar but they are also present in all of the sectors cited above.

When a granular material is saturated in humidity, some liquid bridges can appear between the particles and be responsible for cohesion. But in dry granular materials, the reason why some materials are cohesive is not clear. Van der Waals interaction, the very short range interaction between particles, has been proposed. Static electricity that appears when two objects are rubbed against each other



**Figure 2:** A spoon of non-cohesive granular material (sugar, left) compared to a cohesive granular material (cornstarch, right). Aggregates can be observed when the material is cohesive. Taken from [stock.adobe.com](https://www.stock.adobe.com).

has also been pointed out as another possible cohesive force. However, the mechanisms of this effect, called the triboelectric effect, are not fully understood. As a consequence, what creates cohesion in granular materials and what influences it still needs to be clarified and this is the motivation of this thesis.

This thesis concentrates on analyzing the flow of cohesive granular materials and exploring the potential relationship between cohesion and the triboelectric effect. This effect is frequently observed in different scenarios but still remains unexplained. Therefore, this effect was chosen as the focus of this study. Numerical simulations were employed to investigate the flow of cohesive granular materials, specifically in a rotating drum geometry, which will be discussed in detail. The decision to primarily utilize numerical simulations in this work stems from their capacity to provide extensive freedom for testing and analyzing theories and parameters.

In section 2.1, the research that has been done on the triboelectric effect from Antiquity since now is reviewed. By the end of this section, all the experiments and misconceptions that lead to our current knowledge of this effect will be explained and the reason why it is still debated should be clear. In the following section 2.2, what is known about ideal granular materials is reviewed. A more specific section 2.3 then focuses on the existing theories on the flow of granular materials. With these three sections, the scene will be set to start the investigation of this thesis' subject **How does the triboelectric effect influence the flow of granular materials?** The methods used for the numerical simulation of flowing granular



materials are described in section 4 and the results I obtained using the simulations are presented in the following sections 5 to 7. Experimental results obtained while making a brief aside on the influence of the particles' shape on the flow of granular materials are finally presented in section 8.

---

## 2 State of the art

---

### 2.1 The triboelectric effect

#### 2.1.1 History

The first observation of the triboelectric effect dates back to Antiquity, at the time when amber (*i.e.* fossilized tree resin, see figure 3) was used in jewelry. People observed that these amber stones that were embedded in their jewels were often covered with dust. Women in Syria also used amber on their spindles to help



**Figure 3:** Amber was used in Antiquity in jewelry and for ornamentation. It is at the origin of the *amber effect* which was observed when amber was rubbed against fur and could then attract light objects. Illustration from [romadesignerjewelry.com](http://romadesignerjewelry.com).

them attract the light fringes of tissues for yarn spinning [3]. Even though there exists no written proof of it, the first observation of the *amber effect* is attributed to Thales around  $\sim 600$  BC [3, 4]. He was indeed the first to state that amber can attract light objects if it has been rubbed with fur. The amber effect could thus explain why people's jewels made of amber were covered with dust as they could accidentally rub their jewels against the fur they were wearing. At this time, the explanation of this effect relied on the belief that objects possessed a soul or inherent state that would naturally give them an attractive or repulsive power. Thus, the attraction of light objects by amber and the magnetic attraction of small pieces of iron by lodestone (naturally magnetized iron ore) were understood in a similar manner. Throughout the Middle Ages, people continued exploring the amber effect by rubbing different materials. They observed that different degrees of attraction could be obtained depending on the materials they were rubbing but they could still not provide any other more scientific interpretation to this phenomena.



**Figure 4:** The *versorium*, William Gilbert's instrument used to test the attraction and repulsion of objects charged by friction. By electrostatic induction, the metallic needle points to a charged object. Taken from [5].

A significant step towards the understanding of the amber effect has been made by English physicist William Gilbert in his work published in 1600 entitled *De Magnete*. Initially interested in the Earth's magnetic field, Gilbert clarified the distinction between the amber effect and magnetism using the first ever electroscope in history which he designed, the *versorium*. This instrument, shown in figure 4, consists in a metallic needle which is allowed to pivot freely on a support. Gilbert observed that an amber stone that had been previously rubbed attracted the needle, like any other materials that he had rubbed such as glass. It was not the case for the naturally magnetized lodestone that has North and South poles. Depending on the orientation of the magnetized stone, he could observe that the needle was attracted

or repelled. He managed to show this way that magnetic and electrostatic effects were not similar and was the first to use the term *electricity* which is derived from *elektron*, the Greek word for amber.



**Figure 5:** Otto Von Guericke holding a sulphur globe he charged by rubbing and used to test the interaction with different objects. Objects were initially attracted by the globe but then repelled if they touched it. Taken from [6].

A few decades later, around 1660, Otto Von Guericke made pioneering discoveries about air pressure and vacuum, which also led him to explore electrostatics. In his famous experiment, *the Magdeburg hemispheres*, Von Guericke created a globe by assembling two sulfur hemispheres and then used the first-ever vacuum pump, which he invented, to pump the air out of the globe. To demonstrate the power of atmospheric pressure, he attached the two hemispheres to four horses each, trying to pull them apart. This sulphur globe then captured his attention as it could attract objects if it was rubbed, similarly to amber. He attached the globe on a shaft so that he could carry it close to objects as shown in figure 5. He observed that if an object that is initially attracted by the globe touches the globe, it is then repelled. The object is attracted again by the globe if it touches the ground, a finger or another object. While Gilbert denied the existence of electrostatic repulsion because he could not observe it with his instrument, Von Guericke experimented it for the first time. He also saw and heard that *electricity* Gilbert was talking about and which was responsible for the interaction between objects as he saw sparks in the dark at the discharge, and heard their crackling noise once rubbing objects on the globe [6]. In 1660, Von Guericke's work triggered every physicists' curiosity...

In 1730, Charles François de Cisternay du Fay did new experiments on rubbed objects and their mutual interaction. He also observed, like Von Guericke, that some objects were repelled and others attracted. He used this criterion to classify objects in two categories. Objects could be electrified either with a *vitreous* electricity (e.g. glass, crystal or precious stones) or with a *resinous* electricity (e.g. amber, silk or paper). Objects that are electrified with vitreous electricity attract objects that are electrified with resinous electricity and repel those that are charged with the same vitreous electricity [7]. According to du Fay, those two electric fluids are separated by frictional forces and neutralise when they recombine by flowing between objects [8]. His theory was then called the two-fluid theory of electricity.

Du Fay's two-fluid theory was rapidly replaced around 1747 by Benjamin Franklin's one-fluid theory of electricity. The development of this theory would however not have been possible without the invention of the Leyden jar the year before. Convinced that electricity was a fluid that could flow from one object to another, Ewald Georg von Kleist and Pieter van Musschenbroek (professor at Leiden University, hence *Leyden jar*) used a glass bottle filled with alcohol to store electricity. Using an electrostatic generator like the one of von Guericke, they could charge the bottle through a nail that was inserted in the cork as shown in figure 6. They observed that electricity could be collected and kept inside the bottle. Both of them received severe shocks while experimenting but could not explain why.

Interested in the processes of charging and discharging objects, Benjamin Franklin made extensive use of Leyden jars for his experiments. He demonstrated that electricity was actually not two but one single fluid that could flow between objects and be held by objects in different quantities. A neutral object has a "normal" quantity of fluid. If it has an excess of this fluid, it is called "plus" (referring to the excess of liquid) and if it has less than normal liquid, it is called "minus" [9]. This one-fluid theory of electricity can be applied to explain the charging of Leyden jars. By charging the bottle, the inner part becomes positive while the outside of the bottle becomes negatively charged, assuming that glass

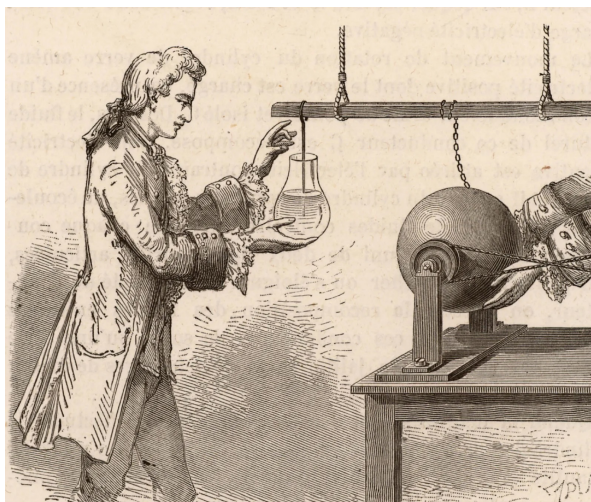


**Figure 6:** Pieter van Musschenbroek charging a Leyden jar using an electrostatic generator similar than the one of von Guericke. Illustration from [britannica.com](http://britannica.com)

is completely impermeable to electricity. When a person touches the two parts of the bottle, it allows the fluid to flow back through the body from where it is in excess to where it is in deficit and neutralise. The Leyden jar also helped him demonstrate that lightning is a form of electricity through his famous kite-flying experiment during a storm. By connecting a conducting kite to a Leyden jar, he showed that the jar charged similarly to how it would with an electrostatic generator, indicating that electricity flows from the clouds to the ground during lightning.

A few years later, in 1785, Charles Augustin de Coulomb explained how charged objects interact using his famous Coulomb's law. With this law, Coulomb introduced a new unit of electrical charge, now known as the Coulomb, and demonstrated that the repulsion or attraction between charged objects is proportional to the quantities of charge they carry.

Benjamin Franklin is also responsible for the invention of the first electric battery by connecting several Leyden jars together as shown in figure 7. Doing so, he observed that he could store a stronger charge and increase the power available on discharge.




**Figure 7:** The first electric battery invented by Benjamin Franklin who connected multiple Leyden jars together to increase the amount of electricity stored. Illustration from [benfranklin300.org](http://benfranklin300.org).

From that moment, and following Franklin's invention of the battery, the study of the triboelectric effect—the modern term for the phenomenon responsible for the transfer of charges by rubbing (derived from the Greek *tribo-* meaning "to rub" and *elektron* meaning "amber")—and the study of electricity diverged into separate paths. Indeed, with the evolution of the battery by Volta around 1800 based on electrochemistry, electrostatic generators were not used anymore to generate electricity as they were less reliable. The development of electromagnetism took most scientists' attention and reached its climax around 1860 with the development of Maxwell's laws of electromagnetism and Faraday's electric generator. In the late 19th century, Thomson unveiled the electron, a fundamental particle bearing a negative charge. Shortly thereafter, Rutherford's investigations led to the discovery of the proton, its positively charged counterpart. It is now clear that charged particles are transferred between objects rather than a fluid. In the meantime, very little investigation on the triboelectric effect has been done so we have to jump to the beginning of the twentieth century for the first detailed analysis of the triboelectric effect.

2.1.2 Triboelectric series

The twentieth century saw the emergence of triboelectric series which are ordered lists of materials that give the charge a material would obtain if it were rubbed against another one in the list. For example, in the lists shown in table 1 that have been published by different authors, materials that charge positively are at the top of the list. According to Wilcke for example, if wool is rubbed against paper, wool charges positively and paper charges negatively as wool is higher in the list than paper. But if wool is rubbed against glass, now wool charges negatively and glass charges positively. The triboelectric series are empirically determined and somewhat controversial, as different orderings can be observed for materials such as wood, as shown in Table 1. The first observation of identical materials tribocharging by Shaw [10] also questioned the relevance of triboelectric series as they only consider charge transfers between different materials, located at different positions in the serie.

Wilcke (1759)	Faraday (1840)	Jamin and Bouty's "Physique" (1891)	Shaw (1917)
Glass	Cat's fur	Cat's fur	Glass
Wool	Wool	Glass	Wool
Quills	Quills	Wool	Cat's fur
Wood	Flint glass	Feathers	Pb
Paper	Cotton	Wood	Silk
Ground glass	Linen	Paper	Paper
Pb	Silk	Silk	Cotton
Sulphur	Hand	Resin	Wood, Fe
Metals	Wood	Ground glass	Ground glass
	Fe, Cu, Ag, Pb		Resin
	Sulphur		Cu, Ag
			Sulphur



**Table 1:** Triboelectric series obtained at different times. Materials at the top of the list charge positively (indicated by the red arrow) if rubbed against a material that are below in the list that consequently charge negatively (indicated by the blue arrow). Reproduced from [11].



### 2.1.3 Asymmetry of rubbing and the effect of size

The experiment performed by Shaw in 1926 where same-materials tribocharging has been observed consisted in rubbing two rods of ebonite (*i.e.* a sort of hard plastic made of rubber) that were cut from the same piece to ensure that the rods were perfectly identical. Using a gold-leaf electroscope, he showed that both pieces were charged oppositely. More interestingly, he observed that the way the rods are rubbed influences their charge. When rubbing the rod A on the rod B as shown in the left panel of figure 8, he observed that A charges positively while B charges negatively. If B is rubbed on A as shown in the right panel of figure 8, then A charges negatively and B charges positively. He concluded that in any case, when two identical materials are rubbed, the rubber charges + and the rubbed object charges -. Similar observations were reported later by Henry [12]. Both Henry and Shaw proposed that heat gradient could cause a migration of charge from one object to the other as the one with the smallest area of contact would be hotter than the other one with a much larger surface of contact.

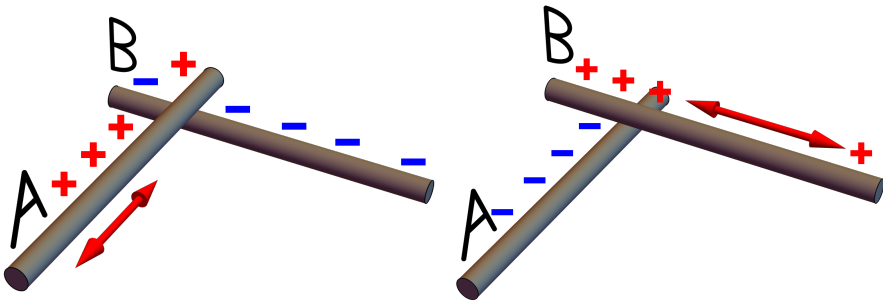


**Figure 8:** Asymmetric rubbing of two identical rods to show that the way identical materials are rubbed influences their final charge. On the **left**, the rod A is rubbed on the rod B. A is the *rubber* and B is the *rubbed* rod. The surface of contact of B is much smaller than the surface of contact on A. On the **right**, B is the *rubber* and A is the *rubbed* rod. The surface of contact of A is much smaller than the surface of contact of B. *Rubber* always charge + while *rubbed* charge - [10].

When measuring the charge of the rods, it was also observed that the charge evolves with the time of rubbing [10]. After just a few strokes, the rubber charges negatively and the rubbed charges positively, opposite to what has just been discussed. However, by continuing rubbing, the objects gradually lose

their charge to become neutral and then eventually change sign to become positive for the rubber and negative for the rubbed. If rubbing is temporarily stopped when the objects are in the neutral condition, one further stroke could charge the rubber + then the following stroke in the opposite direction charges it −.

The observations reported concerning the tribocharging of identical materials raised many questions. In particular, parallels were being made between the charging of identical materials and the charging of dust [10]. Indeed, during dust storms, lightning occurs as a consequence of important particles charging [13,14]. Similar observations were reported in volcanic ash plumes where lightning can also occur because of the charging of volcanic clouds [15–17]. As dust particles are mostly identical in composition, the fact that identical materials could charge because of the triboelectric effect provides a possible explanation to this phenomenon. Studies on dust devils revealed that they were carrying strong vertical upward electric fields [18]. Considering that smaller particles are lifted higher because of their reduced weight while large particles remain close to the ground, the particles' size also seems to have an influence on charging.

Many experiments have then shown the bipolar charging of granular materials. The device that is frequently used to show it is the electrostatic separator. It consists in two vertical electrodes between which the granular material is allowed to fall. If the particles are charged, they are deviated towards the oppositely charged electrode. The granular material must be charged prior to inserting it in the separator and the interaction between the particles and the container must be avoided. To do so, a gas is injected in the granular material to create a fountain-like flow. This way, only particle-particle interaction might occur. The charged particles are then transferred to the separator using another flow of gas. This setup has been used multiple times to show that large particles tend to charge positively and small particles tend to charge negatively in granular mixtures [19–21] which is consistent to what has been observed with dust devils. The charge of the particles is measured using Faraday cups that are placed at the bottom of the electrodes [19,21] as shown in the left panel of figure 9 or by tracking the deviation of the particles due to the electrodes' electric field using a free-falling camera [20] as shown in the right panel of figure 9.

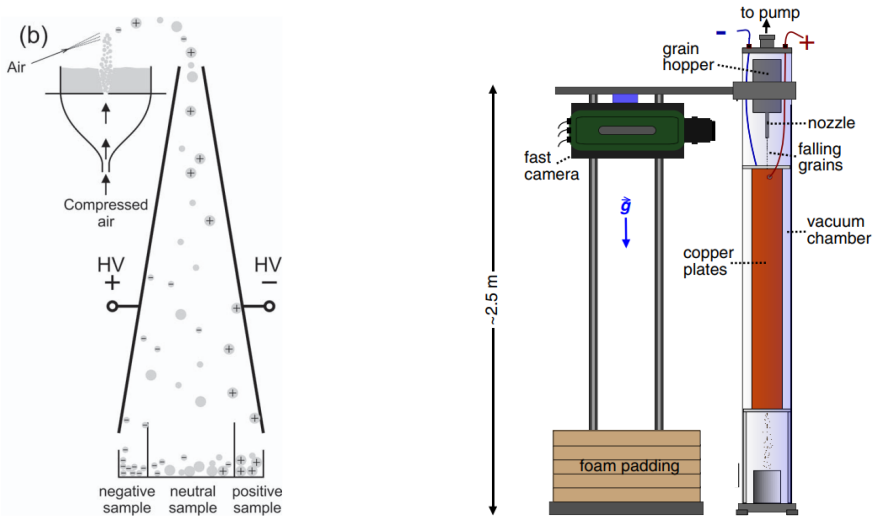


**Figure 9:** Electrostatic separators used to investigate the bipolar charging of granular materials where small particles tend to charge negatively and large particles tend to charge positively. Both devices consist of two vertical electrodes between which a charged granular material is allowed to flow. **(Left)** electrostatic separator with Faraday cups at the bottom for the measurement of the particles' charge [19]. **(Right)** electrostatic separator using a free-falling camera to track the deviation of the particles in the electric field and measure their charge [20].

Forward *et al.* [22] use a different device to study bipolar charging of granular materials. They place a copper plate covered with an isolating parafilm and held at a positive or negative voltage above the air-fluidized granular material to collect the charged particles. An optical microscope is then used to take pictures of the collected particles and determine their diameter. Zhao *et al.* [23] also use a slightly different electrostatic separator consisting in a vertical array of Faraday pails but still obtains the same characteristic charging of small and large particles.

These experiments on bi-disperse granular materials and asymmetric rubbing give important insight into same-materials tribocharging. We can summarize these observations by stating that when two identical objects are rubbed asymmetrically or when large and small particles are mixed together, the objects with the largest surface area of contact become positively charged, while those with a smaller surface area of contact become negatively charged. The effect of size and the

effect of the asymmetry of rubbing can thus be regarded similarly [24] and both effects seem to indicate that same-materials tribocharging is dictated by some surface effects.

### 2.1.4 Role of trapped electrons

One way to explain the tribocharging of identical insulators and the effect of the surface of contact can be found in solid-state physics. Looking at the electronic band structure of insulators tells us that ideal insulators are characterized by a filled valence band (low energy electronic states) and an empty conduction band (high energy electronic states). The valence and conduction bands are separated by a large energy gap that make it impossible for electrons from the valence band to be transferred to a conduction state under normal conditions. A real insulator however has defects, *trapped states*, in the band gap that are partially occupied by electrons as shown in figure 10. Those trapped electrons are in non-equilibrium states but can still remain in those states for very long times (from days to centuries) [25] without external excitation (heat typically). It is by the way by thermoluminescence experiments that the presence of trapped electrons has been demonstrated [26]. When rubbing two insulators against each other, those electrons on higher energy states have the opportunity to reach an empty lower energy and thus more stable state on the other object [27]. Indeed, at contact between the two objects, a trapped electron at the surface of the first object will eventually be in close proximity of a vacant lower energy state on the surface of the other object as shown in figure 10. The electron will spontaneously tunnel to this lower energy state and reach equilibrium.

If the two objects in contact are infinite planes, there is no net transfer of charge between them. Indeed, as the two objects are identical, they have the same surface densities of trapped electrons so there are as many transfers in one direction as in the other. If the rubbing is asymmetric like in figure 8, then the object with the smaller surface of contact can only lose a few electrons that are in trapped states in that small area of contact. It can however pick up a large number of electrons from the object which has a large surface of contact [27]. As the surface density of trapped electrons is the same for both objects at the beginning of the experiment, the number of trapped electrons on the small surface of contact of object A in

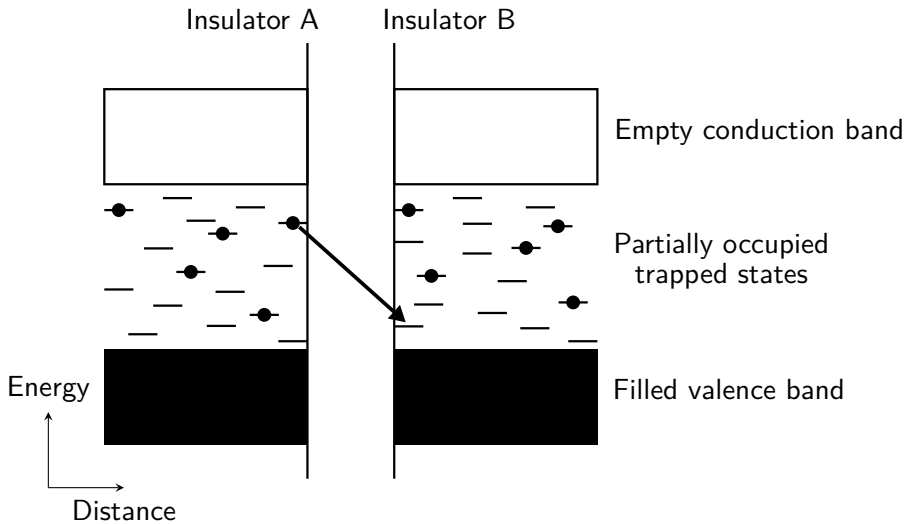


**Figure 10:** Electronic band structure of two insulators and transfer of a trapped electron between two insulators in contact.

figure 8(right) is much smaller than the number of trapped electrons on the large surface of contact of object B. After some time, the smaller surface of contact of A will be completely depleted in trapped electrons but will still be able to pick up those of the large surface of contact of B. As a consequence, the object A will charge negatively and the object B positively as reported in experiments.

This mechanism has been tested in numerical simulations to show that it could indeed explain the charging of identical materials [28–30]. In this study, the collisions between the particles of a binary mixture composed of identical small and large particles (*i.e.* with equal surface trapped electron densities) have been reproduced numerically. The number of high energy trapped electrons and the number of low energy electrons are fixed at the beginning of the simulation. Once a collision between two particles occurs, one trapped high energy electron is transferred to a low energy state from each particle to the other. The transfers continue at subsequent collisions as long as there are still some high-energy trapped electrons on the particles. It has been observed with that simple numerical simulation model that large particles charge positively and small particles charge negatively. Numerical measurements and analytical expressions of the particles' charge over time both indicate that the particles do

not charge at the beginning of the simulation but eventually reach the expected polarity [25, 28]. Indeed, let  $n_A$  and  $n_B$  be the number of high-energy trapped electrons on particles A and B respectively. While  $n_A > 0$  and  $n_B > 0$ , transfers of electrons from both particles occur so there is no net charging of the particles. If  $n_A > 0$  and  $n_B = 0$ , there is a transfer of one electron from particle A to particle B but not from B to A which explains the asymmetric charging of large particles that carry more trapped electrons than smaller particles because of their larger surface area.

The transfer of trapped electrons thus seems to be a good candidate to explain the tribocharging of identical insulators. There must however be sufficient trapped electrons at the surface of objects to make sure that this effect is indeed responsible for the measured charges. After measuring the charge of fluidized particles using an electrostatic separator shown in the right panel of figure 9, Waitukaitis *et al.* measured the number of trapped electrons on those particles using thermoluminescence [20]. By heating the sample, they managed to provide sufficient thermal energy to the material to allow the trapped electrons to spontaneously relax to a low-energy state. Once this transition occurs, photons are emitted and detected by a photomultiplier to measure the density of trapped electrons. They observed that even by loading a maximum of trap states using UV light before heating the sample, the density of trapped electrons was 5 orders of magnitude smaller than the amount necessary to account for the charge transfer they obtain in the free-falling experiment [20]. In conclusion, even though the transfer of trapped electrons seemed really appealing and allowed to explain some of the observations made on asymmetric rubbing, they do not exist in sufficient quantities at the surface of insulators to account for their measured charges.

### 2.1.5 Patch model

Considering that contact charging seems to occur at the surface of objects as suggested by the observations made on the influence of size and the asymmetry of rubbing, many studies focused on characterizing the surface before and after contact. Using probes, especially Kelvin probes, it has been observed that the charge at the surface of objects was not uniform after contact as shown in figure 11(top left and right) [31–34]. Other convenient experimental techniques using

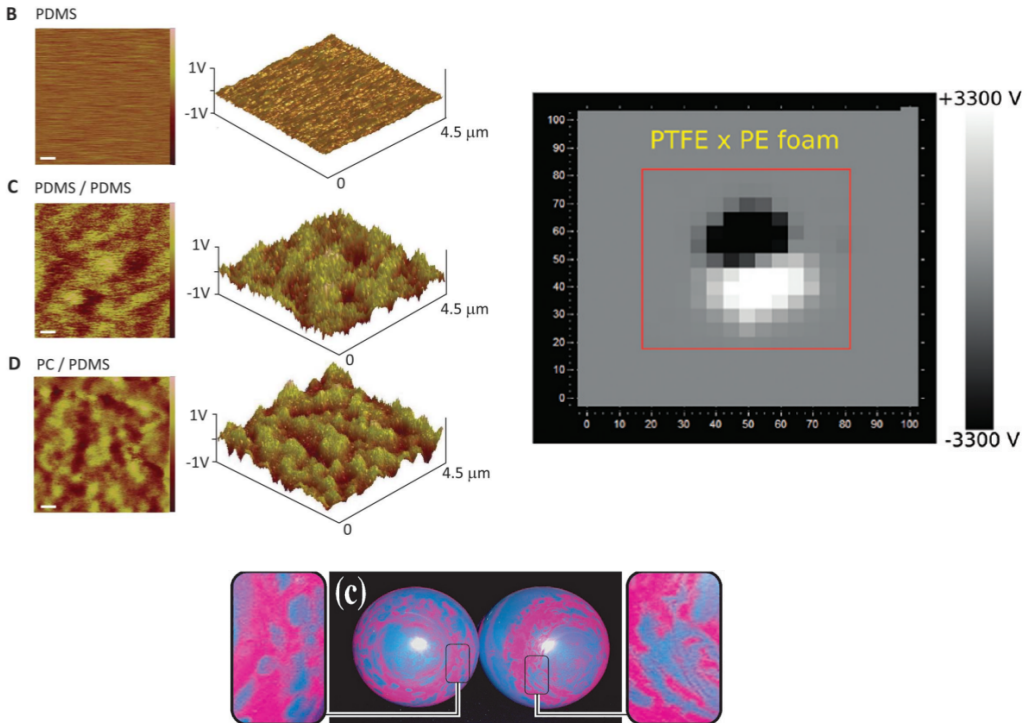


**Figure 11:** Non-uniform surface charging of materials after contact/rubbing. **(Top, left)** Kelvin Force Microscopy (KFM) of different materials' surface before and after contact shows microscopic positive and negative regions on the surface. Taken from [31]. **(Top, right)** Potential patterns obtained after rubbing PTFE with PE. Taken from [33]. **(Bottom)** Two latex balloons rubbed one against the other. Some magenta toner sticks to the surface where the balloons are negatively charged. Taken from [35].

printer toners that stick to negatively charged objects have also revealed that the toner accumulate locally to form patches as shown in figure 11(bottom) [35,36]. Rather than charging uniformly, the materials' surface is thus characterized by some positive and negative domains on scales as large as a few millimeters.

Furthermore, the fact that charging would be localized rather than uniform could explain some observations made on contact charging. For example, it has been observed in microgravity experiments that particles in an electric field could both stick to each other and be attracted by the same electrode, indicating that they are of the same charge [37]. Such interaction would be impossible if the

particles were uniformly charged as two particles with the same charge repel. However, Steinpilz *et al.* demonstrate that if the particles were non-uniformly charged (*i.e.* composed of many patches of different charges on the surface), then attraction could be possible even if they have identical or zero net charges [37].

Apodaca *et al.* also show that the presence of patches at the surface of materials could explain the tribocharging of identical materials [38]. To measure the charging of identical objects, they first cut two pieces out of a single piece of a polymer, polydimethylsiloxane (PDMS), to make sure that the two objects in contact are perfectly identical. When put in contact, these two objects charge oppositely (one charges + and the other one charges -). The charges, that are measured using a Faraday cup, continue increasing during following contacts and are equal in magnitude for both objects. They eventually saturate and do not exceed a certain final charge that depends on the size of the objects [38]. These results are interpreted by the fact that contact electrification could result from the existence of small fluctuations in the compositions of the contacting surfaces. It is assumed that the surfaces are composed of some sites that can donate charges (the donor sites) and sites that can accept charges (the acceptor sites). When two surfaces are put in contact, charge transfers occur when a donor touches an acceptor as shown in figure 12. Then, if a transfer has occurred between two sites, these sites cannot exchange charges anymore during subsequent contacts [38]. As a consequence, some sites are positively charged and others are negatively charged, as it has been observed using probes to analyze the surface of objects after contact as shown in the previous figure 11. Using this patch model, the evolution of charge with the number of contacts as well as the correlation between the final charge and the size of the system can be obtained by tuning the number of donor and acceptor sites.

This model has also been used and analyzed in numerical simulations to verify its validity. To mimic a contact between two surfaces composed of donor and acceptor sites, two N-elements matrices can be created and single elements can be defined as donors or acceptors [39]. By comparing the elements having the same positions in the matrices, contacts can be reproduced. In these simulations, it is observed that the transfers of charges that occur between the surfaces are consistent with what was obtained in experiments with identical materials. The



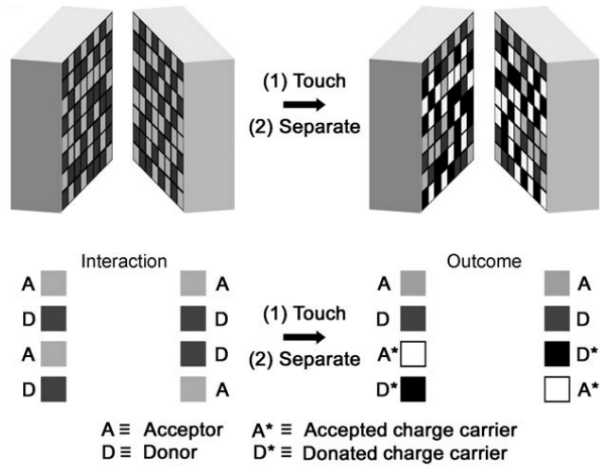


**Figure 12:** The patch model developed by Apodaca *et al.* to interpret the charging of perfectly identical materials. Even though objects are made of the same materials, small fluctuations exist in the composition of the contacting surfaces: the donor and the acceptor sites. Taken from [38].

surfaces charge oppositely, with the same magnitude, their charge rapidly increases during the first contacts and finally saturates. The influence of the system's size on the final charge is also retrieved like in Apodaca *et al.*'s experiments but an intermediate scale between the system's size and the elements' size also seem to have importance. By gathering sites of the same type, the charge transfer between the surfaces is indeed larger [39]. The reason why asymmetric rubbing has an influence on the charge as well as the contact electrification of different materials could also be explained with these simulations [40].

In the patch model, it is assumed that donors exchange negative charges with acceptors resulting in positively charged donor and negatively charged acceptor after a successful contact. But unfortunately, this model does not precise how or what charges are carried from one object to the other.

### 2.1.6 Capacitor model

Other models, which are still considered, have been proposed to interpret the measurement of a saturating charge after repeated contacts such as the capacitor model [41]. This model considers that the contact between insulators can be

regarded as a capacitor. When two objects are in close proximity, the capacitance resulting from the presence of the two surfaces is determined as well as the potential difference. To do so, this model takes in consideration the area of contact between the interacting objects and an electric cut-off distance to determine the capacitance, and the effects of the image charges for the potential difference. The result is a model that predicts an increasing particle charge until a maximum saturation charge is reached. It is an interesting tool to reproduce the contact charging of identical insulators but physical interpretation is more complex.

### 2.1.7 Role of strain

Experiments on the charging of stretched materials could help identify the charge carriers that are responsible for the tribocharging of identical materials. For example, simple experiments with a latex balloon rubbed on someone's hair show that the balloon more easily attracts the hair if it has been inflated. Measurements of the charging of inflated and deflated latex balloons have been performed and reveal that stretching has indeed an influence on the amplitude of charging [42]. On more than 100 experiments contacting a deflated balloon on PTFE (*i.e.* Teflon) and cleaning surfaces after each contact for maximum reproducibility, it has been observed that PTFE always charges positively [42]. When performing the same experiments but with an inflated balloon, PTFE charges negatively. Strain could thus control the direction of charge transfer in contact charging [42].

Using identical materials, it has been reported that when rubbing a piece of material with a stretched piece of the same material, the stretched one systematically charges positively while the other one charges negatively [43, 44].

Further experiments on stretched rubber have been conducted to try to explain what affects the charging of stretched materials. By doing cycles of stretching/relaxing natural rubber, it has been observed that the electric potential of a stretched piece of rubber changes with strain without having to rub it on any other material [45, 46]. Each time the material is stretched, it charges positively and when it is relaxed, it charges negatively. During those experiments, it was observed that ambient humidity could affect the experimental results. The same experiments have thus been reproduced under higher relative humidity which lead

to larger amplitude of potential variation [45].

In each of these studies, the effect of strain on charging is attributed to an alteration of the surface's properties. Using X-ray diffraction and Raman spectroscopy, it has been shown that the chemical composition of the material did not significantly change with strain [42, 44]. However, studying the light transmission of stretched materials reveals that transmittance decreases with strain [44]. Scanning electron microscopy of the materials surface revealed that microscopic holes are created in the material as it is stretched [44, 46]. As those holes scatter light, it explains why the transmittance is lower for stretched materials. With those holes, materials with different chemical composition than the rest of the surface (coming from the bulk), especially polar molecules, are exposed to the surface [44, 46]. The charging of stretched materials could thus be consistent with an adsorption of negatively charged water close to the holes because of these newly exposed polar molecules. If the material is stretched, the apparition of polar molecules at its surface could enhance the adsorption of water enriched in negative ions. Strain thus contribute to the negative charging of the material.

The adsorption of negative ions because of strain could also explain why PTFE charges negatively when rubbed with an inflated balloon in Sow *et al.*'s experiments [42] and also why PTFE charges negatively when rubbed with stretched PTFE in Wang *et al.*'s experiments [44]. Those studies thus suggest that ions could be the charge carriers responsible for contact charging.

### 2.1.8 Role of ions and humidity

Ions are naturally present in water as a consequence of the self-ionization reaction. In this reversible reaction, hydroxide ( $\text{OH}^-$ ) and hydronium ( $\text{H}_3\text{O}^+$ ) ions are produced by the ionization of water. Therefore a transfer of water at contact between two materials implies a transfer of ions and thus possibly a small change in the materials' charge.

McCarthy and Whitesides [47] propose the hydroxide-adsorption model to explain the contact electrification of materials. In their study, they demonstrate that  $\text{OH}^-$

ions are mobile and can be transferred between thin water layers at the surface of materials as shown in figure 13. The model thus considers that if one of the two materials has a higher affinity with hydroxide,  $\text{OH}^-$  ions are transferred to this material while the concentration of positive hydronium ions remains constant. A contact between these materials would result in a segregation of the hydroxide ions and an opposite charging of the two materials.

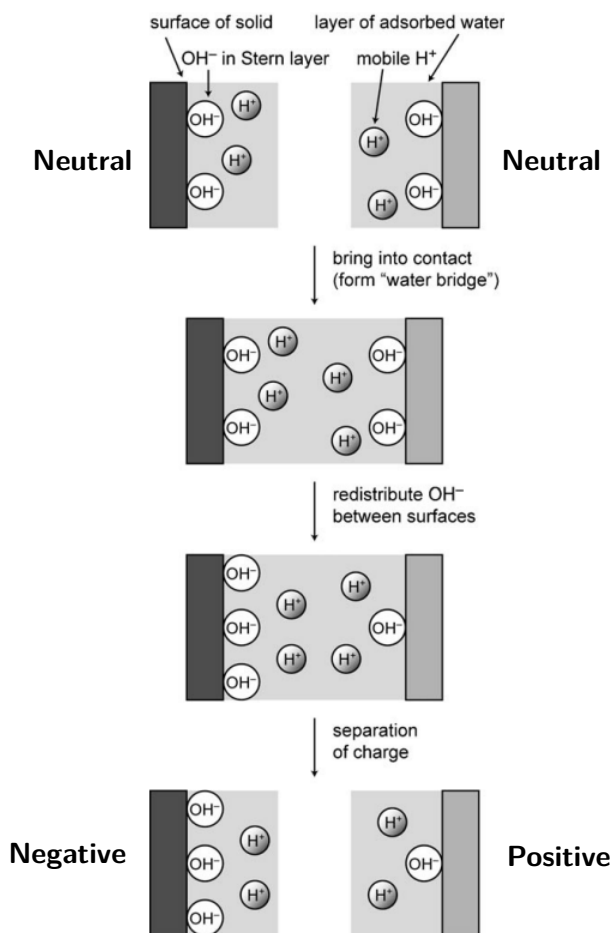


**Figure 13:** The hydroxide-adsorption model proposed by McCarthy and Whitesides [47]. At contact between two materials covered with a thin layer of water, the hydroxide  $\text{OH}^-$  ions naturally present in water can be transferred from one surface to the other and result in an opposite charging of the two materials. Adapted from [47].

Experiments have been conducted to investigate this possible mechanism. Lee *et al.* studied the charging of hydrophilic and hydrophobic particles after contacting an hydrophilic or hydrophobic surface [48]. To precisely measure the charge of the particle after each contact, the particle is levitated using an acoustic trap which can be turned off and on again to let the particle touch the surface only once. Analyzing the oscillation of the levitated particle under an electric field then allows to measure the particle's global net charge. When an hydrophilic particle touches an hydrophobic surface, the particle steadily charges positively at a constant rate after successive contacts. If the particle is hydrophobic and the surface is hydrophilic, then the particle charges negatively at the same rate. If both the particle and the surface are hydrophilic or hydrophobic, the particle does not charge significantly. Identical results were also obtained by Schella *et al.* in vertically vibrated granular media [49]. McCarthy and Whitesides' hydroxide-adsorption model applies to explain these results but should be slightly adapted as hydrophobic surfaces are very likely not covered with water layers. As  $\text{OH}^-$  have a greater affinity with hydrophobic surfaces [48], when a wet surface contacts a dry surface,  $\text{OH}^-$  ions preferentially accumulate on the initially dry surface. As a consequence, a negative charge transfer occurs from the wet surface to the dry surface. Hydrophilic materials that are covered with larger amount of water thus charge positively while hydrophobic materials charge negatively [48].

Concerning the presence of water at the surface of materials that charge at contact, it has been shown that adsorbed layers (adlayers) of water formed islands [50] as shown in figure 14. This result has been obtained by depositing a graphene sheet on top of mica. As the sheet is deposited, it deforms to take the shape of the surface. If water is present on the surface, it is trapped under the sheet. Water can then be visualized using AFM which provides images as shown in figure 14. It has been shown that the islands could grow if the relative humidity was increased. These results lead to a significant conclusion, as these water islands bear a striking resemblance to the charged patches discussed in section 2.1.5.

Lots of recent other studies have focused on the influence of humidity on charging [21, 51–54] and all of them agree on the fact that humidity controls tribocharging through water adsorption. Despite the strong consistency of this theory with the

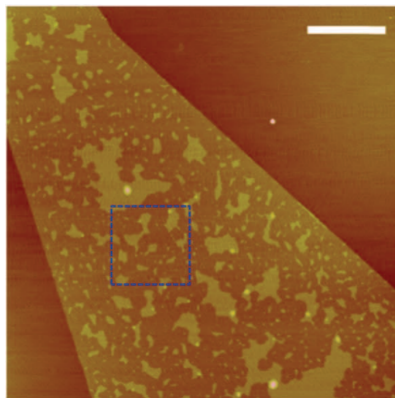


**Figure 14:** Adlayers of water at the surface of mica forming water islands (in light yellow). Scale bar at the upper right corner corresponds to  $1 \mu\text{m}$ . Taken from [50].

experimental results discussed above such as on the role of strain and the charged patches, the possible implication of water in the triboelectric effect is still currently debated. A few grey areas still remain such as the explanation of the effect of size discussed in section 2.1.3. Especially, the tribocharging of granular materials characterized by contacts between identical materials still raise interrogation. With granular materials, charge measurements seem to fluctuate from one study to the other which obviously casts doubt on existing theories. Their charging also disrupts the classical theories developed for ideal granular materials that do not include electrostatic interaction and make their behavior significantly more intricate and complex. The following section provides a description of our current knowledge on ideal granular materials and how the triboelectric effect influences these theories.

## 2.2 Granular materials

Let's imagine a pile of sand simply left in a closed box. As long as nobody or nothing interacts with the box, the pile of sand is immobile and it looks like we have a solid in the box. Now let's grasp the box and start tilting it slowly. At a certain angle, the sand will begin to flow like a liquid. If we rather shake vigorously the box in all directions, the sand particles fly all over the box, bouncing off the walls and describing almost straight trajectories like the molecules of a gas.

Those transitions between phases are really specific to granular materials and have

been the heart of most of the research that has ever been done on granular materials. Understanding granular materials consists in understanding what influences their state as well as how they go from one state to the other. This investigation has led to highly interesting features that are inherent to granular materials and listed in figure 15. This figure will serve as a mind map in this section to cover all of the phenomena that are specific to ideal granular materials.

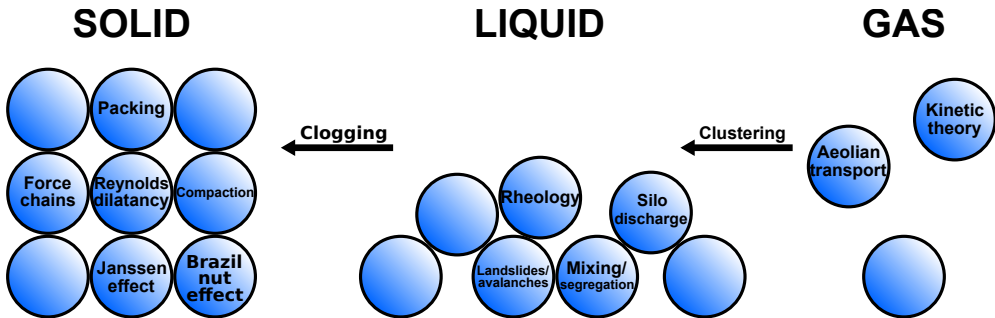


**Figure 15:** Subjects of interest in each granular materials phase and arrows representing the effects responsible for phase transitions.

### 2.2.1 Solid phase

#### The Janssen effect

The most trivial experiment one could do with granular materials that are in the solid phase is to weigh them in a recipient. Let us fill a container with granular materials and measure the total force exerted on the container's bottom plate, one would expect that the more the recipient is filled, the heavier the column of granular materials will be as we would obtain if the recipient was filled with a liquid. It has been shown in 1895 by German physicist H.A. Janssen that it was not the case [55]. For small fillings, the weight of the granular materials column increases linearly with its height but for larger heights of filling, weight does not increase anymore, it saturates. The experiment from 1895 done by H.A. Janssen with corn in silos has been reproduced and one can see in figure 16 that the pressure measured at the bottom of the silo saturates once the quantity of corn

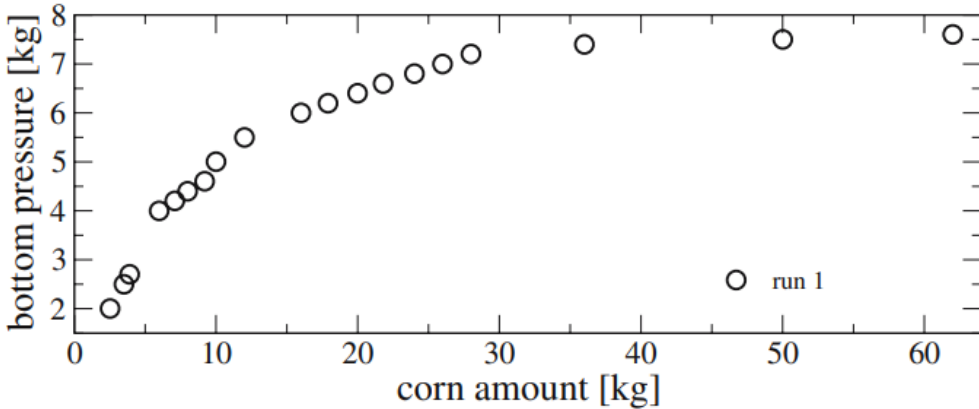


**Figure 16:** Measurement of the weight of corn in a silo cell with respect to silo's filling. For large fillings, weight does not increase anymore due to the Janssen effect. Taken from [56].

inside the silo increases [56]. This peculiar property of granular materials can be explained as a shielding effect as pressure is redirected towards the silo's walls because of friction between the particles and the walls. Expressing vertical and horizontal pressures and stresses of the granular material yields perfectly fitting exponentially decaying expressions for the pressure at the base of the silo with respect to silo's filling [55, 57, 58]. This nice agreement between equations and experiments thus indicate that the Janssen effect is quite well understood and effectively due to friction between grains and the sidewalls. This theory has even been successfully extended to non-static systems with moving walls [57, 58].

### Force chains and arches

The redirection of pressure towards the walls that is responsible for the Janssen effect is known as *force chains* [59–62]. When a granular media is compressed, only a few particles exert force one onto the other leading to the so-called force chains as all the particles that play a role in the transmission of the forces at contact create a network of force chains. Those force networks can be observed using photoelastic particles that are stress-birefringent particles whose light transmission properties are affected by stress. Once one photoelastic particle is submitted to an important stress, the polarization of light that passes through it is affected. Using a set of carefully placed polarizers, one can reveal solely particles that are



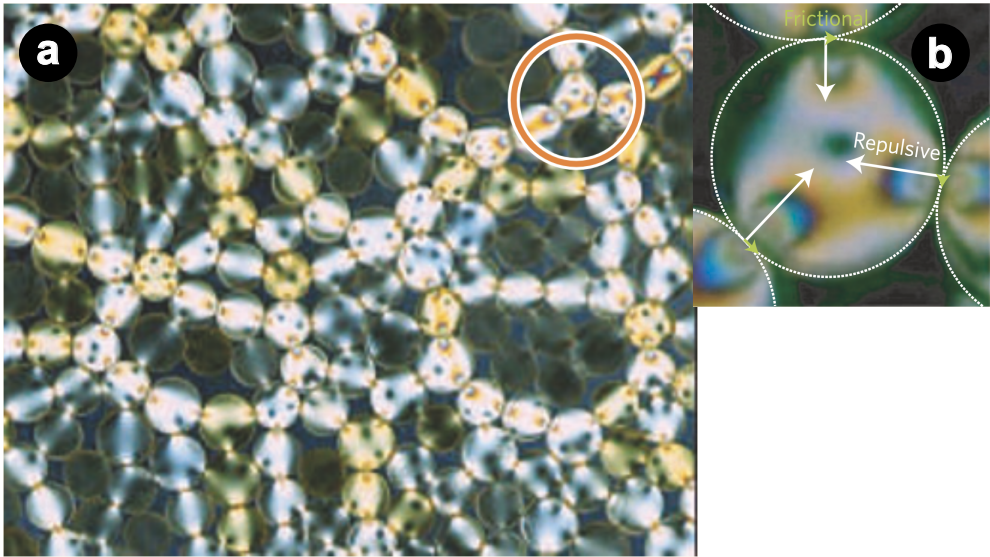


**Figure 17:** (a) Photoelastic disks revealing force chains, typical of granular media. Only the bright particles are exerting forces one onto the other. The brighter the particle, the more intense the force it is submitted to. (b) Close-up view of one photoelastic particle circled in red in the left pannel showing complex patterns that can be analyzed to determine the normal and tangential forces applied on the particle. Taken from [60].

exerting force one onto the other as shown in figures 17(a) and 18. The horizontal components of the force chains that can be seen in those vertically compressed granular media illustrate the redirection of pressure towards the walls that is the central assumption of Janssen's theory. Furthermore, the pattern observed inside each photoelastic particle as shown in figure 17(b) can be analyzed to estimate the intensity of the normal and tangential forces applied on the particle [59,60].

The Janssen effect that is provoked by force chains can have dramatic consequences as the pressure applied on the walls of silos can become so important that it could lead to the failure of the silo. Romans could however take advantage of those force chains to build aqueducts with arches.

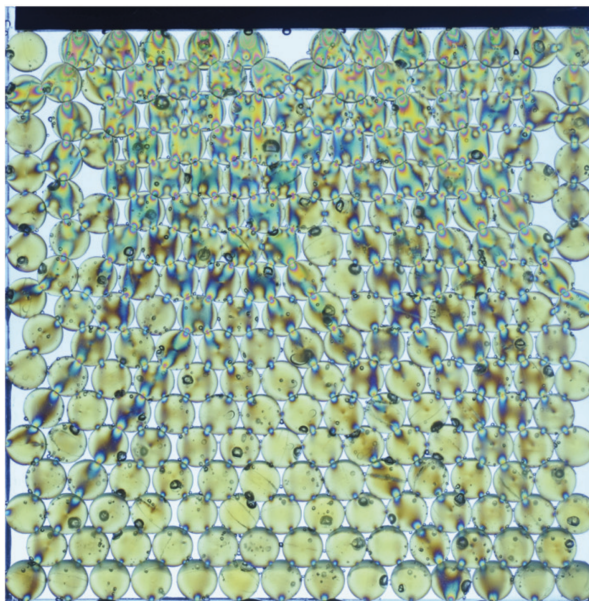


**Figure 18:** Compressed photoelastic particles with a vertical pressure applied on the top. Taken from [61].

### Reynolds dilatancy

Another effect of friction occurring in quasi-static granular materials is the increase of the total volume under shear. It has been discovered in 1885 by Irish physicist Osborne Reynolds that granular materials under pressure take more space (*i.e.* their apparent volume increases) and he called this effect *dilatancy* [63]. Just like the Janssen effect, dilatancy is a consequence of friction between the particles [64,65] and can be interpreted as a rearrangement of the particles under shear that leads to an increase of the granular material's volume as shown in figure 19. Dilatancy can be experienced in our everyday lives when walking on the beach on wet sand. One has already observed that sand seems to dry under our feet. Because of dilatancy, as the sand's volume increases under the weight of the person that is walking, voids appear between the particles and those voids can be filled with water. As a consequence, it looks like sand is drying as water is drained in the region close to our feet.

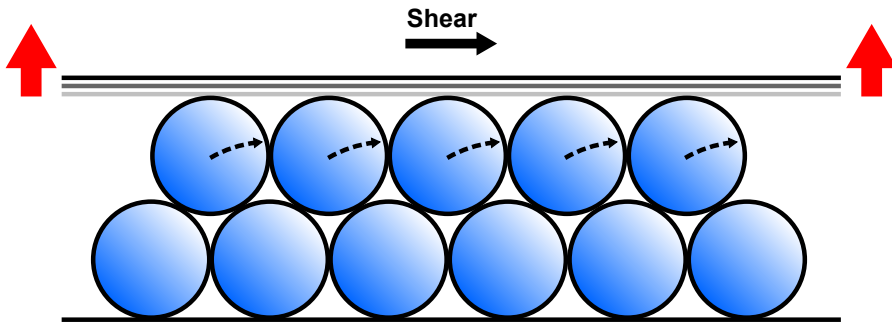


**Figure 19:** Schematic interpretation of the Reynolds dilatancy. As a granular media is sheared for example by a moving wall, its total volume increases because of friction between the particles. In this schematic view, the increase of volume indicated by the red arrows can be directly seen from the movement of the particles (dashed arrows) that is provoked by the moving wall.

### Compaction

In some applications, one would like the complete opposite effect, *i.e.* reduce granular materials' apparent volume which is a process known as compaction. It is for example an objective in industries that want to reduce the costs of transport by compacting granular materials as much as possible. Experiments show that by tapping repeatedly on a cell containing a granular material, its apparent volume decreases with the number of taps. Packing fraction (*i.e.* the volume of all particles divided by the apparent volume of the assembly) is often measured to quantify compaction and it was similarly shown that this parameter increases when tapping on the cell [66]. This effect has been attributed to the mobility of the particles within the granular material [66, 67] which is determined by the size of the voids in its surrounding area. Tapping on the container enables particles to rearrange and fill those voids.

From this observation, it has been shown that the asymptotic packing fraction one could reach by tapping on the cell was influenced if different sizes of particles compose the system [68, 69]. In ideal granular materials where particles do not interact, the larger the polydispersity (*i.e.* the difference between the sizes of the small and the large particles), the larger the asymptotic packing fraction. This result makes sense with the previous interpretation based on mobility as tiny

particles will easily fill the voids that are present in their surroundings. Moreover, it has been shown that there exists an optimum volume fraction of small beads to reach the highest packing fraction after tapping which lies somewhere between 30 and 40% [68, 69].

The way one taps on the container also has an influence on compaction. It has been shown that the top peak acceleration reached by the cell during tapping could be increased to enhance compaction [70, 71]. Indeed, more compacted systems can be obtained with higher shaking intensities. Interestingly, even higher packing fractions were obtained by increasing and then decreasing the top peak acceleration which is interpreted as an annealing effect of the voids left between the particles [72].

### **Brazil nut effect**

Compaction is not the only observable effect in vibrated granular materials. Indeed, gently shaking granular materials in a container will not only compact it but also induce a movement of the larger particles towards the surface if it contains a mixture of small and large particles. This size segregation effect is known as the brazil nut effect named for the fact that in a container of well-mixed nuts, the larger brazil nuts always seem to rise to the top after transport [73]. The upward motion of large particles is explained by the fact that when shaking the container, particles can move apart from each other. Voids could therefore appear beneath large particles and remain stable because of the particles arches created by the force chains described earlier [74, 75]. The smaller particles in the mixture will then fill those voids which will, as the process recurs at each tap, make large particles rise progressively to the top. The collective displacement of all the large particles in the mixture towards the top implies that the small particles initially located above them must move towards the bottom of the container. It has been shown that convective cycles take place in vibrated granular materials with an upward flow in the center of the cell and falling in a thin layer close to the walls [76, 77].

The Brazil nut effect is considered as a perfect case of study of thermodynamics

out of equilibrium. The system is continuously agitated which serves as an energy input and the inelastic collisions between the particles causes energy dissipation. This leads to the apparition of macroscopic structures (segregation) that increase the system's entropy. The emergence of segregation from energy input and dissipation highlights the inherently non-equilibrium nature of the Brazil nut effect. This effect offers insights into the thermodynamic principles governing non-equilibrium phenomena in granular systems.

To sum up this section, the exploration of the physics governing solid granular materials reveals a flourishing field that emerged at the end of the nineteenth century, undoubtedly triggered by the Industrial Revolution. It led to breakthrough discoveries such as the Janssen effect or the Reynolds dilatancy. Static granular materials are characterized by arches, dilatancy and voids between the particles that arise because of friction between the particles. Even though static granular materials are quite well understood, some topics of research are still very active. For instance, force chains and compaction are still the subjects of many publications in the community.

All these studies have been carried out using ideal granular materials. The properties of such granular materials that have been discussed in this section are influenced by cohesion. It has indeed been shown in simulations and experiments that the compaction and the force chains of cohesive granular materials were slightly different [78–80].

Let us now shake granular materials (much more) vigorously ...

### 2.2.2 Gaseous phase

When granular materials are strongly agitated, the particles interact mostly two by two like the molecules of a gas. As the thermodynamic behavior of gases has been successfully described by the kinetic theory of gases, the analogy between agitated granular materials and gases led to the development of a granular kinetic theory [81, 82]. Strongly agitated granular materials are even often referred to as *granular gases*.

### The kinetic theory of granular gases

In the classical kinetic theory, temperature defines the state of gases. One should thus also define a granular temperature to extend the kinetic theory to granular gases. This temperature is obtained by decomposing the instantaneous translation velocity of a particle  $\mathbf{v}$  into a mean velocity  $\mathbf{u}$  and a fluctuating part  $\delta\mathbf{v}$  which yields

$$\mathbf{v} = \mathbf{u} + \delta\mathbf{v}. \quad (1)$$

The granular temperature is then given by

$$T = \langle \delta\mathbf{v}^2 \rangle, \quad (2)$$

which tells us that granular temperature is given by the fluctuating part of the particles' kinetic energy. Once the temperature of a granular gas is defined, one can derive the state equations of granular gases such as pressure, velocity, thermal conductivity or energy [81, 83].

There is however a major difference between classical gases and granular gases which is the fact that there is dissipation of energy once the particles of granular materials collide. The fact that contacts are dissipative in granular gases must be taken into account for the calculation of granular gases' energy and it has significant consequences on their state. Indeed, considering the definition of the granular temperature, if there is dissipation, then the velocity fluctuations are smaller and so does the temperature. As granular temperature defines the flow of granular gases (because pressure, viscosity or conductivity all depend on  $T$ ), if  $T$  varies then the flow is also influenced.

### Clustering

This kinetic theory of granular gases has been validated by experiments as it has been shown that in continuously vibrated granular materials, clusters form at high enough particle density in the cell because of the inelasticity of the collisions between the particles [84–86]. The clusters formed in microgravity by metallic bronze beads with a diameter of 1 mm are shown in figure 20 (left). Increasing

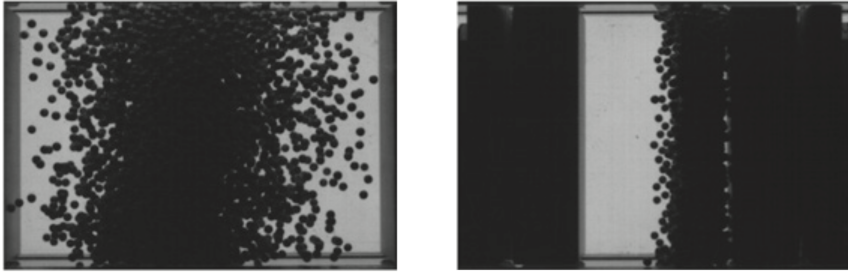


**Figure 20:** Strongly agitated granular materials (bronze beads with a diameter of 1 mm) by two horizontally oscillating walls in microgravity. Left panel shows the clustering of granular materials that occurs because of energy dissipation at contact between the particles. Right panel shows the bouncing regime characterized by the bouncing of all the particles from one wall to the other as a single body when the particle density is high enough. Taken from [86].

even further the particle density leads to a bouncing regime where all the particles move as one single body as shown in figure 20 (right). The clusters of particles that form in granular gases because of energy dissipation are large dynamic bodies as their shape continuously changes. Clustering is thus a phase transition in granular materials from gas to liquid.

As the particles of a granular gas experience lots of collisions between each other, they can charge significantly. The electrostatic charging of granular gases has been shown in microgravity experiments similar to those shown in figure 20 without lateral agitation (static cell in microgravity) [37]. Even though the particle distribution in the cell is uniform at the onset of the microgravity phase, particles aggregate after a few seconds because of electrostatic interaction [37, 87] as shown in figure 21. The aggregates obtained can have sizes up to a few centimeters and are stable as they can bounce at relatively high velocities on the walls of the cell without breaking [87]. Such aggregates were also reported in numerical simulations by implementing charge transfer at contact and Coulomb interaction between charged particles [88]. The high stability of these aggregates despite their global neutral charge is explained by the fact that as particles are insulators that are locally charged, they stick because of opposite sign patches [87].

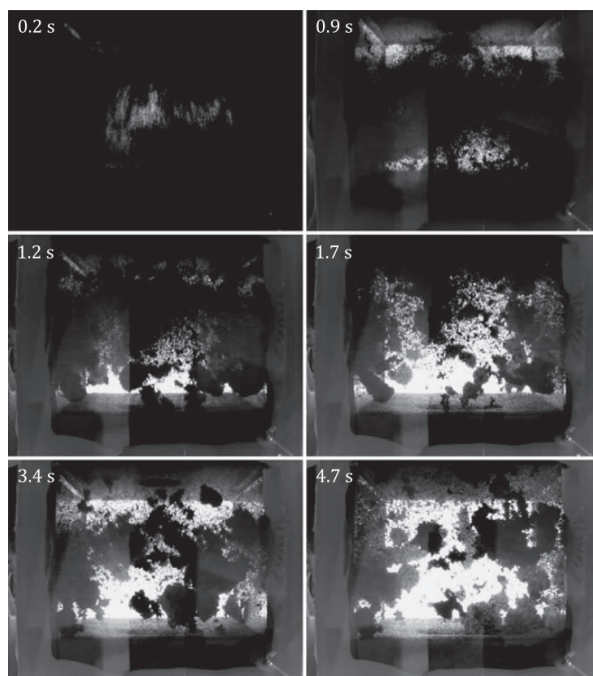


**Figure 21:** Time evolution of the aggregation of a charged granular gas in microgravity. The cell is 50 mm  $\times$  50 mm  $\times$  42 mm and agitated (to charge the particles) prior to being launched vertically in a drop tower for microgravity experiment. Taken from [87].

It is believed that such tribocharging of granular gases could provide an explanation to the formation of planets by aggregation of dust. At very early stages of planet formation, dust and ice grains collide and stick to each other because of van der Waals interaction. As the agglomerates' size increases, two aggregates colliding slowly will bounce off rather than stick to each other [87]. This is known as the *bouncing barrier* as it stops the growth of dust agglomerates when they reach a few millimeters in size. On the other hand, if the agglomerate is large enough (on the order of a meter), gravity takes over for further aggregation. There is thus a gap in the millimeter to centimeter range that requires other mechanisms such as electrostatic interaction.

Charging also presents an effective means to regulate the cooling process of granular gases. Research has demonstrated that when particles within a granular gas possess charges of the same polarity, the rate of decrease in granular



temperature is notably reduced [88, 89]. As particles repel each other, the rate of collision decreases and energy thus dissipates less fast.

### 2.2.3 Liquid phase

This last phase of granular materials lies between the solid and the gas phases in terms of the grains' kinetic energy. In the liquid phase, particles are in motion but a contact network still exists, like in the solid phase. Grains interact mostly through collisional and frictional contacts. Similarly than granular gases look like classical gases, flowing granular materials exhibit numerous similarities with classical liquids. The theories developed to describe the flow of liquids can be transposed to the case of granular materials.

### Rheology

Rheology is the branch of physics that deals with the way in which liquids behave under applied forces or stresses. It uses shear stress, shear rate and viscosity to define the flow of liquids under shear. Let's thus consider a granular material sheared between two horizontal plates as shown in figure 19 to develop the rheology of granular materials. In this plane shear configuration, four parameters control the flow; namely, the size of the grains  $d$ , the density of the grains  $\rho$ , the shear rate  $\dot{\gamma} = \frac{v_w}{L}$  with  $v_w$  the speed of the moving wall and  $L$  the distance between the plates and the pressure  $P$  applied on the moving plate. A dimensional analysis yields a dimensionless number that controls the system

$$I = \frac{\dot{\gamma}d}{\sqrt{P/\rho}}. \quad (3)$$

This number is called the inertial number as it compares a microscopic timescale  $\frac{d}{\sqrt{P/\rho}}$  that gives a typical inertial timescale of the rearrangement of the particles under the pressure  $P$  and a macroscopic timescale  $\frac{1}{\dot{\gamma}}$  linked to the mean deformation [65, 82, 90–92]. A large inertial number corresponds to a rapid flow as the time of rearrangement is larger than the time of deformation while small values of  $I$  correspond to a quasi-static regime as the deformation is slow compared to the microscopic rearrangement [90].

Dimensional analysis also tells us that pressure  $P$  and shear stress  $\tau$  are proportional through a coefficient of friction  $\mu$  that depends on the inertial number [65]

$$\tau = \mu(I)P. \quad (4)$$

An expression for this effective coefficient of friction cannot be obtained using dimensional analysis and it is thus determined experimentally or using numerical simulations. This  $\mu(I)$  theory can be used to characterize the flow of granular materials in different configurations. It allows one to define the regime of the granular flow, the behavior of a granular liquid under stress or an effective viscosity of the granular liquid.

Granular liquids can be obtained in different configurations which are represented in figure 22. The rheology of granular materials can be investigated in each of these configurations to determine the characteristics of the flow [90,92]. Each of these geometries display specific properties that are reviewed below.

### **Silo discharge**

The flow of granular materials out of a silo (*i.e.* silo discharge) has been and is still particularly studied for instance because of the wide use of silos for storage in many applications. The  $\mu(I)$  theory has been successfully applied to reproduce accurately this type of flow in numerical simulations [82, 93] but there is one specific feature about silo discharge that has been deeply investigated: clogging. Clogging occurs when an arch forms at the outlet of the silo and stops the flow. Arches have already been discussed in section 2.2.1 on force chains and are responsible for a phase transition from liquid to solid. In silos, arches are stable static structures of grains that form above the outlet and hold back the grains that are located above it. The main parameter controlling a clogging event is the ratio between the size of the silo outlet and the size of the grains [94–96]. The probability of clogging indeed increases when the radius of the orifice decreases. Once the flow has stopped, an input of energy or stress is required to restart the flow [97]. The number of grains between two clogging events (called an avalanche) can also be quantified to show the effect of the silo's aperture size [95]. It has been shown that there exists a critical size of the orifice below which

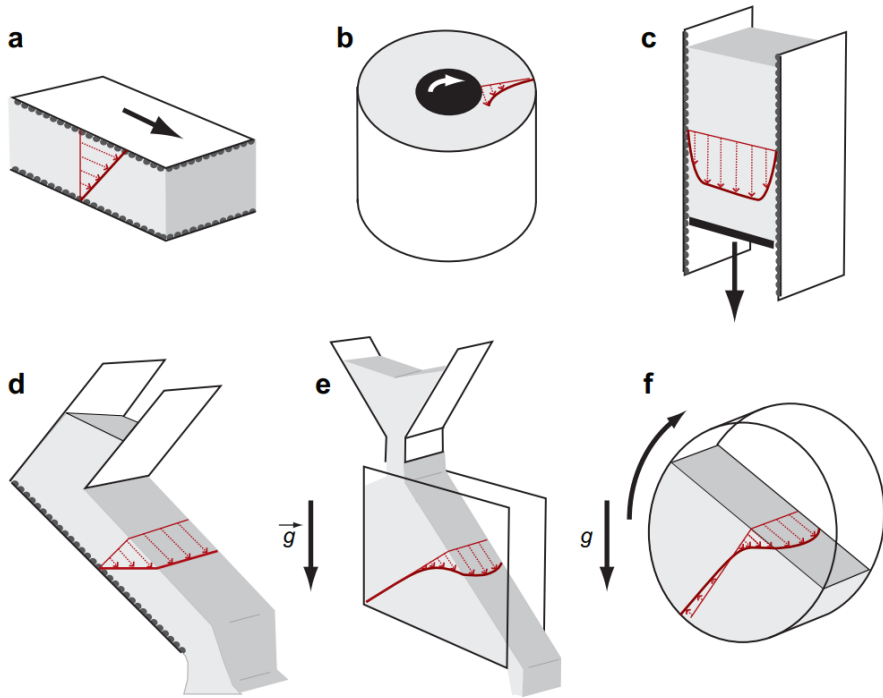


**Figure 22:** Flowing granular materials in different configurations (a) plane shear, (b) Couette cell, (c) silo, (d) inclined plane, (e) pile or heap flow and (f) rotating drum. Most applications in which granular materials flow can be viewed as a flow in one of these configurations which is the reason why they have been extensively studied. Taken from [90].

clogging will occur [98].

Tribocharging during silo discharge is well-known and has dramatic consequences if the granular material stored in the silo is inflammable. Indeed, significant charging can be reached during silo discharge or loading. If the charge is sufficiently high and the powder is inflammable, sparks can happen and ignite the material. Such incidents have been reported several times in grain silos [99, 100].

### **Inclined planes, heap flow, landslides and avalanches**

Granular flows down an inclined plane and heap flows have also received much attention, motivated by the explanation of natural phenomena such as landslides

and avalanches. It has been shown that flows on inclined planes were characterized by a critical angle of the plane at which the flow starts [101, 102]. In-depth analysis of the parameters influencing this critical angle allowed to determine how landslides and avalanches were triggered and comparison to granular flow allows to establish the equations for numerical simulations [103, 104]. Other features of such granular materials flows – called *debris flows* – like the volume of material transported or the distance of runout [105] could be predicted to provide important information in case of emergency.

Investigating the effect of electrostatic charges in landslides does not make sense considering the large size of the grains and the presence of interstitial fluid that would dissipate the charges. However, the charging of small particles that are in contact with inclined planes has been investigated. Particles are poured on top of an inclined plane (or tube) and collected at the bottom in a Faraday cup to measure the net charge of the sample. It has been observed that the sample can become positively or negatively charged depending on the materials of the particles, the plate, or the tube [106–109]. Surprisingly, the angle of the plane has a major influence on the final charge of the particles. In most experiments, the measured net charge decreases when the tilt angle increases [106, 107, 109]. Ireland [106] shows that this effect could be due to the fact that when particles flow down inclined surfaces, they bounce much more if the plane is inclined. Less particles are thus in contact with the plane and the transfers of charges because of the triboelectric effect occur less often. He highlights two parameters that influences the fraction of bouncing particles on inclined planes, and so the particles' charge: the shape of the particles and the friction between the particles and the plate [110]. When the particles are almost flat, no rolling is observed and the measured charge is quite small as the area of contact of the particle with the plate is always the same. When the particles are perfectly circular, they roll down the plane without bouncing and the charging is maximum. In between these two regimes, when they are almost circular and if the coefficient of friction between the particles and the plane is high enough, the particles roll and bounce of the plane resulting in a significant charging but not as large as if the particle was just rolling. The reduced contacts between the particles and the plane because of bouncing at high tilt angles could thus explain why the charge decreases.

### The rotating drum

The flow of granular materials in rotating cylinders is quite similar to heap flow and granular flow on inclined planes in that they are all surface flows. Indeed, in these configurations, granular material in the liquid phase is flowing on top of a solid phase. Like in heap flows and flow on inclined planes, there exists a critical angle of the grain-air interface at which the flow starts as well as an angle at which it stops – the angle of repose [92]. The  $\mu(I)$  rheology can also be applied to this geometry except that it is slightly more complex as this theory is only satisfied locally [111, 112]. Instead, the flow of granular materials is often characterized by measuring the velocity of the particles in a slice of the granular bed, known as velocity profiles, and the angle of the interface. To perform such measurements, the flow of the particles beneath the surface must be analyzed which is quite tricky in this geometry because of the opacity of the particles. The techniques then used to characterize the flow of granular materials in rotating drums include

1. Quasi 2D cylinders (*e.g.* cylinders whose width is smaller than the radius and typically close to the particles' diameter) with transparent end walls for imaging [112–116],
2. Positron Emission Particle Tracking (PEPT) [117, 118],
3. Magnetic Resonance Imaging (MRI) [119, 120],
4. Fiber optic probes [121].

As PEPT, MRI and probes only allow to track a few particles or are invasive and disturb the flow, the first technique based on imaging the flow through transparent end caps is the most common experimental technique used. Yet this technique is problematic as it has been shown that the friction of the end walls has an influence on the flow of the particles in the rotating drum [119, 122–125]. The flow observed with this imaging technique is thus perturbed by the end wall effect which will be discussed in more details in the following section. Since all experimental techniques have drawbacks, numerical simulations offer a compelling alternative. They provide easy access to every particle's trajectory and offer much

greater freedom in controlling experimental parameters.

Compared to the other geometries shown in figure 22, the rotating drum has the particularity that it is a closed system which makes it easier to implement in numerical simulations as no particles exit the system. The flow rate can also be easily adjusted using the rotation speed to produce a steady granular flow. For these reasons, the rotating drum is often considered as the best geometry to analyze the flow of granular materials [126]. In the following section, the flow of granular materials in the rotating drum is reviewed in details as this setup has been largely employed in this thesis.

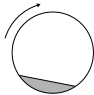
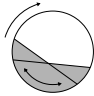
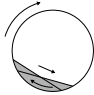


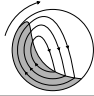
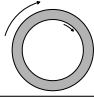
### 2.3 Granular flow in a rotating drum

#### 2.3.1 Flow regimes

Different granular flow regimes have been observed in the rotating drum depending on the filling degree and the rotation speed of the drum [79, 127, 128]. These regimes are represented in table 2 where the rotation speed is expressed using a dimensionless number called the Froude number that is given by the ratio between the inertia of the particles and gravity

$$Fr = \frac{\omega^2 R_d}{g}, \quad (5)$$

with  $\omega$  the rotation speed of the drum in rad/s and  $R_d$  the radius of the drum. At low rotation speed and low filling degree, the granular material is in the sliding regime. The whole bed slides on the drum. If the drum is slightly more filled, the flow is in the surging regime and the whole bed now moves as a solid up and down, sliding on the drum when it returns to the bottom. Increasing the rotation speed at low filling degrees leads to the slumping regime characterized by an intermittent flow which is defined by angles at which the flow starts and stops as discussed in the previous section. If the rotation speed is further increased, the flow is in the rolling regime which is now a continuous granular flow. The interface will then be S-shaped for even larger rotation speeds in the cascading regime. At large rotation speed, the particles will start flying off the granular bed in a parabolic motion which defines the cataracting regime and finally, at very large rotation speed, the whole granular bed is uniformly spread on the drum because of centrifugal force in

Regime	Schematic	Froude number ( $Fr$ )	Filling degree ( $f$ )
Sliding		$0 < Fr < 10^{-4}$	$f < 0.1$
Surging			$f > 0.1$
Slumping		$10^{-5} < Fr < 10^{-3}$	$f < 0.1$
Rolling		$10^{-4} < Fr < 10^{-2}$	$f > 0.1$
Cascading		$10^{-3} < Fr < 10^{-1}$	
Cataracting		$0.1 < Fr < 1$	$f > 0.2$
Centrifuging		$Fr \geq 1$	

**Table 2:** The different possible regimes of granular flow in the rotating drum depending on the filling degree and the rotation speed of the drum given by the Froude number. Table adapted from [128].

the centrifuging regime.

Consequently, a continuous granular flow effectively occurs only within a restricted range of the rotation speed, in the rolling and the cascading regimes which are the conditions of operation of all simulations in this thesis.

### 2.3.2 Velocity profiles and angle of flow

The flow of granular materials in rotating drums can be characterized more precisely by measuring the velocity profile. It consists in measuring the average velocity of the particles in a thin slice that is perpendicular to the free surface in the center of the drum as shown in figure 23. The shear rate can be obtained from this measurement and then an effective granular viscosity in comparison to liquids. For

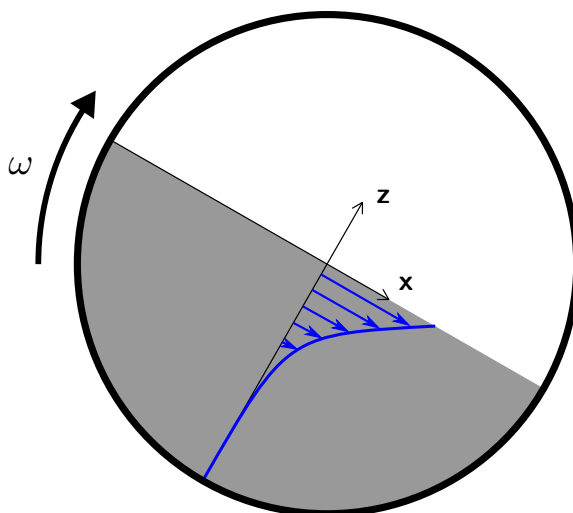


**Figure 23:** The velocity profile (in blue) is measured in the center of the drum, perpendicularly to the free surface ( $x$  axis). It consists in measuring the average velocity of the particles in a thin slice along the  $z$  axis. It is often measured in the reference frame that is rotating with the drum (as represented here).

ideal granular materials, it has been observed that the velocity profile was linear close to the surface up to a distortion point where the velocity of the particles decreases exponentially with depth [92, 111, 112, 129, 130], as shown in figure 24. The region close to the surface where the velocity profile is linear corresponds to the flowing layer (e.g. the liquid phase) while the region where the velocity of the particles decays exponentially up to the wall of the drum corresponds to the upward motion of the particles as a solid at the speed of the drum. The limit between those two regions thus define the liquid-solid interface and can be used to evaluate the depth of the flowing layer. As can be seen in figure 24, the depth of the flowing layer increases with the rotation speed as the distortion point goes deeper as  $\omega$  increases but the velocity profiles remain linear in the flowing layer with the same slope.

Any divergence from these reference velocity profiles obtained with ideal granular materials is the indication that the flow is perturbed because of different parameters. The velocity profiles are sensitive to any variation in the granular materials' properties as will be shown shortly which is why this measurement is insightful.



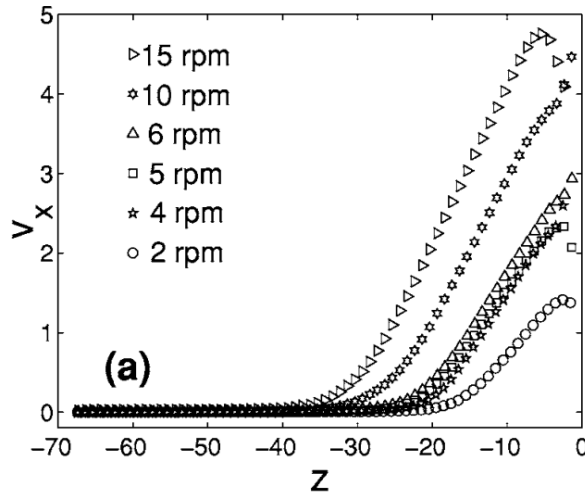


**Figure 24:** Typical velocity profiles obtained using numerical simulation to reproduce the flow of granular materials in a rotating drum. Different rotating speeds have been investigated (see symbols). Taken from [111].

The second measurement usually performed in rotating drums is the angle of the grain-air interface, called the dynamic angle of repose. This angle is obtained by fitting the interface at the center of the drum to avoid inappropriate linear fitting of a curved interface once it becomes S-shaped as shown in figure 25. It has been observed that the dynamic angle of repose increases with the rotation speed of the drum [119, 131–134] as shown in figure 26. Indeed, as the surface becomes more and more S-shaped due to the increase of the rotation speed, the angle at the center of the drum must increase. The dynamic angle of repose can be used to determine the transition from the rolling to the cascading regime which has been identified in a change of slope in the measurement of  $\theta$ . This transition can be seen around 15 rpm in figure 26. When comparing the dynamic angles of repose obtained with different sizes of particles, it has been observed that  $\theta$  decreases when the particles' size increases [119, 131] as shown in figure 26. The dynamic angle of repose is also influenced by the shape of the particles as it has been shown that it increases if the particles are rough [133]. The sensitivity of the dynamic angle of repose to several parameters – such as the particle's size and shape – also makes this measurement a reference to characterize granular materials and their flow in the rotating drum.

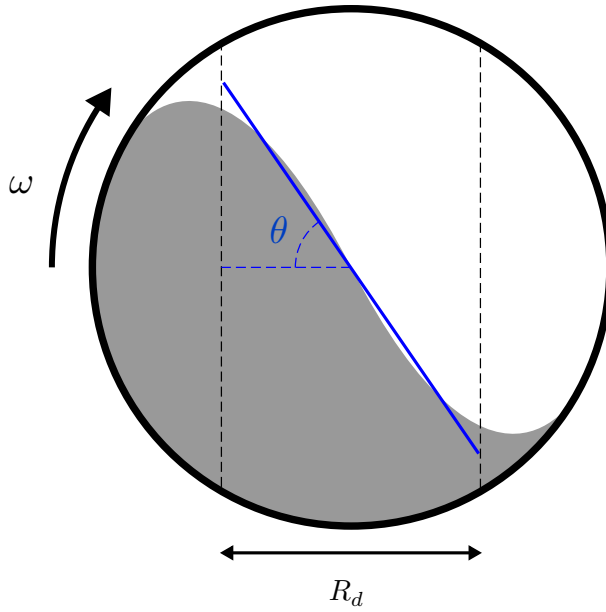


**Figure 25:** Measurement of the angle of flow, called the dynamic angle of repose  $\theta$ . As the interface might be S-shaped as shown here,  $\theta$  is often measured in the center of the drum by fitting the interface (blue line) over a region equal to the drum's radius  $R_d$ .

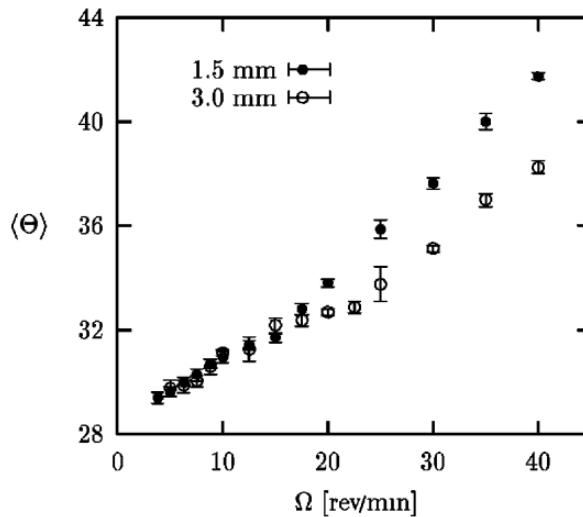


**Figure 26:** Evolution of the dynamic angle of repose for small (●) and large (○) glass beads with the rotation speed of the drum. Taken from [119].

### 2.3.3 End walls effect

Because of the friction of the end walls that close the rotating cylinder, the flow is disrupted close to these end walls. Particle tracking experiments and numerical simulations revealed a complex velocity profile close to the end walls [123–125]. First, the particles in the flowing layer immediately adjacent to the walls move slower than in the center of the drum. Then, a few particle diameters further from the end walls, the particles' velocity is larger. Therefore, in experiments using quasi 2D rotating drums, the velocity of the grains flowing down at the surface is significantly larger than in the center of large 3D drums [123]. The dynamic angle of repose is also larger close to the end walls [119] as a consequence of an S-shaped interface. Moreover, it has been shown that the S-shape is reduced once the friction of the end walls vanishes [79, 122].

This effect of the end walls is difficult to remove in most experiments using the traditional imaging technique in quasi 2D cylinders with transparent end walls. When analyzing other parameters, the flow might become complex to interpret. The solution would be to analyze the granular flow far from the end walls, at the center of a long rotating drum but as discussed earlier, it requires complex or invasive techniques. Therefore, numerical simulation is a powerful and interesting tool to investigate the flow of granular materials in rotating drums firstly because it provides a direct access to any particle's motion and also because it offers an infinite freedom on the definition of the experimental parameters.

### 2.3.4 Influence of cohesion

Among all the parameters that influence the flow of granular materials, cohesion is one of the least understood. As briefly discussed in the introductory section of this thesis, cohesion occurs when particles attract each other and the mechanisms that could be responsible of this interaction are still debated. When the relative humidity is high, liquid bridges are predominant [135–141] but the attraction because of liquid bridges is slightly different as it only appears after the contact between the particles resulting in adhesion rather than cohesion. In dry granular materials, van der Waals interaction [142–144] and electrostatic interaction are pointed out to explain cohesion. As cohesion is difficult to control precisely in experiments, magnetized dry granular materials have also been used to trigger

more easily cohesion [145–147].

Whether it is caused by liquid bridges, van der Waals interaction, a magnetic field or electrostatic charges, cohesion strongly influences the flow of granular materials. It has been shown in rotating drums that the rolling regime was replaced by an avalanching regime [140, 141, 148, 149]. Indeed, as can be seen in figure 27, cohesion leads to the formation of large clusters of particles that detach periodically from the granular bed and then flow down until a new avalanche is initiated. The continuous flow of ideal granular materials known as the rolling regime is thus replaced by an intermittent flow of aggregates which is a distinctive feature of cohesive granular materials. It can also be seen in this figure that powdered sugar, that has been obtained by grinding sugar crystals, displays a poor flowability compared to granulated sugar. It is often the case in nature and experiments, when the powder is fine, it is usually more cohesive. It has been shown by comparing different powders that when the size of the grains is small, granular materials are more cohesive [126].

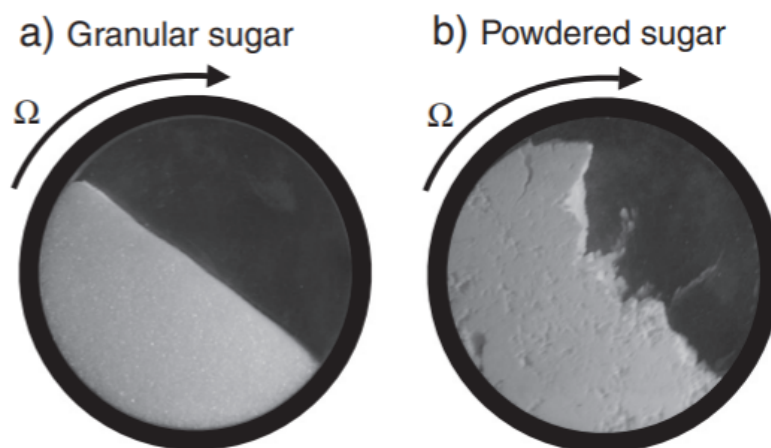


**Figure 27:** Flow of a non-cohesive granular material (left) compared to the flow of a cohesive granular material (right). The flow of cohesive granular materials is characterized by large clusters of particles that flow down the interface. Taken from [126].

The well-established methodology for investigating the flowability of non-cohesive granular materials based on the measurement of the velocity profile and the angle

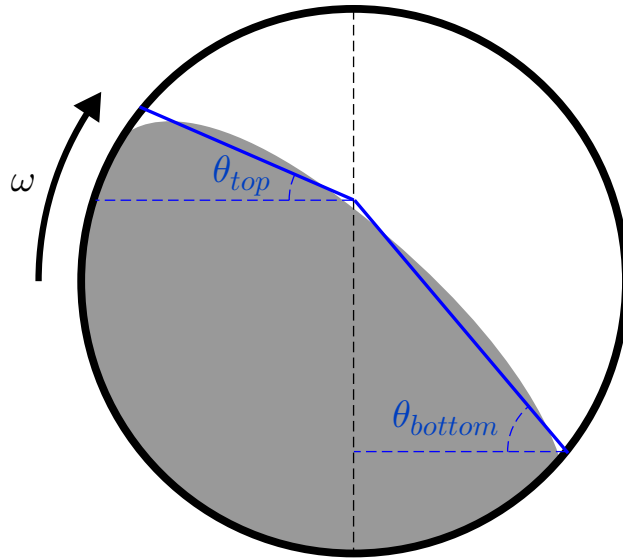


**Figure 28:** Measurement of the dynamic angles of repose when the granular material is cohesive. As the surface becomes convex because of cohesion, measuring the dynamic angle of repose as described in figure 25 is not suitable anymore. Instead, measuring two dynamic angles of repose,  $\theta_{top}$  at the top of the flowing layer and  $\theta_{bottom}$  at the bottom of the flowing layer is rather performed with cohesive granular materials.

of repose has been applied to cohesive granular materials [150, 151]. Firstly, the S-shaped interface can not be obtained anymore when granular materials are cohesive. The interface is rather convex for highly cohesive granular materials and the method described in section 2.3.2 to measure the interface's angle is not suitable anymore. For cohesive granular materials, one rather measures two angles, one at the top of the flowing layer  $\theta_{top}$  and one at the bottom  $\theta_{bottom}$  as shown in figure 28. As the cohesion increases, it has been observed that  $\theta_{top}$  decreases while  $\theta_{bottom}$  increases thus indicating the change of shape of the interface from S-shaped to convex shape. Concerning the velocity profile, it has been observed that it tends to flatten close to the surface when granular materials are cohesive as shown in figure 29. This plateau is consistent with the characteristic avalanching regime of flowing cohesive granular materials as it corresponds to the flow of particle aggregates as rigid bodies at the interface. All the particles in the aggregates flow down at the same velocity resulting in a constant velocity profile.

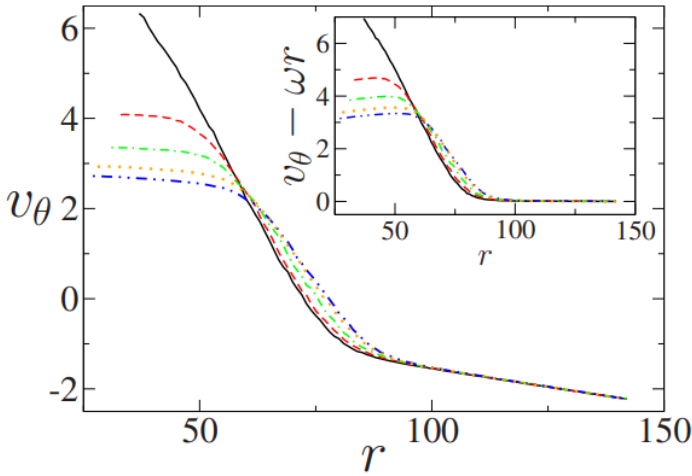


**Figure 29:** Typical velocity profiles (in the laboratory’s reference frame and in the rotating reference frame in inset) of cohesive granular materials in a rotating drum for no cohesion (solid black line) to strong cohesion (blue dot-dashed line). Taken in [150].

As the intermittent avalanching regime really seems to be the signature of cohesive granular materials’ flow, Espiritu *et al.* [152] propose a way to characterize the cohesiveness of a granular material by measuring the length of the grain-air interface that they called *spatial fluctuation*. They show that the larger the cohesion, the larger the spatial fluctuation.

### 2.3.5 Mixing/segregation

The rotating drum is not only used to characterize the flow of granular materials, it is also widely used to mix granular materials together. It has indeed been shown that the rotating drum was an appropriate tool to mix similar particles together no matter their roughness [133, 138]. Just a few rotations are necessary until all particles are perfectly mixed and the presence of smooth or rough particles in the granular bed does not influence the mixing. However, segregation (*i.e.* the separation of different particles) has been observed when trying to mix a binary mixture of large and small particles together as large particles were mostly found in the outer region of the bed, close to the cylinder’s wall [138]. Small particles are in the core, surrounded by large particles as they managed to pass through the gaps left by the large particles.

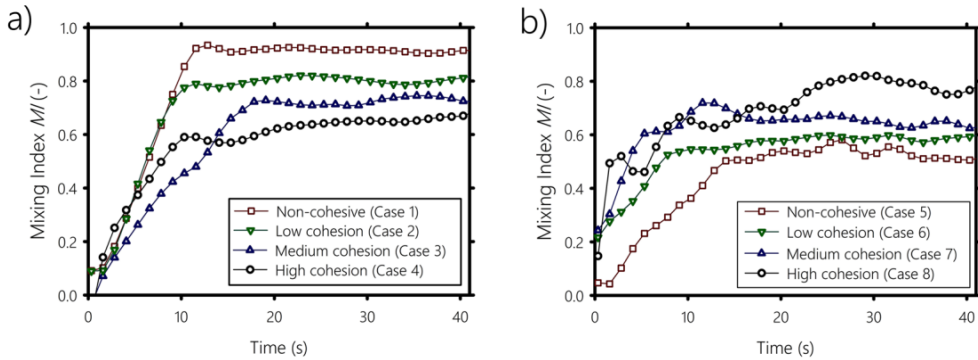


**Figure 30:** (a) Influence of cohesion on the mixing of particles having all the same size and (b) with a binary mixture of large and small particles. A mixing index close to 1 indicates that the particles are well mixed while a mixing index close to 0 indicates that the particles are segregated.

Segregation is also observed if particles of the same size are cohesive [138, 153] as shown in figure 30(a). It can be seen that the mixing index first increases sharply until it reaches a maximum value at which it saturates. The best mixing they could obtain depends on the intensity of cohesion between the particles with lower maximum mixing indexes for higher cohesion intensities. It could be explained as follows, as cohesion enhances the clustering of the particles, aggregates are pushed to the outer region of the drum as if they were the large particles of a binary mixture. Cohesion in monodisperse granular materials (*i.e.* in which all particles have the same size) thus induces segregation. Interestingly, if a binary mixture is cohesive, mixing can be improved as shown in figure 30(b). In this case, the highest mixing index is obtained for the most cohesive particles. Because of cohesion, small particles aggregate and thus cannot pass anymore through the gaps left by larger particles.

---

## 3 Motivations

---

Most granular materials commonly used in industries and daily life are cohesive. The pharmaceutical, food, construction and engineering industries all have to deal with one particularly undesirable property of cohesive granular materials which causes problems at every stage of granular materials' handling because of their a poor flowability. Indeed, because of the attraction between the particles, they aggregate which makes the granular flow intermittent. Any operation with cohesive granular materials thus becomes very complex. Moreover, despite the plentiful applications of cohesive granular materials, a very basic question remains: why are granular materials cohesive ? It can be obvious in some cases for example if the environment is saturated in humidity. Then, liquid bridges are responsible for some kind of cohesion, adhesion, and lots of studies have been focused on such wet granular materials. But in dry granular materials, the mechanisms of cohesion are still at the stage of hypotheses with van der Waals interaction and electrostatic charges as best candidates.

The reason why cohesion in granular materials is so difficult to explain is certainly due to the fact that the triboelectric effect, this thousands year old mystery that could be responsible for the development of electrostatic charges in granular materials, is not fully understood yet. We have seen that several theories have been proposed to explain the mechanisms of the triboelectric effect. Some of



them have been rejected and the validity of the others has not been shown yet. The lack of knowledge still make it difficult to interpret situations such as why electrostatic charges are present in granular materials when particles are agitated, during the discharge of silos or in dust clouds as discussed in section 2.2. Many other questions still need to be addressed such as why does the size of the particles have an effect on tribocharging ? Why does the charge of contacting object saturate after a few contacts ? Is the patch model valid for granular materials and can it be related to water patches ? Do granular materials become more cohesive when the size of the particles is reduced because of the triboelectric effect ?


The reason why we do not really understand the flow of cohesive granular materials is also certainly due to the fact that the best tool we have to analyze the flowability of granular materials, the rotating drum, gives us difficult access to a clean and steady granular flow, notably because of the end walls effect.

This thesis aims to explore the potential correlation between cohesion and the presence of electrostatic charges generated by the triboelectric effect. By investigating whether the cohesion of granular materials is influenced by the triboelectric effect, this study seeks to offer new insights into the understanding of granular material cohesion. Specifically, this investigation focuses on granular flow, which is significantly influenced by cohesion, yet has seen limited quantified research in this context.

To test this hypothesis and analyze easily the flow of granular materials in the rotating drum, using numerical simulations seems to be the best option. Moreover, as it requires to model all the interactions between the particles – including cohesion –, the validity of the models proposed to explain the triboelectric effect can be verified if a good agreement is obtained between the simulations and experiments.

In the following sections of this thesis, once the models I have developed for the numerical simulations have been described, the results I obtained in the rotating drum with these simulations will be presented and compared to the experimental results that have been described in section 2.3 *Granular flow in a rotating drum*.

As a first step, a simple model of cohesion will be used to provide a quantified analysis of the influence of cohesion on the flow of granular materials. Then, this simplified model will be replaced by a model of the triboelectric effect inspired by what has been presented in section 2.1 *The triboelectric effect*. If similarities between the flow obtained with the numerical simulations and the flow of cohesive granular materials are observed, then conclusions on the link between cohesion and the triboelectric effect could be drawn.

This thesis is complemented by animations generated from numerical simulations. These animations can be accessed by scanning QR codes, which will redirect you to YouTube. Feel free to adjust the settings on YouTube as needed to visualize the animations with the best resolution (click on  → Quality → Advanced → Select the highest quality). These animations can also be found in the supplementary materials on ORBi.

---

## 4 Numerical simulations

---

The two most popular methods used to reproduce numerically the flow of granular materials are the Finite Element Method (FEM) and the Discrete Element Method (DEM). The first one considers the granular material as a continuous medium. Indeed, as shown in the introductory section of this thesis, granular materials can be regarded as a liquid, a gas or a solid depending on the agitation of the particles. At the macroscopic scale we could thus ignore the existence of grains and apply the continuum mechanics theories that have been briefly discussed in section 2.2 to reproduce the flow, the shearing or the compaction of granular materials.

The second method considers granular materials as they are: a collection of interacting particles. The DEM consists in exerting forces on each individual grain and displace them according to Newton's second law [154]

$$m_i \frac{d^2 \mathbf{r}_i}{dt^2} = \sum_{j \neq i} \mathbf{F}_{i,j} + \mathbf{F}_{\text{ext}}, \quad (6)$$

with  $i = 1, \dots, N$  where  $N$  is the number of grains in the simulation,  $m_i$  is the mass of grain  $i$ ,  $\mathbf{r}_i$  is the position of grain  $i$ ,  $\mathbf{F}_{i,j}$  are the contact forces exerted by particle  $j$  on particle  $i$  (contact forces with the container are also considered similarly) and  $\mathbf{F}_{\text{ext}}$  are the long-range interaction forces [155]. This method offers

the possibility to implement all kinds of interaction between the particles or with the container.

As the objective of this thesis is to understand the behavior of granular materials resulting from electrostatic interactions between the grains, the FEM is not suitable as it neglects the existence of grains. However, DEM fits particularly well to the objective of this thesis.

### 4.1 The Discrete Element Model (DEM)

The accuracy and the resemblance to realistic granular flows of the DEM simulations lies in a correct modeling of the forces applied on the grains. The fundamental interactions that must be implemented to reproduce the flow of granular materials made of spherical particles are:

- the weight of the particles  $m_i \mathbf{g}$ ,
- the repulsion between the particles touching each other or exerted by the container on a particle in contact with it,
- the friction exerted on a couple of particles sliding on each other or on a particle sliding on the container,
- the rolling friction applied on a couple of particles rolling one onto the other or on a particle rolling on the container and
- the spinning friction on a couple of particles spinning one onto the other or on a particle spinning on the container.

#### 4.1.1 Normal force / repulsion

To model the repulsion between two particles touching each other, it is assumed that particles can overlap on a short distance. Let us consider two grains  $i$  and  $j$  with radii  $R_i$  and  $R_j$ . As shown in figure 31(left), the distance from surface to surface between these two grains is given by

$$\delta_n = |\mathbf{r}_i - \mathbf{r}_j| - R_i - R_j. \quad (7)$$

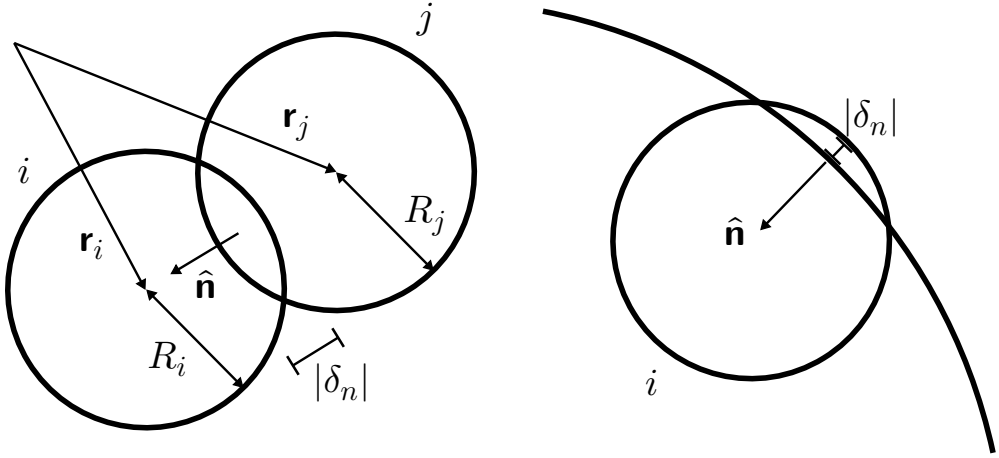


**Figure 31:** The overlap between two particles  $i$  and  $j$  with radii  $R_i$  and  $R_j$  (left) or between a particle  $i$  and the drum with radius  $R_d$  (right) is given by  $\delta_n$  and eqs.(7) and (8).

Similarly, the distance from the surface of a particle  $i$  to the drum, centered in  $\mathbf{r}_0$  that has a radius  $R_d$  is given by

$$\delta_n = R_d - |\mathbf{r}_i - \mathbf{r}_0| - R_i. \quad (8)$$

If  $\delta_n < 0$ , it implies that particles are overlapping and a repulsive force must be applied on the grains. To model the repulsive force at contact between the grains, it is common to consider the contact as a spring that initiates once the particles overlap and whose elongation is given by  $\delta_n$ . In this case, the normal force exerted on particle  $i$  is given by

$$\mathbf{F}_n = \begin{cases} \mathbf{0}, & \delta_n > 0 \\ -k_n \delta_n \hat{\mathbf{n}}, & \delta_n < 0 \end{cases}, \quad (9)$$

where the unitary normal vector is given by  $\hat{\mathbf{n}} = \frac{\mathbf{r}_i - \mathbf{r}_j}{|\mathbf{r}_i - \mathbf{r}_j|}$  (or  $\hat{\mathbf{n}} = -\frac{\mathbf{r}_i}{|\mathbf{r}_i|}$  if the particle is in contact with the drum, see figure 31(right)) and  $k_n$  is the spring stiffness that must be chosen so that the overlap between the grains remains sufficiently small. The opposite force is also exerted on particle  $j$ . However, this expression does not take into account the dissipation of energy that occurs during the contact and should be added. Therefore, a damping force proportional to the relative normal

velocity of contact is exerted on the particles during the time of contact and eq.(9) becomes

$$\mathbf{F}_n = \begin{cases} \mathbf{0}, & \delta_n > 0 \\ -k_n \delta_n \hat{\mathbf{n}} - \eta_n \mathbf{v}_n, & \delta_n < 0 \end{cases}, \quad (10)$$

where  $\eta_n = -2 \ln(\epsilon) \sqrt{\frac{m^* k_n}{\ln^2(\epsilon) + \pi^2}}$  is the viscous damping constant which depends on the coefficient of restitution  $\epsilon$  and the effective mass  $m^* = \frac{m_i m_j}{m_i + m_j}$  and  $\mathbf{v}_n = (\mathbf{v}_i - \mathbf{v}_j) \cdot \hat{\mathbf{n}}$  is the relative normal velocity of the two grains in contact moving at velocities  $\mathbf{v}_i$  and  $\mathbf{v}_j$ . One just has to make sure that an attractive force is not applied on the particles which could happen when damping is high, *i.e.* when  $\mathbf{v}_n > 0$  (*i.e.* when the particles separate) or when  $\eta_n \gg$ . One thus has to check that  $|\mathbf{F}_n| > 0$  before exerting the normal force on the grains. If it is not the case, no normal force is applied on the grain,  $\mathbf{F}_n = \mathbf{0}$ .

#### 4.1.2 Tangential force / friction

A similar model based on an elongated spring along with Coulomb's friction law can be used to exert a friction force on the grains once they are sliding. In the static friction regime, this tangential spring elongates to exert a friction force on the particles that tends to prevent them from sliding one onto the other,

$$\mathbf{F}_t = -k_t \delta_t \hat{\mathbf{t}} - \eta_t \mathbf{v}_t, \quad (11)$$

where  $k_t$  is the tangential spring stiffness,  $\eta_t$  is the tangential viscous damping coefficient and  $\delta_t$  is the tangential relative displacement of the grains that is obtained by integration of  $\mathbf{v}_t \Delta t$  where  $\mathbf{v}_t$  is the tangential velocity of contact and  $\Delta t$  is the simulation's time step. It is generally accepted that the tangential spring and the normal spring stiffness are related. Several constants of proportionality can be found in literature but I have used  $k_t = 2/7 k_n$  [156]. The same proportionality has been used for the viscous damping constants. The tangential velocity of contact  $\mathbf{v}_t$  is given by

$$\mathbf{v}_t = \mathbf{v}_i - \mathbf{v}_j + R_i \hat{\mathbf{n}} \times \boldsymbol{\omega}_i + R_j \hat{\mathbf{n}} \times \boldsymbol{\omega}_j - \mathbf{v}_n, \quad (12)$$

where  $\omega_i$  and  $\omega_j$  are the rotation speeds of the grains so that  $R_i \hat{\mathbf{n}} \times \omega_i$  and  $R_j \hat{\mathbf{n}} \times \omega_j$  are the linear velocities of the grains' surfaces because of their rotation. The tangential unitary vector can then be defined using this tangential velocity as  $\hat{\mathbf{t}} = \frac{\mathbf{v}_t}{|\mathbf{v}_t|}$ .

The tangential spring stretches until  $|\mathbf{F}_t| \geq \mu_s |\mathbf{F}_n|$  where  $\mu_s$  is the static friction coefficient, when the grains start to slide. If this point is reached, then the friction force exerted on the grains is given by Coulomb's law  $|\mathbf{F}_t| = \mu_d |\mathbf{F}_n|$  with  $\mu_d$  the dynamic friction coefficient, to mimic dynamic friction. Because of the use of a spring to model friction, grains could return to their original positions, which is not physical when they slide. To prevent that, a maximal value of  $\delta_t$  is imposed. As  $|\mathbf{F}_t|$  can not exceed  $\mu_d |\mathbf{F}_n|$ , one has

$$\mu_d |\mathbf{F}_n| \text{sgn}(\mathbf{F}_t) = |\mathbf{F}_t| \quad (13)$$

$$= -k_t \delta_t - \eta_t |\mathbf{v}_t| \quad (14)$$

$$\Rightarrow \delta_t = \frac{\mu_d |\mathbf{F}_n| \text{sgn}(\mathbf{F}_t) + \eta_t |\mathbf{v}_t|}{-k_t} \quad (15)$$

where  $\text{sgn}(\mathbf{F}_t)$  is the signature of  $\mathbf{F}_t$  that gives the sign of  $\mathbf{F}_t$ .

As the friction force is not exerted at the center of the grains, torque must also be exerted on the grains simultaneously. The torque exerted on the grains because of friction is given by

$$\boldsymbol{\tau} = R_i \hat{\mathbf{n}} \times \mathbf{F}_t. \quad (16)$$

### 4.1.3 Rolling friction

Without rolling friction, the grains would roll infinitely on an horizontal plane, without ever stopping. A torque must be exerted on rolling grains to slow down their rotation. Rolling friction is caused by the deformation of the grains at the point of contact as shown in figure 32. A simple model of rolling friction includes a rolling friction coefficient  $\mu_{rol}$  and the rolling friction torque is proportional to the grains' relative linear speed of rotation  $\mathbf{v}_r$  and to the normal force  $\mathbf{F}_n$  [157]. The faster the grain rotates or the larger the normal force exerted on it, the larger

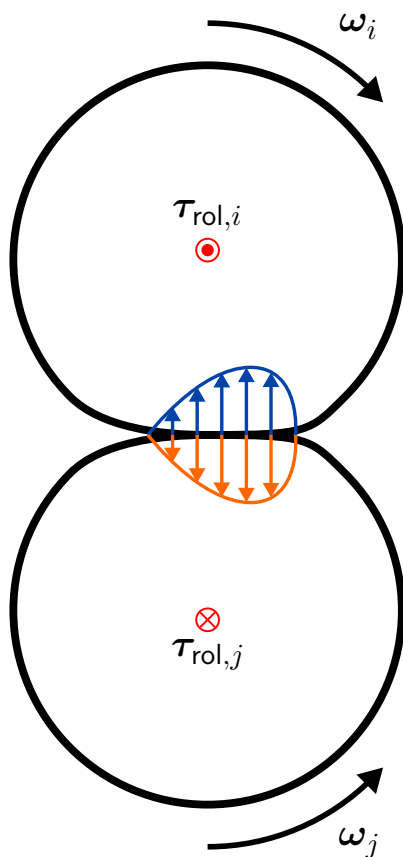


**Figure 32:** The rolling friction arises from the deformation of the grains once they rotate during contact. An asymmetric pressure (in blue on the top grain and orange on the bottom one) is exerted between the grains that are in contact while rotating. It induces a rolling resistance on the grains,  $\tau_{rol,i}$  and  $\tau_{rol,j}$  that slows down their rotation.



the rolling friction torque,

$$\boldsymbol{\tau}_{\text{rol}} = \mu_{\text{rol}} R_i \frac{\mathbf{F}_n \times \mathbf{v}_r}{|\mathbf{v}_r|}, \quad (17)$$

where  $\mathbf{v}_r = R_i \hat{\mathbf{n}} \times \boldsymbol{\omega}_i - R_j \hat{\mathbf{n}} \times \boldsymbol{\omega}_j$ .

#### 4.1.4 Spinning friction

When a grain is immobile on a surface and spins around an axis that is perpendicular to this surface (like a top), a torque must also be exerted on this grain to dissipate this rotation energy. To model spinning friction, the fact that grains overlap is exploited and the radius of overlap between the two grains  $r_c$  is determined as shown in figure 33. The spinning friction torque then also includes a spinning friction coefficient  $\mu_{\text{spin}}$ , the normal force exerted on the grain  $\mathbf{F}_n$  and the relative spin velocity between the grains  $\boldsymbol{\omega}_i - \boldsymbol{\omega}_j$  [157],

$$\boldsymbol{\tau}_{\text{spin}} = -\mu_{\text{spin}} r_c \mathbf{F}_n \frac{(\boldsymbol{\omega}_i - \boldsymbol{\omega}_j) \cdot \hat{\mathbf{n}}}{|\boldsymbol{\omega}_i - \boldsymbol{\omega}_j|}. \quad (18)$$

With these four fundamental interactions (normal and tangential forces as well

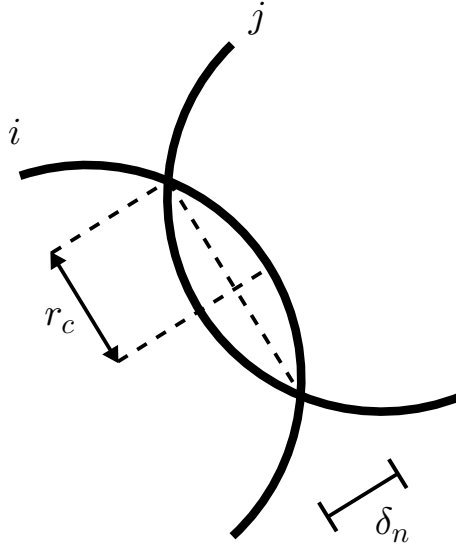


**Figure 33:** To model spinning friction, the radius of overlap between the two grains  $r_c$  is required.

as rolling and spinning friction), the flow of granular materials made of hard spherical particles such as glass beads can be reproduced.

The values of all the parameters that define the interactions described above for typical simulations are given in table 3.

Parameter	Value
$k_n$	200
$\epsilon$	0.7
$\mu_s$	0.8
$\mu_d$	0.6
$\mu_{\text{rol}}$	0.005
$\mu_{\text{spin}}$	0.005

**Table 3:** Parameter values for typical numerical simulations.

#### 4.1.5 Displacement of the grains

The first step of the numerical simulation is to set the initial conditions. The grains are defined with a radius and a mass and their position, velocity and acceleration are set. The initial velocity and acceleration of the grains are both set to zero and the grains are placed randomly in the drum by making sure that they do not overlap. A typical first frame showing the particles at time  $t = 0$  s is shown in figure 34. To compute the trajectory of all the grains resulting from the interactions described in the previous section, the whole time of the simulation (which is one of the simulation's parameters) is divided into smaller time steps  $\Delta t$ .

Once the particles are placed, the forces that are exerted on each individual particle are computed and a resulting force  $\mathbf{F}_i$  is determined. In general, as the particles do not touch each other at the first time step, only weight is applied on each of them. The acceleration of each grain can then be calculated using Newton's second law,

$$\mathbf{a}_i = \frac{\mathbf{F}_i}{m_i}, \quad (19)$$

where  $\mathbf{a}_i$  and  $m_i$  are respectively the acceleration and the mass of grain  $i$ . The velocity and the position of each grain can then be integrated.

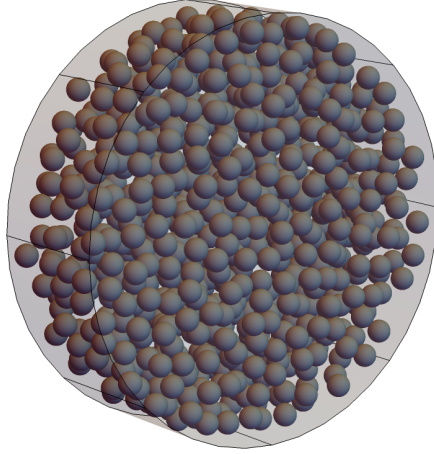


**Figure 34:** Typical first frame of a numerical simulation showing the initial conditions. The grains in the rotating drum at time  $t = 0$  s do not overlap, are placed randomly in the drum and their velocity and acceleration are set to zero.

To reduce the errors and avoid as much as possible divergence from the real trajectory, the leapfrog integrator [155] has been used. It consists in calculating the acceleration and the position at each time step and the velocity at each half time step. Let the position of a grain at the  $k$ th time step, at time  $t = k\Delta t$  be written  $\mathbf{r}^k$ , its velocity at time  $t = (k + 1/2)\Delta t$  be written  $\mathbf{v}^{k+1/2}$  and its acceleration at  $t = k\Delta t$  be  $\mathbf{a}^k$ . The grains are displaced step by step using

$$\begin{aligned}\mathbf{v}^{k+1/2} &= \mathbf{v}^{k-1/2} + \mathbf{a}^k \Delta t \\ \mathbf{x}^{k+1} &= \mathbf{x}^k + \mathbf{v}^{k+1/2} \Delta t\end{aligned}\quad (20)$$

However, this algorithm does not give access to the velocity of the grains at  $t = k\Delta t$  which is required to compute some of the interactions that have been described in the previous section such as the damping forces. To get around this problem, the velocity is also calculated at each time step using

$$\mathbf{v}^k = \mathbf{v}^{k-1/2} + \mathbf{a}^{k-1} \Delta t / 2. \quad (21)$$

The definition of the time step is primordial, a too large time step would make it impossible to solve rapid collisions while a too short time step would pointlessly increase the number of evaluations and thus the computation time. A compromise should be found. In the simulations, the time step has been determined so that a collision lasts about twenty time steps.

If the interactions between all the grains had to be calculated at each time step, there would be  $N^2$  possible interactions to check each time while only a few of them will effectively occur. Indeed, it is not likely that a grain at the bottom of the container enters in contact with a grain at the top of the container if they are separated by several layers of grains. Therefore I used an optimization method to reduce the number of tests at each time step, the Verlet list. It consists in dividing the whole simulation space into cells whose size is proportional to the range of interaction between the grains. Each cell contains a few grains that are susceptible to touch each other or touch the grains in neighbouring cells. This way, only the most likely interactions are tested at each time step which eventually reduces considerably the number of calculations and the time of computation.

## 4.2 Tribocharging

The objective of this thesis is to reproduce the flow of granular materials that charge because of the triboelectric effect. As grains charge, electrostatic interactions between them increase and should be included in the list of forces that are implemented in the numerical simulations. But before electrostatic interactions are applied on the grains, the charge transfer mechanism should be defined. A decision had to be made on which theory reproduces the best the charging of granular materials considering the still active debate in the tribocharging community. In view of the large number of evidences pointing to the patch model that have been discussed in section 2.1 of this thesis and the fact that numerical simulations could provide new insights on the validity of this model, I adapted the patch model so that it reproduces the charging of granular materials in my simulations.

To explain the transfers of charges that occur at contact between identical materials such as the particles of granular materials, the patch model considers

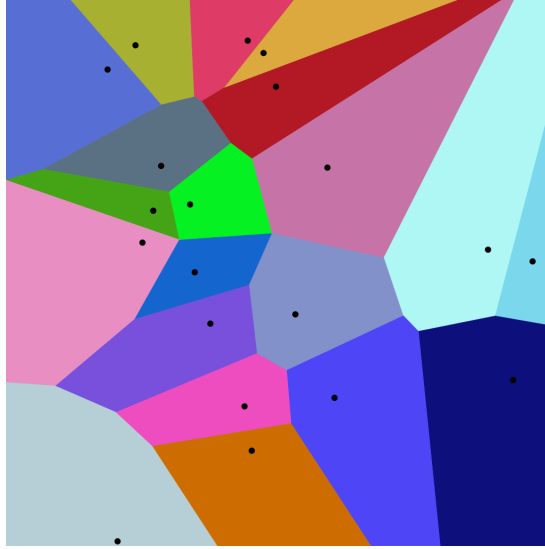


**Figure 35:** Voronoi diagram obtained from 20 points. Each colored region corresponds to a Voronoi cell associated to one point of the set – the generator. All points within the cell are the closest to their generator. Taken from Wikipedia – Voronoi diagram.

that there exists some patches at the surface of objects that can either give or receive a certain amount of charges (as seen in section 2.1.5). Most numerical studies using the patch model have considered flat surfaces contacting [39, 40] and a direct division in squares of the objects' surfaces is thus valid to create these patches. This technique does not work for the curved surfaces of the spherical grains. To pave the whole surface of the grains uniformly with roughly identical patches, I used the Voronoi tessellation [158].

To define a Voronoi tessellation of a plane, a set of points within this plane first has to be defined – the generators. One can then define regions with all locations in the plane that are the closest to one member of the point set. This process results in a tessellation of the plane, where each cell is associated to a distinct generator as shown in figure 35.

To define uniform patches on a grain's surface, generators are first placed at random positions along the grain's surface. If two random angles  $\theta \in [0, 2\pi]$  and  $\phi \in [0, \pi]$  are generated to express the point's position in spherical coordinates, the

distribution is not uniform with a higher density of points at the poles, close to  $\phi = 0$  and  $\phi = \pi$ . To generate a uniform distribution of points on a spherical surface, one rather has to pick two random variables between 0 and 1. Let  $u$  and  $v$  be these two variables, the angles  $\theta$  and  $\phi$  that yield a uniformly distributed set of points on the spherical surface are given by

$$\begin{aligned}\theta &= 2\pi u \\ \phi &= \text{acos}(2v - 1)\end{aligned}\quad (22)$$

The position of a first generator on the surface of a grain  $i$  with radius  $R_i$  in the grain's reference frame is then given by

$$\begin{aligned}x &= R_i \cos\theta \sin\phi \\ y &= R_i \sin\theta \sin\phi \\ z &= R_i \cos\phi\end{aligned}\quad (23)$$

However, placing generators without taking into consideration the distances between them yields non uniform cells with large disparities of their sizes as shown in figure 35. To control the uniformity of the patches' shape and size, each time a new position is generated, the distances between this candidate generator and all the other ones that are already placed are determined. Let  $\mathbf{r}_t$  be the position of the new point and  $\mathbf{r}_i$  the positions of the generators already placed on a grain  $A$  with radius  $R_A$ . The distance between this new point and the other generators is given by

$$d_i = R_A \text{acos}\left(\frac{\mathbf{r}_t \cdot \mathbf{r}_i}{|\mathbf{r}_t| |\mathbf{r}_i|}\right)\quad (24)$$

If this candidate is too close to another generator already in place (*i.e.* if  $d_i < d_0$  where  $d_0$  is a critical minimum distance), then a new random position is determined and the distances to the other generators are checked again. The operation is repeated until an adequate position that satisfies the minimum distance condition is found. By varying  $d_0$ , one can control the patches' shape. This initialization of a new generator is repeated until the number of desired patches on the grain has been reached.

Now that the patches are defined, each of them has to receive a role as they could be donors or acceptors of charges. I defined a patch donor probability  $p$  as the

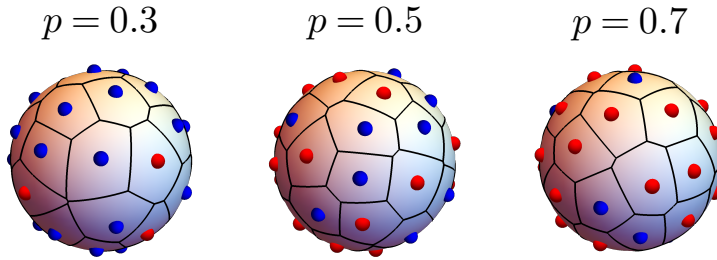


**Figure 36:** Patches on a particle obtained using a Voronoi diagram where red and blue points are the generators that are required to define the Voronoi tessellation. Red patches are donor patches and blue patches are acceptor patches. By varying the path donor probability  $p$ , the density of donors and acceptors can be controlled as illustrated here for 3 different values of  $p$ .

ratio between the number of donor patches  $n_d$  and the total number of patches on the grains  $n$ ,

$$p = \frac{n_d}{n}. \quad (25)$$

Each time a new patch is placed during the initialization of the simulation, a random number is picked between 0 and 1 using a uniform distribution. If this number is smaller than  $p$  then the patch is initialized as a donor patch and if the random number is larger than  $p$ , the patch is an acceptor. For example, when  $p = 0.5$ , there are as many donor than acceptor patches on the grains but if  $p = 0.2$ , there are 20% of donors and 80% of acceptors in average. This method finally results in a distribution of patches on the grains' surface such as shown in figure 36.

Next, the transfer of charges between the grains must be defined. The charge transfer mechanism of the patch model considers that if a donor patch on one object touches an acceptor patch on an other object, a negative amount of charges is transferred from the donor to the acceptor. In my simulations, a transfer of charges could thus possibly occur each time a contact between two grains is detected (*i.e.* when  $\delta_n < 0$ , as seen in section 4.1.1). Once the position of the contact has been determined in both particles' reference frames, the definition of the Voronoi tessellation is applied to find which patches are in contact. By

definition, the contact occurs in the patch whose generator is the closest to the point of contact. If a donor on one particle is touching an acceptor on the other one, the transfer of charges occurs.

To reduce the number of patches on the particles and thus the number of interactions and the computation time, I considered that a patch could charge 10 times before reaching its maximum saturation charge  $q_{max}$ . Even though such multiple charging is not supposed to occur for repeated contacts on a single patch, it is still consistent with the charge transfer mechanisms of the patch model. Indeed, as discussed in the state of the art section on the patch model, it has been shown in numerical simulations that patches can be considered as a collection of individual donor or acceptor sites [39]. One can actually define three length scales, the microscopic scale of the size of individual donor and acceptor sites, the macroscopic scale of the object's size and an intermediate mesoscale of the patches' size which are just a collection of sites. Within this patch all the sites might not be touching a site of the other kind during a contact and successive contacts might be required to charge the whole patch as shown in figure 37. Therefore, the multiple charging of the patches makes sense and has a physical interpretation. In the simulations, once a patch has been charged 10 times, it cannot exchange charges anymore.

As particles charge, electrostatic interaction must be implemented in the simulations. When two charged particles A and B are close to each other, each pair of charged patches on both particles creates an attractive or repulsive force on the particles which is given by Coulomb's law. The force applied on particle A at the position of its charged patch  $i$  because of the charged patch  $j$  on particle B is thus given by

$$\mathbf{F}_{ij} = \sum_{\substack{i \in A \\ j \in B}} -k_e \frac{q_i q_j}{|\mathbf{r}_{ij}|^2} \frac{\mathbf{r}_{ij}}{|\mathbf{r}_{ij}|} = -\mathbf{F}_{ji}, \quad (26)$$

where  $k_e = 9.10^9 \text{ N}\cdot\text{m}^2\cdot\text{C}^{-2}$ ,  $q_i$  and  $q_j$  are the charges of the patches  $i$  and  $j$  on particles A and B respectively and  $\mathbf{r}_{ij}$  is the vector pointing from patch  $i$  to patch  $j$ . To decrease the size of the cells and the number of interactions between particles to test, it is considered that as dense granular flows are simulated, the electrostatic interaction that one particle might exert or feel from particles further



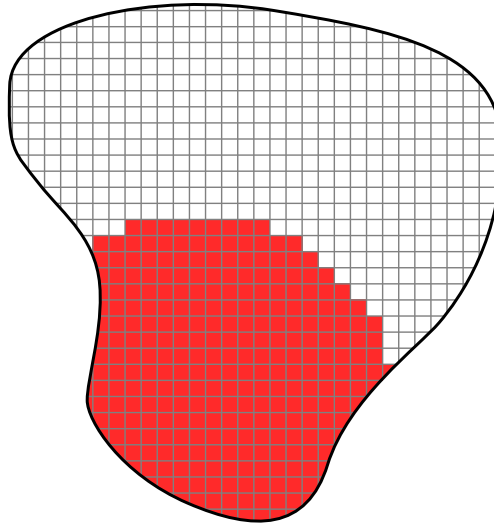


**Figure 37:** A patch is considered as a collection of identical sites. A random donor patch is represented here as a collection of microscopic donor sites. This patch can be only partially charged as illustrated by the red sites because of a contact with an acceptor patch. Only the donor sites that have been in contact with acceptor sites are charged resulting in a donor patch that can still be charged.

than 2 grain diameters (center to center) are screened by particles in between. A cut-off distance has been set for this force at one grain diameter, if the distance that separates two charged patches is larger than one grain diameter, no interaction is considered. As these forces are applied on the surfaces of the particles at the positions of the patches, torques are also applied on the particles and generate particle rotation.

### 4.3 Analysis of granular flow

To determine how the flow of granular materials is influenced by cohesion, I developed an analysis code to obtain the dynamic angle of repose, the velocity profile and the fluctuations of the interface.

The dynamic angle of repose requires to fit the grain-air interface. The drum is first divided in classes whose width is equal to one grain diameter. For each output file of the simulation at which the positions of the grains have been recorded, the whole list of grains is scanned and the highest grain's position in each class is kept

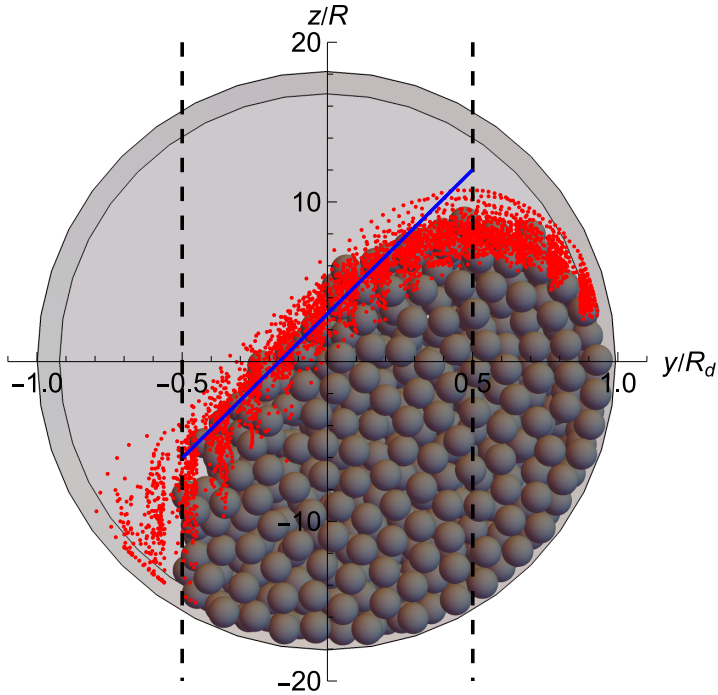


**Figure 38:** Detection of the interface for the measurement of the dynamic angle of repose and the velocity profile. In each output file of the simulation, the interface is detected. All the interfaces are shown by the red points and normalized by the drum's radius  $R_d$  ( $y$  axis) and the grains' radius  $R$  ( $z$  axis). This list is then used to fit the interface (blue line) in the central part of the drum (delimited by vertical dashed lines), which is required to perform the desired measurements.

in memory. What I obtain is a list of points that contains each interface in each output file as shown in figure 38. The least squares fitting is then used to obtain a linear fit of the interface in the central region of the drum only to avoid fitting an S-shape interface as discussed in section 2.3.2. Let  $z = ay + b$  be this linear fit, the dynamic angle of repose is then given by

$$\theta = \text{atan}(a). \quad (27)$$

The linear fit of the interface is then also used to measure the velocity profile. For this measurement, the velocity of the grains passing in a thin layer perpendicular to the interface must be determined. The method used to measure the velocity profile in the simulations is shown in figure 39. The velocity profile is measured

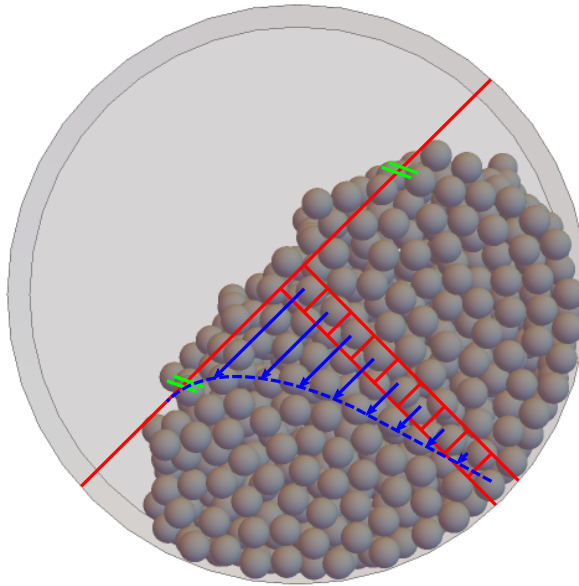


**Figure 39:** To measure the velocity profile in the simulations, the intersections of the interface's linear fit with the wall of the drum are determined. The perpendicular of the interface passing by the middle between these two intersections is then used to define a thin layer with a width of one grain diameter. This layer is then subdivided into square cells. The velocity of the grains located in each of these red cells is averaged over the whole simulation to obtain the velocity profile (in blue).

in a thin layer which is perpendicular to the interface and in the middle of the two intersections between the interface's linear fit and the wall of the drum. The velocity of each grain passing through this thin layer during the simulations is kept in memory to compute the average velocity of the grains with respect to depth in the granular bed  $d$ . The velocity profile is calculated in the rotating drum's reference frame by subtracting  $\omega d$  to the measured velocity.

---

## 5 Influence of cohesion on granular flow

---

Work published in:

Nicolas Preud'homme, Geoffroy Lumay, Nicolas Vandewalle and Eric Opsomer. Numerical measurement of flow fluctuations to quantify cohesion in granular materials. *Physical Review E*, 104(6):064901, 2021.

Nicolas Preud'homme, Geoffroy Lumay and Eric Opsomer. Numerical analysis of cohesive granular materials' flow. *Belgian Journal of Physics*, 2022.

## 5.1 Motivations

Controlling the cohesion of granular materials in experiments is complex. In dry granular materials where liquid bridges play no significant role, cohesive forces are supposed to arise mostly from an effect which is not well understood, the triboelectric effect. Therefore, very few studies characterizing the flow of cohesive granular materials exist. So as a first approach, I have implemented a simple model of cohesion to investigate the flow of cohesive granular materials. This model consists in applying an attractive force on the particles up to a certain range and which is maximum at contact between the particles. By measuring the dynamic angle of repose and the velocity profile, the simulations can be compared to experimental results to validate the models used. The intensity of cohesion can then be easily controlled in the simulations to fully characterize the flow of cohesive granular materials which will serve as a benchmark for further simulations using the patch model.

To reproduce cohesive forces, an attractive force has been applied between each pair of grains. It has been defined arbitrarily to mimic roughly the cohesion in granular materials. A maximum range of action has been defined at one grain radius from surface to surface (*i.e.* at  $\delta_n = R$ ). No attractive force is applied on the grains if the distance that separates them is larger than  $R$ . As shown in figure 40, the force is maximum at contact between the grains and decays quadratically up to  $R$ . To control the intensity of cohesion between the grains, the dimensionless granular Bond number has been used. It is defined as the ratio between the maximum attractive force at contact  $F_0$  and the weight of the grains

$$\text{Bo} = \frac{F_0}{mg}. \quad (28)$$

The expression of the cohesive force exerted on each pair of grains is then given by

$$\mathbf{F}_c = F_0 \left[ \left( \frac{\delta_n}{R} \right)^2 - 1 \right] \hat{\mathbf{n}}. \quad (29)$$

This force is applied at the center of mass of the grains.

To focus on the influence of cohesion only, these simulations have been performed

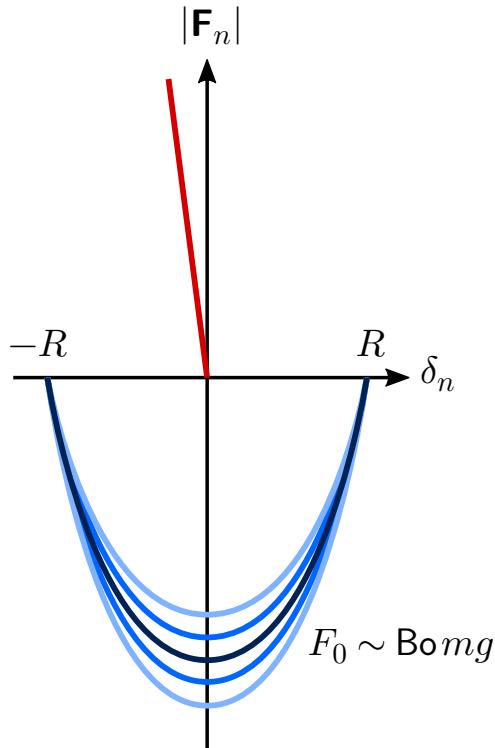


**Figure 40:** The normal forces applied on the grains with a simple model of cohesion used to investigate the influence of cohesion on the flow of granular materials. The attractive force (in blue) is maximum at contact between the grains (*i.e.* at  $\delta_n = 0$ ) and the intensity of this force at contact is proportional to the dimensionless granular Bond number  $Bo$  (light blue curves). The repulsive normal force at contact given by  $k_n \delta_n$  is represented in red.

in 2D to avoid the end wall effect. We could indeed consider that 2D simulations of granular flow correspond to the flow of granular materials at the middle of a long rotating drum, where the influence of the end walls is negligible. In each simulation, the rotating drum is half-filled with 1000 grains, each with a radius 50 times smaller than that of the drum. The grains are also slightly polydisperse. Each simulation with a set of parameters has been repeated 10 times to reduce as much as possible statistical fluctuations and highlight more precisely the influence of the parameters investigated. A few snapshots of the simulations are shown in table 4 to illustrate how the granular flow looks like with and without cohesion.

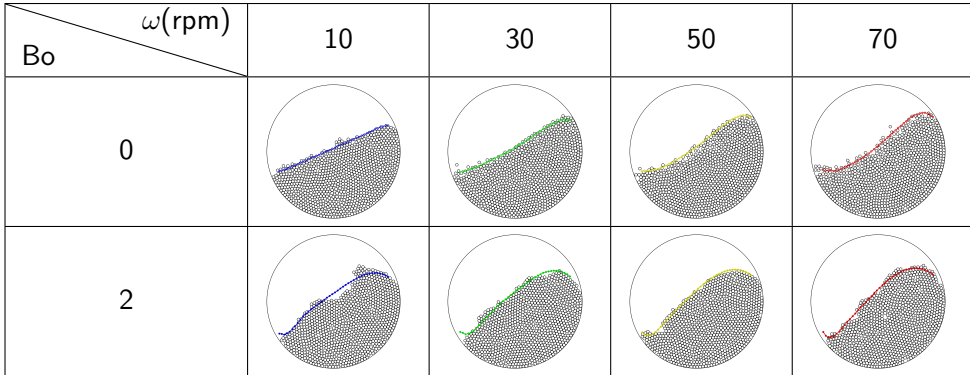


**Table 4:** Snapshots of the numerical simulations without cohesion ( $\text{Bo} = 0$ ) and with cohesion ( $\text{Bo} = 2$ ) for different rotation speeds of the drum. Mean interfaces are represented in colors to highlight the influence of cohesion.

## 5.2 Results

When comparing the velocity profiles obtained for different values of  $\text{Bo}$  shown in figure 41(a), it can be seen that the typical velocity profile of non-cohesive granular materials can be retrieved when  $\text{Bo} = 0$  (purple curve). One can indeed observe that it is linear close to the interface and then decreases exponentially with depth like discussed in section 2.3.2. The results obtained in the numerical simulations with non-cohesive granular materials are thus consistent with experimental results. As  $\text{Bo}$  increases, the velocity profile near the interface flattens, forming a plateau around  $d/R_d = 0$ . This result has also been obtained by Brewster *et al.* as shown in section 2.3.4 and is attributed to the presence of aggregates flowing at the interface like avalanches. For the largest values of  $\text{Bo}$ , one can see that the velocity profile is linear again at the surface indicating that the aggregates start rolling on the granular bed. Finally, one can also observe in this figure that the interface rises when the cohesion increases. The velocity profile's first point for the maximum value of  $\text{Bo}$  lies around  $-0.3d/R_d$  while it is around  $-0.1d/R_d$  for  $\text{Bo} = 0$  indicating that the interface is higher. This is due to the transition of the interface's shape from the S-shape to the convex shape which is also a distinctive feature of cohesive granular materials discussed in section 2.3.4.

When the granular material is cohesive and the rotation speed of the drum increases, one can see that the velocity profile flattens close to the interface as

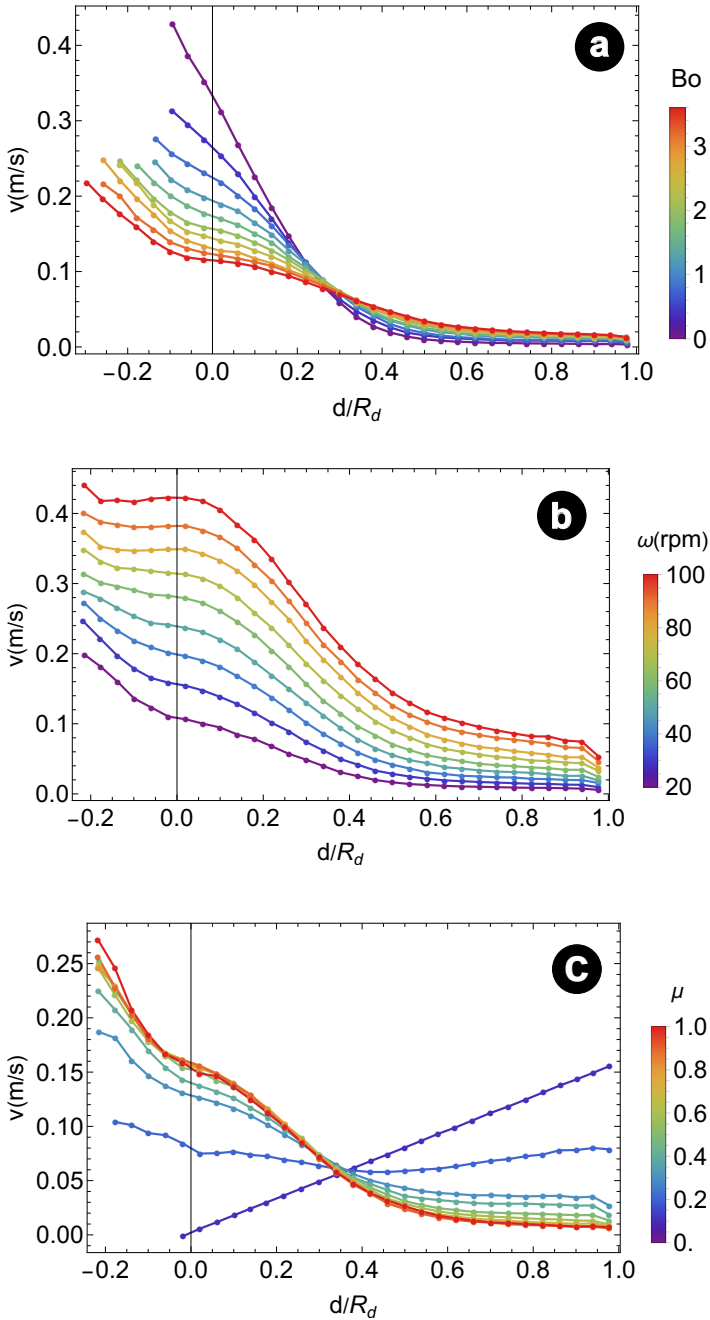


**Figure 41:** Velocity profiles obtained with the 2D numerical simulations of cohesive granular flow in the rotating drum varying the Bond number ( $\omega = 30$  rpm and  $\mu = 0.6$ )(a), the rotation speed of the drum  $\omega$  ( $Bo = 2$  and  $\mu = 0.6$ )(b) and the coefficient of friction between the particles  $\mu$  ( $\omega = 30$  rpm and  $Bo = 2$ )(c). They are expressed as a function of depth in the granular bed  $d$ , where  $d = 0$  corresponds to the level of the interface, and normalized by the drum's radius  $R_d$ .



shown in figure 41(b). The depth over which the velocity of the grains is constant increases with  $\omega$ . If we refer to the classification of the flow regimes presented in section 2.3.1, the granular flow obtained in the numerical simulations at the largest values of  $\omega$  should be in the cataracting regime which is characterized by the take-off of grains from the interface. Because of cohesion, these grains will agglomerate more easily which will eventually increase the size of the aggregates. There should thus be a deeper layer of grains flowing at the same velocity at the interface as shown in the velocity profile measurement. When  $\omega$  increases, it can also be seen in this figure that the velocity of the grains in contact with the drum (*i.e.* at  $d/R_d = 1$ ) is no longer null. In the rotating reference frame used to measure the velocity profile, this indicates that the grains move slightly slower than the drum. As the rotation speed of the drum increases, the shear rate imposed by the drum on the grains is too large and the grains start sliding on the drum.

Finally, the influence of the coefficient of friction has been investigated. The velocity profiles obtained by varying  $\mu$  are shown in figure 41(c). For the smallest value of  $\mu$ , the velocity of the grains is given by  $\omega d$ . The grains thus seem to be all at rest in the laboratory's reference frame as friction is too weak to prevent them from sliding on the drum. As  $\mu$  increases, grains progressively move at the same velocity than the drum. From  $\mu = 0.6$ , the velocity profile is not further influenced by the coefficient of friction.

The influence of the three parameters  $Bo$ ,  $\omega$ , and  $\mu$  on the dynamic angle of repose has been investigated to further understand the effect of cohesion on granular flow. Starting with a non-cohesive granular material, one can first see in figure 42(a) that  $\theta$  increases linearly with  $\omega$  and the slope changes around 50 rpm. This result is in agreement with the experimental results that were obtained for ideal, non-cohesive granular materials which are discussed in section 2.3.2, the change of slope being interpreted by the apparition of the S-shaped interface. If the granular material is cohesive,  $\theta$  increases linearly without any change of slope within the range of  $\omega$  investigated. This indicates that the change of the interface's shape either occurs at another value of  $\omega$  or does not occur at all.

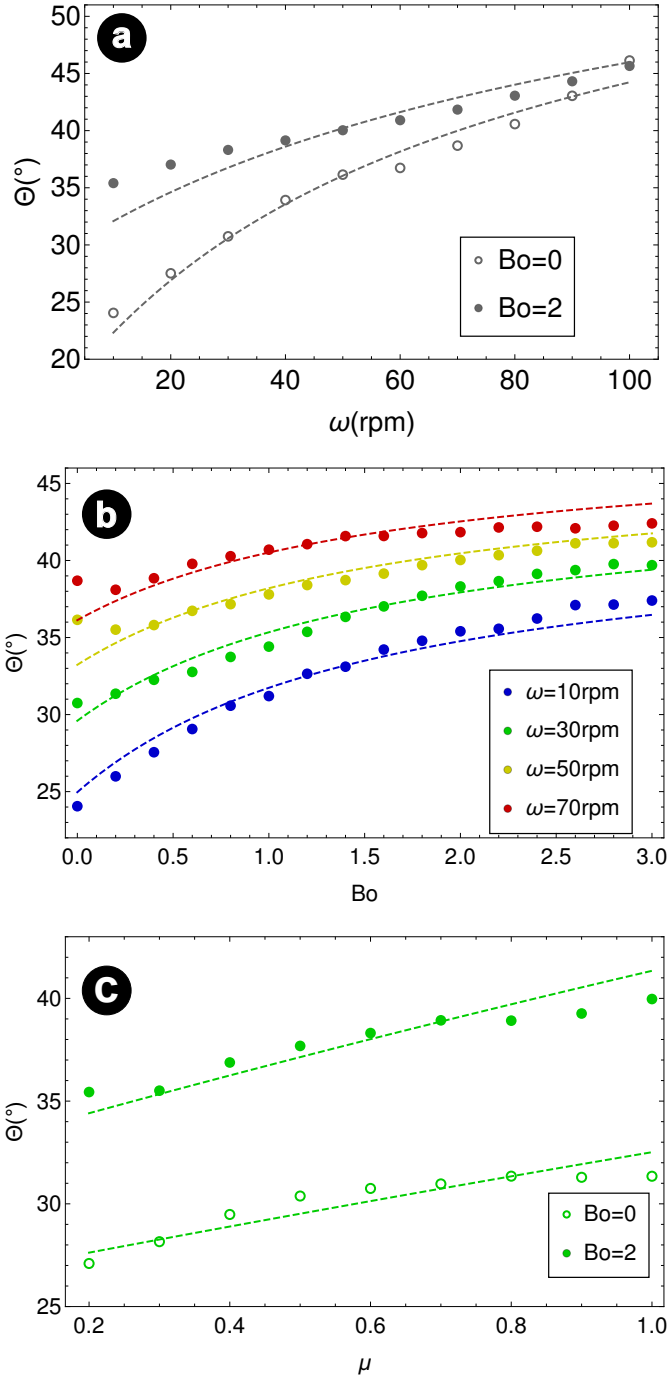


**Figure 42:** Dynamic angle of repose obtained with the 2D numerical simulations of cohesive granular flow in the rotating drum varying the Bond number ( $\mu = 0.6$ ) (a), the rotation speed of the drum  $\omega$  ( $\mu = 0.6$ ) (b) and the coefficient of friction between the particles  $\mu$  ( $\omega = 30$  rpm) (c). Dashed curves have been obtained using the model given by equation (42).

The interface's shape is also influenced by cohesion as can be seen in figure 42(b). When  $Bo$  increases,  $\theta$  first increase and saturate for large intensities of cohesion. As indicated by Brewster *et al.* [150], this results from a competition between the inertia of the grains that depends on the rotation speed of the drum which tends to make the interface S-shaped and cohesion which tends to make the interface convex. When  $Bo$  is high, cohesion overcomes inertia. The dynamic angle of repose thus remain constant as the interface is convex and does not change anymore.

When the coefficient of friction is varied for cohesive and non-cohesive granular materials, one can observe in figure 42(c) that  $\theta$  slightly increases with  $\mu$  up to  $\mu = 0.6$ . From this value of  $\mu$ ,  $\theta$  does not seem to be further influenced by the coefficient of friction. Note that the value of  $\theta$  for  $\mu = 0.1$  is not shown here, as it is equal zero due to the flat interface of the immobile granular bed. Sliding of the grains on the drum can still be expected for larger values of  $\mu$  hence the lower values of  $\theta$  for  $\mu < 0.6$ .

The analysis of the velocity profiles and dynamic angles of repose indicates that cohesive granular flows are characterized by the formation of aggregates flowing along a convex-shaped interface. To further analyze these cohesion-induced aggregates, the vertical fluctuations of the interface were measured to evaluate their typical size, as shown in figure 43. Using the list of points at the interface that had been obtained to measure the dynamic angle of repose (see figure 38), the standard deviation of the interface's vertical position is given by

$$\sigma(y) = \sqrt{\frac{1}{n} \sum_{i=1}^n (z_i - \bar{z})^2}, \quad (30)$$

where  $\bar{z}$  is the mean vertical position of the interface. This measurement of fluctuations thus slightly differ from the one proposed by Espiritu *et al.* [152] but captures what occurs specifically at the interface.

With non-cohesive granular materials, the fluctuations are constant over the whole interface as can be seen in figure 44(a). Moreover, they are equal to 2 grains radii, indicating that there are no aggregates at the interface when  $Bo = 0$ . When  $Bo$

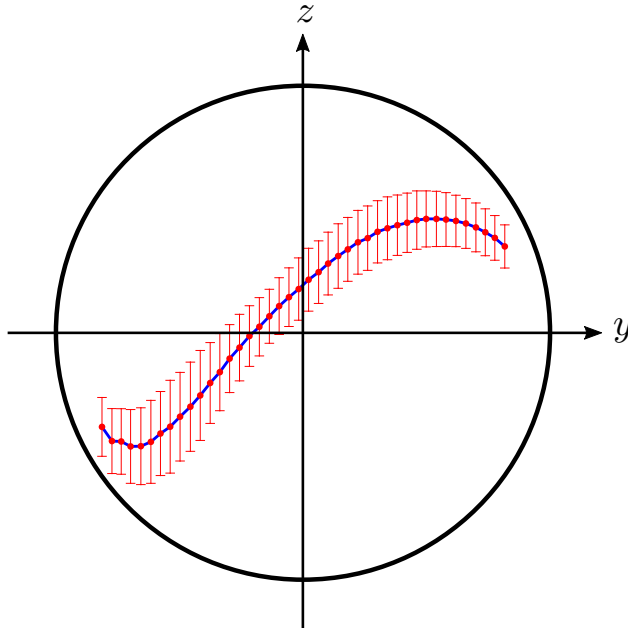


**Figure 43:** Measurement of the fluctuations of the interface given by the standard deviation of the interface's height (in red). The mean interface is represented in blue.

increases, one also observes that fluctuations increase all along the interface with larger fluctuations at the top of the flowing layer, around  $y = 0.5R_d$  and at the bottom of the flowing layer, around  $y = -0.5R_d$ . The peak in interface fluctuations at the top of the flowing layer can be interpreted as follows. When  $Bo$  increases, grains are more strongly attracted by each other and larger aggregates can be formed. As the drum rotates between two avalanches, the dynamic angle of repose gradually increases. As the shear stress applied on the aggregate of particles by weight increases with the angle of repose, there comes a point when it is sufficient to detach the aggregate from the granular bed and trigger an avalanche. The surface then consequently lowers until a new aggregate is formed by the rotation of the drum which explains why large fluctuations are measured at the top of the flowing layer. Once the avalanche has started, the aggregate flows down on top of a slower granular bed. Because of friction, the aggregate is sheared and flattens. Hence the lower fluctuations at the center of the drum. The aggregate finally reaches the bottom of the flowing layer where it hits the wall of the drum. Depending on the size of the aggregate, it takes some time to carry all the grains

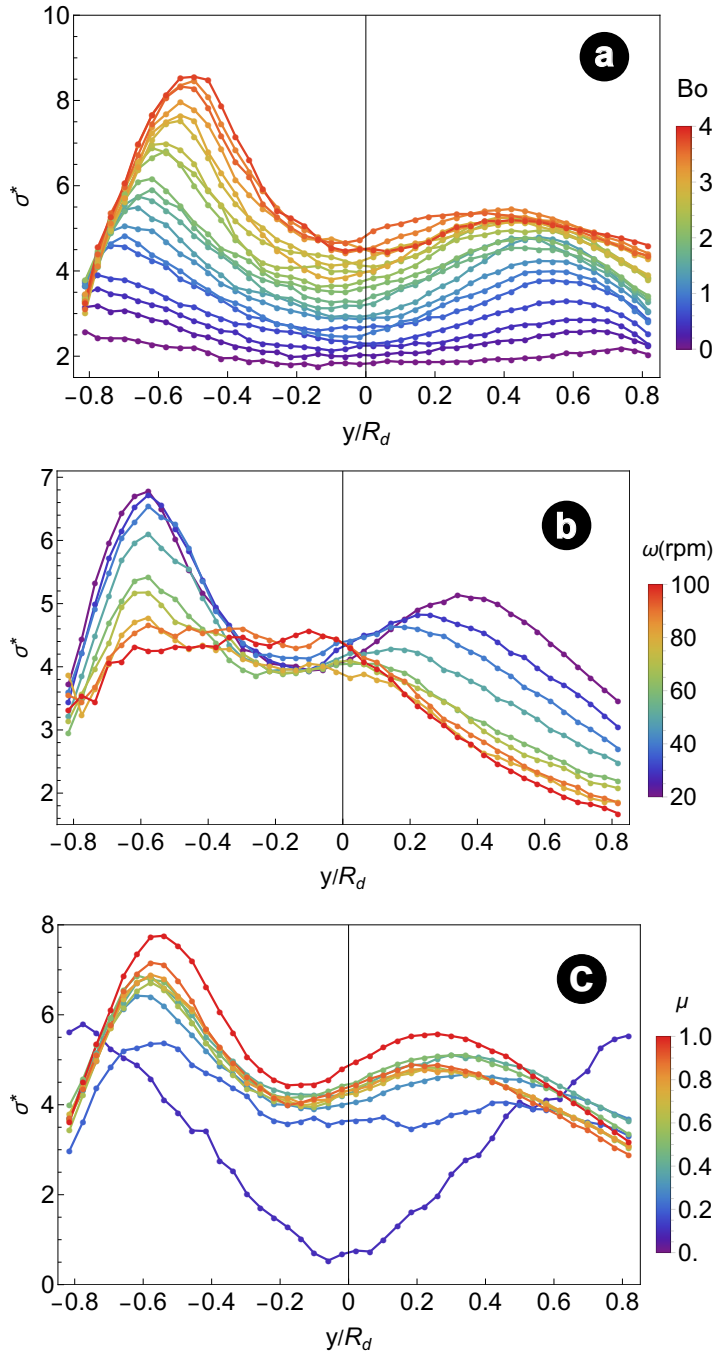


**Figure 44:** Fluctuations of the interface which defined as the standard deviation of the interface's height, given by eq.(30). The fluctuations are normalized by the grains' radius  $\sigma^* = \sigma/R$ . The influence of  $Bo$  (a), the rotation speed of the drum  $\omega$  (b) and the coefficient of friction (c) are shown. The default values are  $Bo = 2$ ,  $\omega = 30$  rpm and  $\mu = 0.6$ .

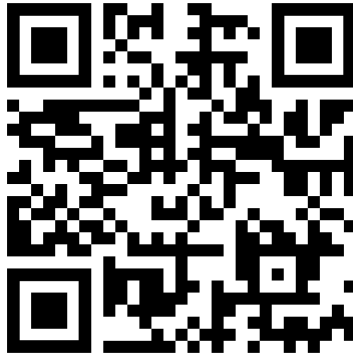


**Figure 45:** Video of the flow of a cohesive granular material in a 2D rotating drum. In this simulation,  $Bo = 4$ ,  $\omega = 30$  rpm and  $\mu = 0.6$ .

back up to the top of the flowing layer. The interface thus greatly fluctuates at the bottom of the flowing layer when  $Bo$  is high as the aggregates should be larger. This dynamic of the aggregates can be viewed in the simulations by scanning the QR Code shown in figure 45.

Interestingly, when the rotation speed increases, the fluctuations of the interface decrease as can be seen in figure 44(b). As the grains are less strongly bonded to the granular bed because of the centrifugal force, aggregates are more easily freed from the interface and are thus smaller. Moreover, as the dynamic angle of repose of the granular bed increases with  $\omega$  (as discussed previously in figure 42(a)), the shear stress applied on the aggregates is larger which also contributes to reduce the fluctuations at the top of the flowing layer. As the drum is rotating faster, aggregates do not accumulate as much at the bottom of the flowing layer but are rather more rapidly evacuated back up to the top.

The sliding of the grains when the coefficient is too low can also be seen in the measurement of the fluctuations which are shown in figure 44(c). However, this measurement allows to see that the granular bed is actually in a stick-slip motion when  $\mu = 0.1$  which was not visible in the measurements of  $\theta$  and the velocity profile. Indeed, the linear increase of the fluctuations on either side of the drum's center indicates that the interface goes up and down.

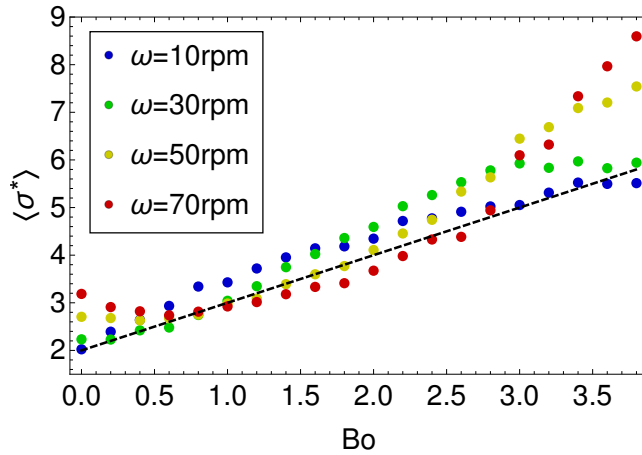


**Figure 46:** Measurement of the mean interface fluctuations. Dashed black line has the expression  $Bo + 2$ .

These fluctuation measurements strongly indicate that aggregates form at the interface due to cohesion, as also observed in the velocity profiles and angle of repose. To determine an approximate mean size of the aggregates, the mean interface fluctuations  $\langle \sigma^* \rangle$  shown in figure 46 have been determined by taking the mean of each of the  $\sigma^*(y)$  curves that have been presented in figure 44(a). Other rotation speeds have been considered for comparison. It can be seen that the mean fluctuations increase with  $Bo$ , implying that the size of the aggregates is increasing when the cohesion is larger which was expected. Moreover, within a certain range of  $Bo$  between 0.5 and 3, it seems that the mean fluctuations increase linearly with  $Bo$  with no influence of the rotation speed. In this range, the mean fluctuations depend on cohesion only and are roughly given by  $Bo + 2$  as can be seen in figure 46. One could thus consider that the size of the aggregates is determined mostly by cohesion and so that the mean interface fluctuations and cohesion are directly proportional.

The fact that cohesive granular materials exhibit intermittent flows of aggregated grains, rather than a continuous flow of a thin layer of grains significantly alters the classical theories of granular flow. A theory of non-cohesive granular flow in rotating drums from Dury *et al.* [119] has been adapted based on this observation

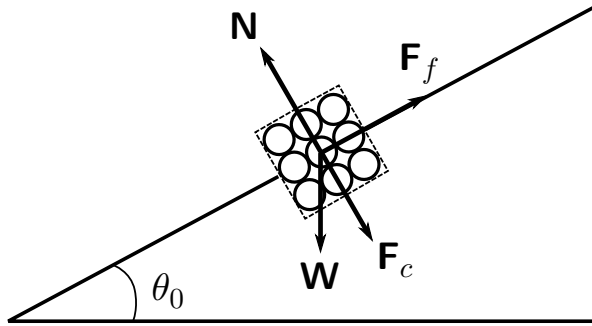


**Figure 47:** Model of cohesive granular flow. It is assumed that the flow of cohesive granular materials consists of the flow of aggregates on top of an inclined granular bed by an angle  $\theta_0$ . The critical angle  $\theta_0$  at which the cohesive granular material flows depend on the weight of the aggregate  $\mathbf{W}$ , the cohesive force applied by the granular bed on the aggregate  $\mathbf{F}_c$ , the friction force applied by the granular bed on the aggregate  $\mathbf{F}_f$  and the normal applied by the granular bed on the aggregate  $\mathbf{N}$ .

to include cohesion. By looking at the flow of a thin layer of grains on top of an inclined granular bed, they managed to obtain an expression for the dynamic angle of repose of ideal granular flows in the rotating drum

$$(z')^3 - (z')^2 \tan \theta_0 + z' + c\omega(z^2 + y^2 - R_d^2) = \tan \theta_0, \quad (31)$$

where  $z' = \tan \theta$ ,  $\theta_0 = \arctan(\mu)$  is the repose angle of the granular bed,  $y$  and  $z$  are the position variables and  $c$  is a parameter that they define as the granular viscosity. When the granular material is cohesive, the angle  $\theta_0$  at which the flow is initiated is not the same than if the material was not cohesive. To determine  $\theta_0$ , it is assumed that the flow of cohesive granular materials consists of the flow of aggregates on top of the granular bed rather than a thin layer of grains. The angle  $\theta_0$  at which the aggregates flow on top of the inclined granular bed can be determined by studying the limit condition at which an aggregate is about to flow using Newton's second law. The problem is represented schematically in figure 47 where the list of interactions that are exerted on the aggregate are shown. Applying Newton's second law along the direction of the inclined plane yields

$$F_f - W \sin \theta_0 = 0, \quad (32)$$



and along the perpendicular of the inclined plane

$$N - F_c - W \cos \theta_0 = 0. \quad (33)$$

Using Coulomb's law of friction and injecting equation (33) in equation (32) yields

$$\mu(F_c + W \cos \theta_0) - W \sin \theta_0 = 0. \quad (34)$$

The solution of this equation according to  $\mu$  is then given by

$$\mu = \frac{W \sin \theta_0}{F_c + W \cos \theta_0}. \quad (35)$$

Using trigonometry, one obtains

$$\mu = \frac{\tan \theta_0}{1 + \frac{F_c}{W} \sqrt{1 + \tan^2 \theta_0}}. \quad (36)$$

As  $\tan \theta_0$  must be positive, the only solution to this equation is

$$\tan \theta_0 = \frac{1 + \frac{F_c}{W} \sqrt{1 + \mu^2 \left[1 - \left(\frac{F_c}{W}\right)^2\right]}}{1 - \left(\frac{F_c}{W}\right)^2 \mu^2}. \quad (37)$$

If  $\mu < 1$ , then  $\mu^2 \ll 1$ , so we can neglect second order terms of  $\mu$ . It remains then that the critical angle at which the aggregate is about to flow is given by

$$\tan \theta_0 = \mu \left(1 + \frac{F_c}{W}\right). \quad (38)$$

In this equation, both  $F_c$  and  $W$  depend on the number of grains  $N$  inside the aggregate. The weight of the aggregate is given by

$$W = Nmg, \quad (39)$$

where  $m$  is the mass of one grain. Concerning the cohesive force applied by the granular bed on the aggregate, let us consider that the aggregate has the shape of a square. The characteristic length of the cluster is given by  $\sqrt{N\pi R^2}$ . This corresponds to the length of contact between the aggregate and the granular bed.

The number of grains in the aggregate that are in contact with the granular bed is thus given by  $\frac{\sqrt{N\pi R^2}}{2R}$ . One obtains that the cohesive force exerted by the granular bed on the aggregate is

$$F_c = \frac{\sqrt{N\pi R^2}}{2R} \text{Bo} mg. \quad (40)$$

To estimate the number of grains that are in the aggregate, the mean interface fluctuations that have been measured in the simulations are used. It has been shown in figure 46 that the mean interface fluctuations scale as  $\text{Bo} + 2$  and give a good estimation of the aggregates' size that are flowing at the interface. As the mean fluctuations indicate that the interface oscillates with an amplitude equal to  $\text{Bo} + 2$ , one can assume that the aggregates that flow at the interface contain roughly  $N = (\text{Bo}/2 + 1)^2$  grains<sup>1</sup>. The ratio  $F_c/W$  is thus given by

$$\frac{F_c}{W} = \sqrt{\pi} \frac{\text{Bo}}{\text{Bo} + 2}. \quad (41)$$

This relation including cohesion is injected in equation (38) which can then be injected in Dury *et al.*'s model given by equation (31). As the dynamic angle of repose  $\theta$  is measured at the center of the drum in the simulations, this equation is solved at the center of the drum (*i.e.* at  $y = 0$  and  $z = 0$ ) using Wolfram Mathematica [159]. The following solution is obtained

$$\tan \theta = \frac{\mu}{3} \left( 1 + \frac{F_c}{W} \right) - \frac{A}{3} \left( \frac{2}{B + \sqrt{4A^3 + B^2}} \right)^{1/3} + \frac{1}{3} \left( \frac{B + \sqrt{4A^3 + B^2}}{2} \right)^{1/3}, \quad (42)$$

where

$$A = 3 - \left( \mu + \frac{F_c}{W} \mu \right)^2 \quad (43)$$

$$B = 18\mu + 18 \frac{F_c}{W} \mu + 27cR^2\omega. \quad (44)$$

This new model now includes the influence of cohesion with the Bond number  $\text{Bo}$ , the influence of the rotation speed  $\omega$  and of the coefficient of friction  $\mu$ . If this equation is plotted on top of our numerical results, one can see in figure 42 that

---

<sup>1</sup>The mean interface fluctuations are expressed in terms of grain radius so we must divide it by 2 to obtain the number of grains along the direction that is perpendicular to the granular bed. It is then squared as we consider that the aggregate is a square.

the expression fits well the data. This agreement between the model and the data confirms the hypotheses that were made to develop the model, the fact that the flow of cohesive granular materials consists of aggregates that flow at the interface.

### **5.3 Conclusions**

The granular flow obtained with the numerical simulations has been analyzed by measuring the dynamic angle of repose and the velocity profile. The flow of non-cohesive granular materials could be compared to experiments and the results from the numerical simulations are in good agreement with the experiments. The contact models used for the simulations thus seem correct as they reproduce a realistic granular flow that resembles what is observed in experiments.

As the implication of electrostatic charges in cohesive forces is still not clear, a simple model of cohesion has been implemented to study the influence of cohesion on the flow of granular materials. An attractive force whose intensity can be controlled through the granular Bond number has been applied between the particles to reproduce cohesion in the simulations. With this cohesive force applied on the grains, the characteristic avalanching flow regime has been observed in the simulations. The flow of aggregates at the interface and the transition of the interface's shape from S-shape to a convex shape are observed in the velocity profiles and in the measurement of the dynamic angle of repose when cohesion is increased.

The specific intermittent flow of cohesive granular materials which is characterized by the flow of aggregates at the interface has been studied in more details by measuring the vertical fluctuations of the interface. The analysis of these interface fluctuations provides insight into the flow of the aggregates formed because of cohesion from their formation at the top of the flowing layer to their evacuation at the bottom of the flowing layer. Moreover, it has been shown that taking the mean value of these interface fluctuations seems to be a relevant measurement to characterize the flow of cohesive granular materials as they only depend on the Bond number. It can thus be a useful measurement to perform in order to quantify the cohesiveness of granular materials as it has been shown that amplitude of the mean fluctuations and the Bond number are proportional.

Based on all these results, a model for the flow of cohesive granular materials has been proposed by adapting a theory that had been developed for ideal, non-cohesive, granular materials. Rather than considering that the flow of granular materials in the rotating drum consists of the flow of a thin layer of grains on top of the granular bed such as in the classical theories, it has been considered that aggregates flow at the interface. The size of the aggregates depends on the intensity of cohesion between the particles and has been approximated using the measurement of the mean fluctuations.

The formation of aggregates thus seems to characterize cohesive granular materials and analyzing these aggregates provides information on the intensity of cohesion. This new insight into the flow of cohesive granular materials will serve as a benchmark for the simulations with the triboelectric effect. It tells us that if interface fluctuations are measured in these next simulations, it is a great indication that the granular material is cohesive and that all the interpretations made at this stage can also apply.

### 5.4 Toy project: the recoater

Work published in:

Nicolas Preud'homme, Aurélien Neuveu, Filip Francqui, Eric Opsomer, Nicolas Vandewalle and Geoffroy Lumay. Simulating powder bed based additive manufacturing processes: from DEM calibration to experimental validation. *ECCOMAS Congress*, 2020.

There is one specific emerging application where powder flowability is a critical parameter, the Selective Laser Melting (SLM) printing process. As briefly discussed in the introduction, this process is a printing technique that consists in spreading a uniform layer of a thin powder which is then locally melted to progressively create an object, layer after layer. To reach a high resolution, the powder used must be as fine as possible. These powders are typically made of fine particles which are highly cohesive [148]. It is thus difficult to spread them uniformly. Assessing the powder's flowability is therefore necessary for SLM and

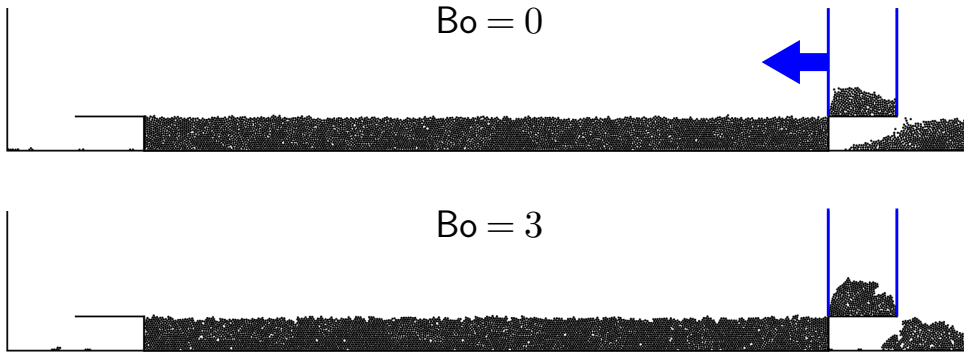


**Figure 48:** Simulation of the additive manufacturing using the recoating process (in blue) with the deposition of a non-cohesive powder (top) and cohesive powder (bottom).

it has been shown that using a rotating drum to analyze the powders is a good method [152,160]. Once the powder has been characterized in the rotating drum, it can also be interesting to optimize the printing parameters such as the speed of spreading or the shape of the recoater (*i.e.* the device used to spread the powder). As testing these parameters in the printer is expensive and time consuming, DEM simulations of the spreading process can be an interesting tool.

The simple model of cohesion I implemented in the previous simulations has been used to reproduce the spreading of fine cohesive powders. The additive manufacturing process has been reproduced in 2D by filling a rectangular container with a length  $L \sim 300$  grain diameters and a height  $h \sim 15$  grain diameters as shown in figure 48. The deposition device, the recoater, consists of 2 vertical walls separated by  $1/10^{th}$  of the container length sweeping the surface of the powder bed at the speed of  $1/4^{th}$  of the container length per second. Once the recoater has passed back and forth over the container, it is filled with grains and the height of the container is incrementally increased by 3 grain diameters after each pass so that a 3-grain-diameter thick layer of grains is deposited onto the underlying powder bed. A representative video showing simulations of the additive manufacturing of an object (in red) can be visualized by scanning the QR code shown in figure 49.

The irregularities of the deposited layer have been quantified by measuring the standard deviation of the grains' position at the interface. The obtained standard



**Figure 49:** Video of the additive manufacturing process simulations with and without cohesion.

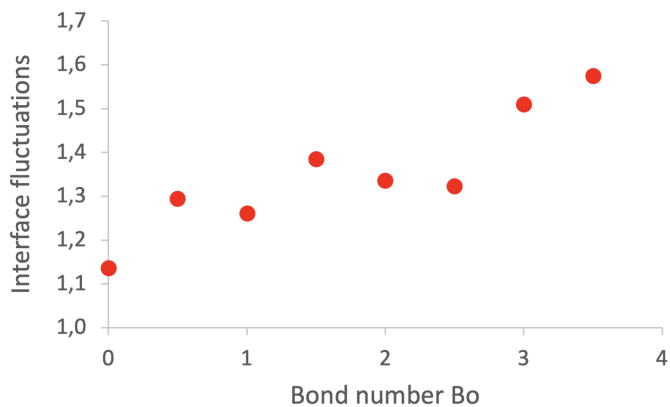


**Figure 50:** Fluctuations of the powder bed's interface after deposition by the recoater.

deviations were then normalized by the grains' radius to obtain the interface fluctuations shown in figure 50. It can be seen that the interface fluctuations increase with  $Bo$  indicating that the interface is more and more irregular.

These simulations could provide a methodology to estimate the quality of a powder for additive manufacturing. Rotating drum simulations can first be used to determine the Bond number. Then, the recoating process can be simulated to obtain the quality of the deposited layer of grains.

---

## 6 The triboelectric effect in granular materials

---

Work published in:

Nicolas Preud'homme, Geoffroy Lumay, Nicolas Vandewalle and Eric Opsomer. Tribocharging of granular materials and influence on their flow. *Soft Matter*, 19(45):8911–8918, 2023.



## 6.1 Motivations

Before analyzing the flow of granular materials charged by the triboelectric effect, the patch model described in section 4.2 is first tested to verify that it correctly reproduces the charging of granular materials. In particular, it should be able to reproduce the saturating charging that has been observed for repeated contacts with identical materials and the influence of the particles' size that have been reported in the state of the art, section 2.1.

To verify that the charge of granular materials made of identical particles effectively saturates, 3D numerical simulations with particles having all the same size and the same density of donors  $p$  have been performed in the rotating drum. As contacts never lead to a net transfer of charge between the particles (as one particle charge  $+$  and the other one charge  $-$  equivalently), the total net charge of the granular material will always be null. We therefore rather measure the transferred charge. Let  $N$  be the number of particles,  $n$  the number of patches per particle and  $q_{ij}$  the charge of patch  $j$  on particle  $i$ , the total transferred charge is given by

$$|Q| = \sum_i^N \sum_j^n |q_{ij}|. \quad (45)$$

Then, simulations with bi-disperse granular materials made of small and large particles have been performed to verify that large particles charge positively while small particles charge negatively. For these simulations, an equal amount of small and large particles have been placed in the rotating drum. The size ratio between the radius of the large particles  $R_L$  and the small particles  $R_S$  is  $R_L/R_S = 2$  and the number of patches is adapted so that their area does not depend on the particles' size. As the particles' surface is multiplied by 4 when the radius is multiplied by 2, 8 patches were placed on the small particles and 32 on the large ones. The amount of charge transferred also does not depend on the particle's size in order to reproduce as precisely as possible identical materials having the same surface properties.

Finally, it has been observed in experiments that non-zero net charging of granular



**Figure 51:** Simulation of the flow of granular materials using the patch model to reproduce the triboelectric effect. In this simulation, 100 identical particles each covered with 8 patches are placed in a rotating drum.

materials could be measured, for example on inclined planes using Faraday cups. The tribocharging of different materials has been investigated with numerical simulations using the patch model. These simulations have been confronted to experiments in a grounded stainless steel cylindrical silo. At the end, all these simulations of the different configurations should allow us to state if the patch model is accurate or not.

## 6.2 Results

### 6.2.1 Mono-disperse granular materials

The charging of 100 identical particles in an insulator rotating drum has first been investigated. The granular flow resulting from the charging of the particles can be seen by scanning the QR code shown in figure 51. In these simulations, the drum has a width equal to  $10/3^{\text{rd}}$  grain diameters, the radius of the drum is equal to 5 grain diameters and the rotation speed is  $2\pi$  rad/s. The charge transferred at one successful contact between two particles is  $q = \pm 4 \cdot 10^{-11}$  C which implies that each patch can charge up to  $q^{\text{max}} = \pm 4 \cdot 10^{-10}$  C. It can be seen in figure 52 that the total transferred charge  $|Q|$  rapidly increases at the beginning of the simulation and then reaches a maximum saturation charge, as in experiments with repeated contacts of identical insulating materials. Interestingly, one can see

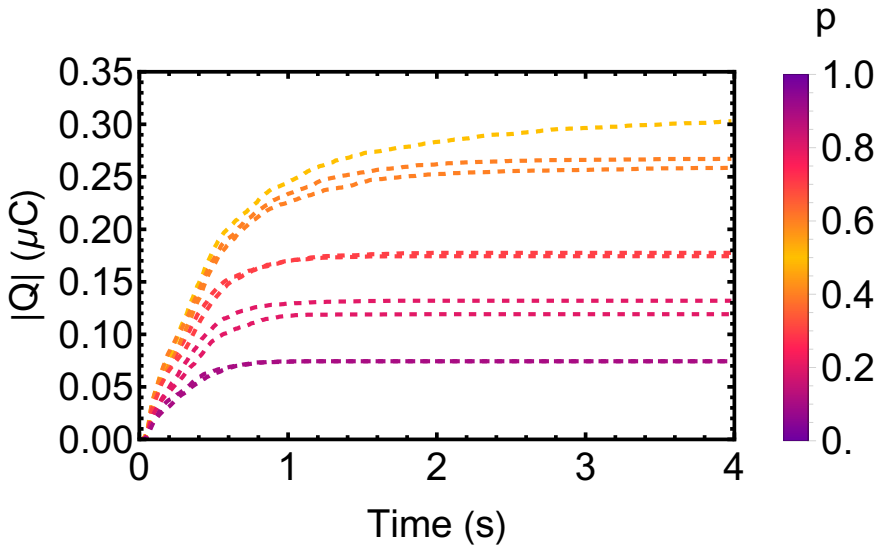


**Figure 52:** Total transferred charge over time of 100 identical particles in the rotating drum. Each curve corresponds to one simulation with a given  $p$  of the particles.

thanks to the simulations that the maximum transferred charge  $|Q|^\infty$  depends on  $p$ . The granular materials charge the most when  $p = 0.5$  and complementary values of  $p$  yield the identical saturation charges (*i.e.*  $|Q|^\infty$  is roughly identical for  $p = 0.1$  and  $p = 0.9$  or  $p = 0.2$  and  $p = 0.8$ ). At the onset of the simulation, many transfers of charges occur because all patches are not charged. This leads to a rapid increase of  $|Q|$  but as all the patches charge by successive contacts between the particles up to  $q_{\max}$ , the transfers of charges slow down.

When  $p = 0.5$ , there are as many donors than acceptors on the particles which implies that all patches could possibly charge when the particles are agitated in the rotating drum. Indeed, all donors could find an acceptor to charge (and inversely) only when  $p = 0.5$ . When  $p \neq 0.5$ , there will be an excess of donors if  $p > 0.5$  or of acceptors if  $p < 0.5$  that cannot be fully charged as there are not sufficient patches of the other species. As the number of donor patches and acceptor patches are respectively given by  $Nnp$  and  $Nn(1-p)$ , one can find the analytical expression

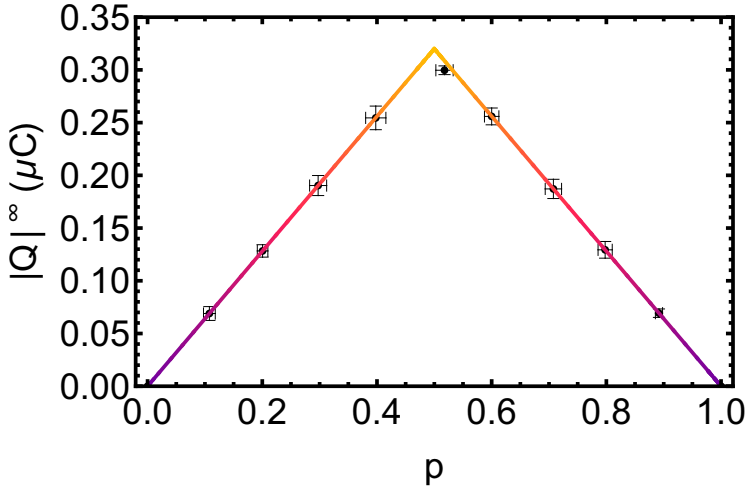


**Figure 53:** Maximum transferred charge of mono-disperse, identical particles agitated in the rotating drum. The results are extracted from the transferred charge measurement presented in figure 52 at 4 s and correctly predicted by the analytical expression (46) (represented in colors, see figure 52 for color legend).

of the granular material's saturation charge

$$|Q|^\infty = q^{\max} Nn \begin{cases} 2p, & p < 0.5 \\ 2(1-p), & p > 0.5 \end{cases}, \quad (46)$$

with the factor 2 coming from the fact that the absolute value of each patch's charge is taken to measure the transferred charge so a transfer of charge between an acceptor and a donor increments  $|Q|$  by  $2|q|$ . As shown in figure 53, this expression precisely predicts the saturation charges obtained from figure 52.

As mentioned previously, if one rather measures the total net charge of the granular materials, one obtains zero. Still, this does not imply that all the particles are not charged. Indeed, as shown in figure 54, some particles have significant net charges. It can also be seen that the particles have the largest charge when  $p = 0.5$  as this distribution is the largest. However, when  $p$  gets closer to 0 or 1, most particles have a net zero charge. It can still be explained by the availability of patches of both species for charging. When  $p = 0.9$ , as there is a large asymmetry in the quantities of donor and acceptor patches, only a few patches can charge resulting

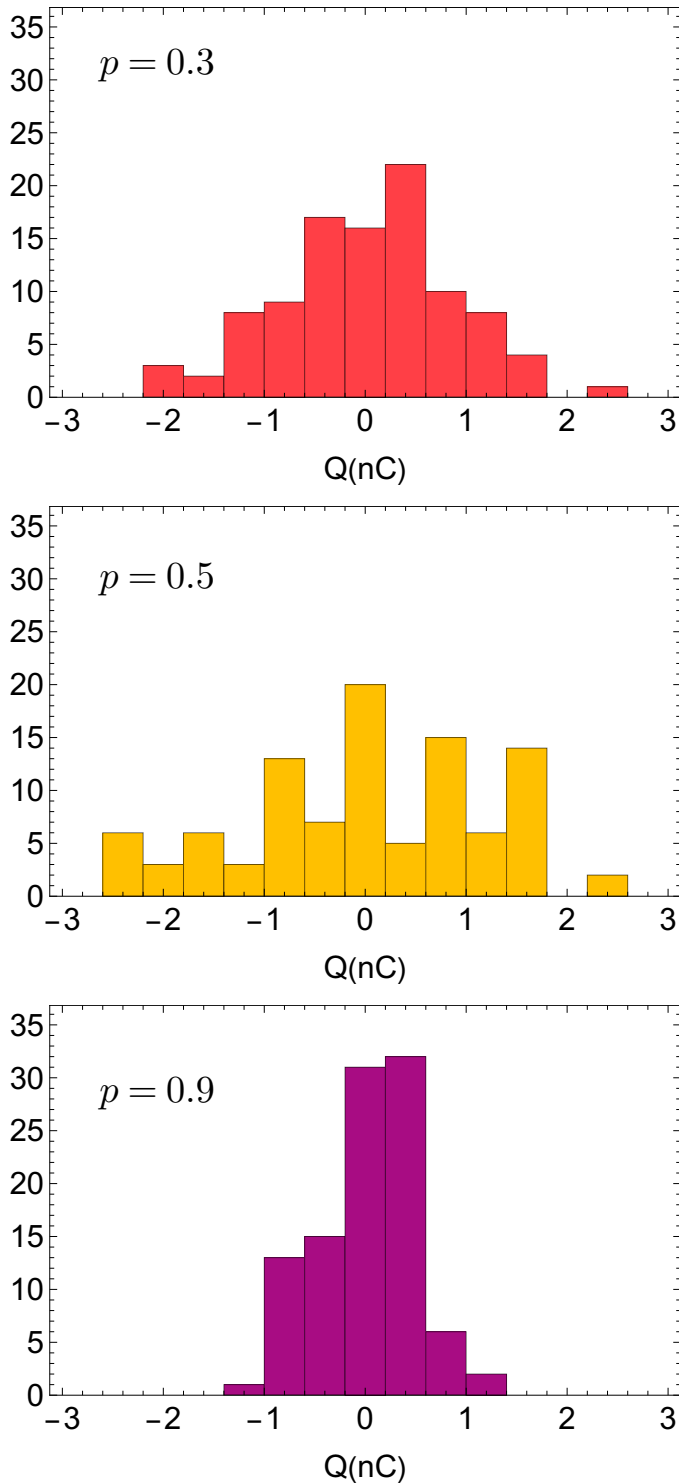


**Figure 54:** Histogram of the particles' charge of mono-disperse granular materials for three different donor densities  $p = 0.3$  (top),  $p = 0.5$  (center) and  $p = 0.9$  (bottom). 109

in weakly charged particles in average. However, when  $p = 0.5$ , as there are as many donor than acceptor patches, all patches could possibly charge. It can be seen in figure 54 for  $p = 0.5$  that some particles have a net charge close to  $\pm 3$  nC which is only possible if most of the particles' patches were charged positively (*i.e.* donors) or negatively (*i.e.* acceptors). Indeed, as the patches can charge up to  $q^{\max} = \pm 4.10^{-10}$  C and as there are 8 patches per particle, the maximum charge a particle could have is  $\pm 3.2$  nC. The fact that particles charge close to this value even though  $p = 0.5$  comes from the statistical definition of the patches using the patch donor probability  $p$ . Particles are covered in average at 50% with donor patches and 50% with acceptor patches when  $p = 0.5$  but some of them might have much more donors than acceptors or inversely.

### 6.2.2 Bi-disperse granular materials

The total net charge of all the small and all the large particles in a binary mixture has been measured as follows

$$Q = \sum_{i=1}^N \sum_{j=1}^n q_{ij}. \quad (47)$$

It can be seen in figure 55 that the saturation charge of the particles again strongly depend on  $p$ . When  $p = 0.3$ , large particles charge positively while small particles charge negatively but when  $p = 0.7$ , the opposite is measured. When  $p = 0.5$ , no significant charging of the particles is measured or large particles charge positively in one simulation and negatively in the following one so that the average charge of the particles is null. It can also be seen in figure 55, especially for  $p = 0.3$  and  $p = 0.7$ , that the charge of the particles remains close to zero for a brief moment at the beginning of the simulations. In other simulations not shown here, transient opposite charging of the particles has even been observed (*e.g.* small particles initially charging positively and large charging negatively when  $p = 0.3$ ). This observation has also been reported in experiments on asymmetric rubbing that have been discussed in section 2.1.3.

At the onset of the simulations, the probability of having contacts between donor patches on small particles and acceptors on large particles is equal to the probability of having a contact between acceptors on small particles and donors

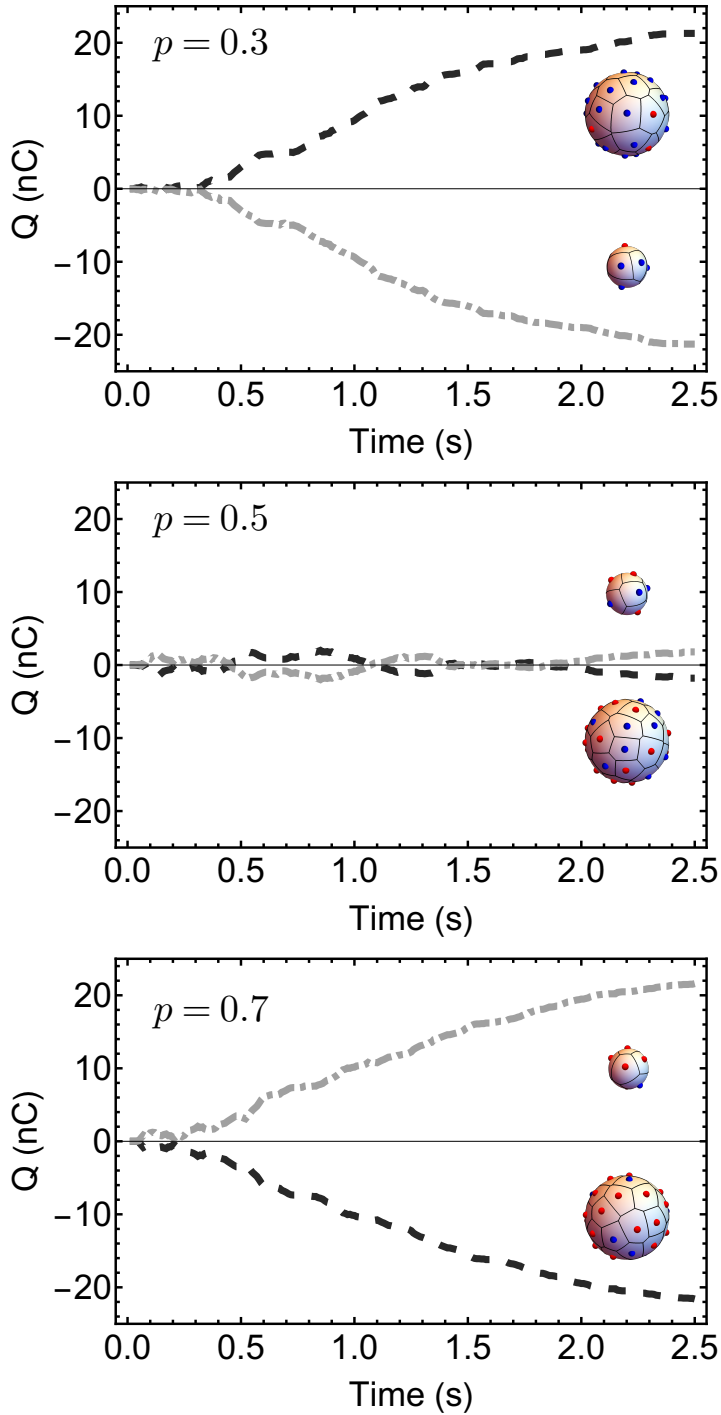


**Figure 55:** Total net charge of large particles (dark dashed) and small particles (light dot dashed) in bi-disperse granular mixtures for  $p = 0.3$  (top),  $p = 0.5$  (center) and  $p = 0.7$  (bottom). Representative particles of the simulations are shown for each curve.

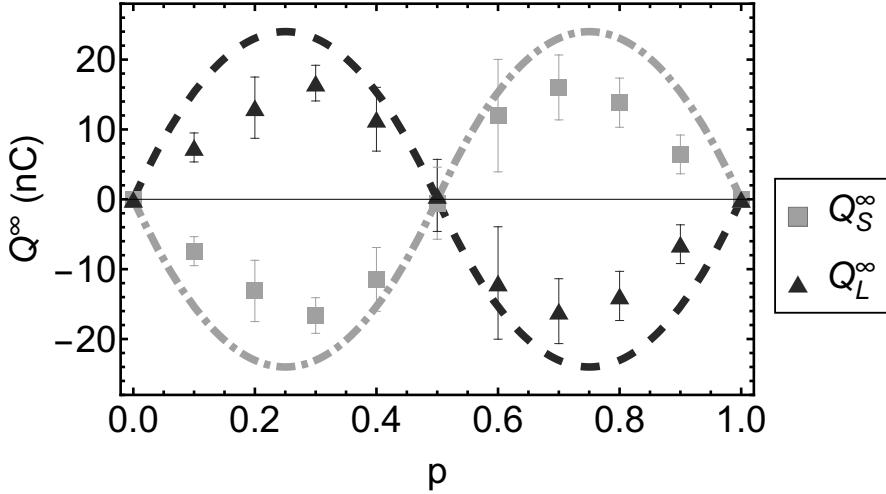


**Figure 56:** Saturation net charge of large (dark squares) and small particles (light triangles) in binary mixtures. Dashed and dot dashed curves for the saturation net charge of large and small particles (respectively dark dashed and light dot dashed curves) are given by equation (66).

on large particles, respectively  $p(1-p)$  and  $(1-p)p$ . As the first kind of contact charges small particles positively and large ones negatively while the second one charges small particles negatively and large ones positively, their net charge remains close to zero for a short time. Once all the patches of the minority species have been charged (donors when  $p < 0.5$  and acceptors when  $p > 0.5$ ), only the patches of the excess species can keep on charging which will eventually determine the particles' final charge.

To highlight more precisely the influence of  $p$  on the charging of bi-disperse granular materials, each simulation has been repeated 10 times with the same set of parameters and the net charges at saturation of all the small  $Q_S^\infty$  and all the large particles  $Q_L^\infty$  have been measured. The results are shown in figure 56. One can see that particles indeed do not charge in average when  $p = 0.5$ . If the density of donors is smaller than 0.5, then large particles charge positively and small particles charge negatively. But if the density of donors is larger than 0.5, then large particles charge negatively and small particles charge positively. An analytical expression can be found by applying a similar reasoning than for the case of mono-disperse granular materials, by looking at the patches in excess and



in minority depending on  $p$ . Let us assume that the simulation is sufficiently long so that all the patches that can charge have the maximum saturation charge  $q^{\max}$ . The charge of the particles is then given by the number of charged patches multiplied by their charge. As charged acceptors have a negative charge and charged donors have a positive charge, the saturation charge of the particles is given by

$$Q^\infty = (n^+ - n^-)q^{\max}, \quad (48)$$

where  $n^+$  is the total number of charged donors and  $n^-$  is the total number of charged acceptors. These number of charged patches depend on  $p$ . Indeed, when  $p < 0.5$ , there are more acceptors than donors in the system. Consequently, all the donors patches have been completely charged after a sufficiently long time but not all the acceptors. Only a number of acceptors equal to the number of donors have been charged. For the small particles, the number of charged acceptors is thus given by

$$n_S^- = N_S n_S p, \quad (49)$$

where  $N_S$  is the number of small particles and  $n_S$  is the number of patches per small particle. There remains an excess of acceptors on both types of particles. The excess number of non-charged acceptors on small particles is then given by

$$N_S n_S (1 - p) - n_S^-, \quad (50)$$

where  $N_S n_S (1 - p)$  is the total number of acceptors. Simplifying yields

$$2N_S n_S (0.5 - p). \quad (51)$$

Considering the larger number of collisions between small and large particles, this excess of acceptors can be charged by large particles' donor patches. However, only a fraction of these acceptor patches in excess can be charged as when  $p = 0$ , there are no donor patches to charge them. But when  $p = 0.5$ , there is a maximum availability of donors on the large particles which implies that all the acceptors in excess on the small particles can be charged. Therefore, expression (51) should be multiplied by  $2p$  to obtain the number of excess acceptors on small particles that

have been charged by large particles' donor patches

$$2N_s n_s (0.5 - p) 2p. \quad (52)$$

The total number of charged acceptors thus becomes

$$n_s^- = N_s n_s p + 2N_s n_s (0.5 - p) 2p. \quad (53)$$

When  $p < 0.5$ , the total number of charged donors on small particles is also given by

$$n_s^+ = N_s n_s p. \quad (54)$$

Concerning the large particles, when  $p < 0.5$ , all of their donor patches are also charged

$$n_L^+ = N_L n_L p. \quad (55)$$

The number of charged acceptors should then also be equal to the number of donors. However, some of the large particles' donor patches – whose number is given by equation (52) – have been charged by the small particles' acceptor patches. Therefore, there remains less donor patches to charge the large particles' acceptor patches which yields

$$n_L^- = N_L n_L p - 2N_s n_s (0.5 - p) 2p. \quad (56)$$

When  $p > 0.5$ , there are more donors than acceptors in the system. All of the acceptor patches have thus been charged but only a number of donors equal to the number of acceptors have been charged

$$n_s^+ = N_s n_s (1 - p). \quad (57)$$

The excess number of non-charged donors on small particles is thus given by

$$N_s n_s p - n_s^+, \quad (58)$$

which is equal to

$$2N_s n_s (p - 0.5). \quad (59)$$

None of these donor patches can be charged when  $p = 1$  as there are no acceptors

on large particles and all of them can be charged when  $p = 0.5$  as there is a maximum availability of acceptor patches on large particles. Therefore, only a fraction of these patches equal to  $2(1-p)$  can be charged which implies that the number of excess donors on small particles that have been charged by large particles' acceptor patches

$$2N_S n_S (p - 0.5) 2(1 - p). \quad (60)$$

The total number of charged donors thus becomes

$$n_S^+ = N_S n_S (1 - p) + 2N_S n_S (p - 0.5) 2(1 - p). \quad (61)$$

And all of the small particles' acceptor patches are charged as  $p > 0.5$

$$n_S^- = N_s n_S (1 - p). \quad (62)$$

Similarly than when  $p < 0.5$ , all of the large particles' acceptor patches are charged.

$$n_L^- = N_L n_L (1 - p). \quad (63)$$

However, some of them have been used to charge the small particles' donor patches. Therefore, there remain less acceptor patches on the large particles to charge all of their donor patches which implies that

$$n_L^+ = N_L n_L (1 - p) - 2N_S n_S (p - 0.5) 2(1 - p). \quad (64)$$

There are thus two regimes, when  $p < 0.5$  and when  $p > 0.5$ . Injecting all of these expressions of  $n^+$  and  $n^-$  in equation (48) yields

$$Q_S^\infty = 2N_S n_S (p - 0.5) q^{\max} \begin{cases} 2p, & p < 0.5 \\ 2(1 - p), & p > 0.5 \end{cases}, \quad (65)$$

and

$$Q_L^\infty = 2N_S n_S (0.5 - p) q^{\max} \begin{cases} 2p, & p < 0.5 \\ 2(1 - p), & p > 0.5 \end{cases} = -Q_S^\infty. \quad (66)$$

It is worth noticing that, to obtain these expressions, some terms are simplified.

They correspond to the patches that have been charged because of contacts between same-sized particles and should thus indeed not contribute to the particles' net charge.

These expressions fit quite well the numerical results as shown in figure 56. The overestimation is explained by the fact that these expressions give the asymptotic total charge of the particles that might not have been reached yet after 2.5 seconds of simulation. Some patches might also not have been fully charged because of the interactions between the particles. If particles stick to each other in the simulations because of electrostatic interactions, the patches in contact cannot charge anymore.

As these expressions fit well the results, it can be deduced from their development that small particles charge negatively when  $p < 0.5$  because they have an excess of acceptor patches that can be charged by the large particles' donor patches who subsequently charge positively. When  $p > 0.5$ , small particles have an excess of donor patches that can be charged by the large particles' acceptor patches. Consequently, small particles charge positively and large particles charge negatively.

### 6.2.3 Different materials tribocharging

Work submitted as:

Nicolas Preud'homme, Eric Opsomer and Geoffroy Lumay. Tribocharging of granular materials in grounded inclined tubes. *Soft Matter*.

In experiments such as the ones described in section 2.2.3 with granular materials flowing on inclined planes, the net charge of granular materials measured in Faraday cups is different from zero. This result cannot be reproduced in the numerical simulations if contact charging only occurs between the particles as charge is conserved during contact. In these experiments using inclined planes and tubes, granular materials are flowing on another surface which might be made of another material. The net charging of granular materials could thus arise from different materials tribocharging.

To test this hypothesis, patches have been placed on the rotating drum and different values of  $p$  were used for the particles and for the drum in order to reproduce different materials. Charging in long inclined tubes has also been investigated. Insulator and metallic containers have been simulated by charging or not the container. When the container is an insulator, its patches charge and keep their charge after contact. Electrostatic interactions then occur between charged particles and charged patches on the container. To reproduce in the simulations a metallic and grounded container, its patches do not remain charged after contact. Interactions between the container and the charged particles still occur and can be implemented using the method of image charges. When a point charge is placed near a grounded or conducting surface, the surface induces charge redistribution to maintain electrostatic equilibrium. This redistribution creates an image charge that, when combined with the original charge, produces the correct boundary conditions at the surface. For example, consider a point charge  $q$  located near a grounded conducting plane. The method of image charges introduces a fictitious charge  $q'$  symmetrically positioned with respect to the plane, such that the potential at the plane is constant and equal to zero. The total potential produced by the real and image charges satisfies the boundary conditions of the grounded plane. This method then allows to calculate the force on the real charge using Coulomb's law between the two point charges. As the particles in the simulations are covered with patches, the mirror particles have oppositely charged patches at the same locations as shown in figure 57.

Let's consider a patch  $P$  at position  $(x_P, y_P, z_P)$  on a grain close to the tube as shown in figure 57. The distance between this patch and its mirror charge at the opposite side of the tube is given by

$$d = 2 \frac{|ay_p + bz_P + c|}{\sqrt{a^2 + b^2}} \quad (67)$$

where  $a$  and  $b$  are the components of the normal vector  $\mathbf{n}$  of the line that is tangential to the drum which is represented in green in figure 57 (this normal vector is the same as the unitary normal vector of contact which was shown for normal contacts in figure 31) and  $-c = ay_M + bz_M$  as  $M(x_M, y_M, z_M)$  is a point of the line.

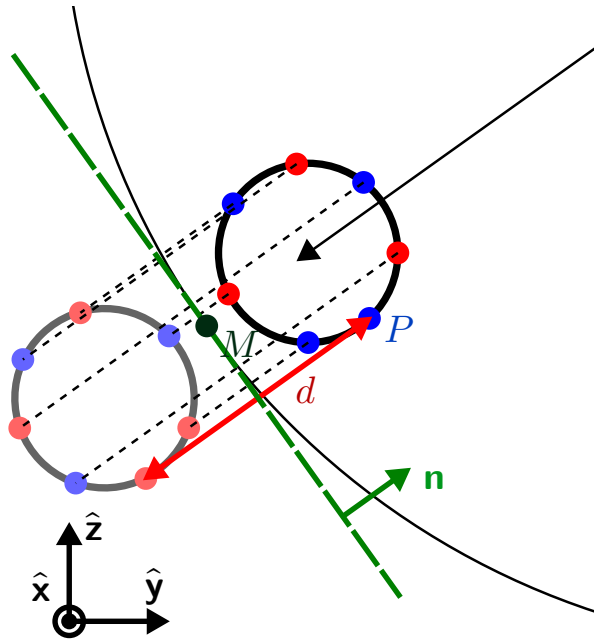


**Figure 57:** Method of mirror charges to calculate the force exerted on a particle that is close to the conducting and grounded tube. The distances between the tube and the patches are determined using the green dashed line to project the patches to the other side of the tube. The mirror particle's patches have the opposite charge. A positively charged donor patch on the real particle (in red) becomes a negatively charged acceptor patch on the mirror particle (in blue).

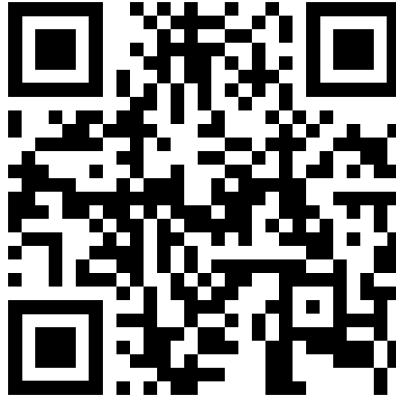


**Figure 58:** Simulations with patches on an insulator drum to reproduce different materials tribocharging. Different densities of donors have been used for the patches of the particles  $p$  and those of the drum  $p_D$ .

Simulations with patches on the drum can be visualized using the QR code shown in figure 58. In one of the two simulations shown in this video,  $p = 0$  and  $p_D = 1$  has been used so that transfers of charges only occur between the particles and the drum. The particles are thus all negative while the drum's patches are all positive. It can be seen that some particles stick to the drum because of attraction between the oppositely charged patches of the particles and the drum enhanced by the repulsion between the negatively charged particles' patches.

The net charge of granular materials has been measured for different values of  $p$  and  $p_D$  and is shown in figure 59. It can be observed that the granular material has a negative net charge if  $p < p_D$  and a positive charge if  $p > p_D$ . Indeed, when  $p < p_D$ , the drum has a larger density of donors than the particles. Most of the particles' acceptor patches will then charge with the drum's donor patches and this leads to the granular material charging negatively. Inversely, when  $p > p_D$ , the drum has a higher density of acceptors than the particles. Most of the particles' donor patches will then charge with the drum's acceptor patches resulting in a positively charged granular material.

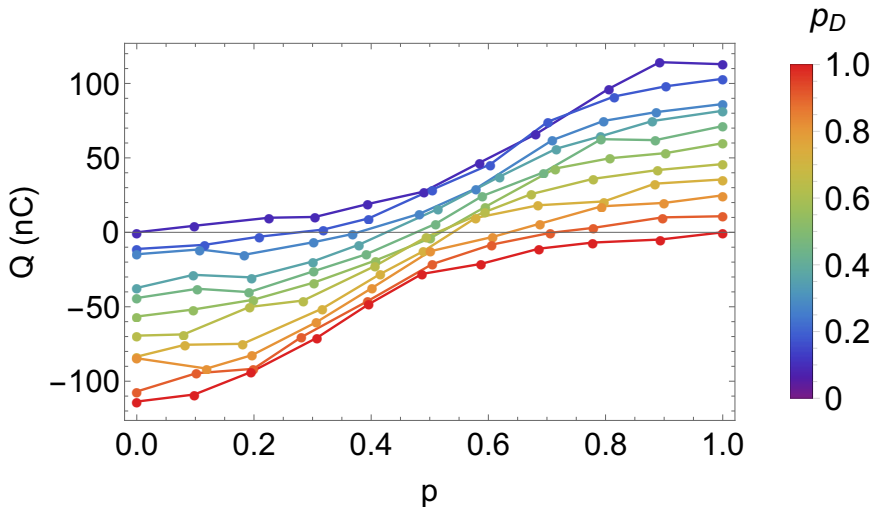


**Figure 59:** Net charge of mono-disperse granular materials flowing in a rotating drum that is also covered with donor and acceptor patches and can thus also exchange charges at contact with particles. The density of donors on the particles is given by  $p$  and on the drum by  $p_D$ .

To investigate the influence of the angle of an inclined plane on the charge of granular materials, simulations with a longer inclined drum and a rotation speed equal to zero have been performed. 150 particles have been dropped at the highest end of the tube and the net charge is measured once all the particles are at rest on the lower end wall or stuck to the tube. In addition, these simulations have been confronted to experiments. The experimental setup that was used is shown in figure 60. It consists in a grounded tube inside which glass beads are poured from a silo. As the powder flows inside the tube, the grains acquire electric charges through friction that occurs both between the grains themselves and between the grains and the tube wall. The powder exiting the tube is collected in a Faraday cup connected to an electrometer, which measures both the total quantity of charge  $Q$  present in the sample and the charge's polarity.

Concerning the numerical simulations, it can be seen in figure 61 that the net charge of granular materials first increases (in magnitude) with the tilt angle up to a critical angle  $\alpha^*$  and then decreases with  $\alpha$ . It is observed in the simulations that below  $\alpha^*$ , particles stick to the drum because electrostatic interaction between



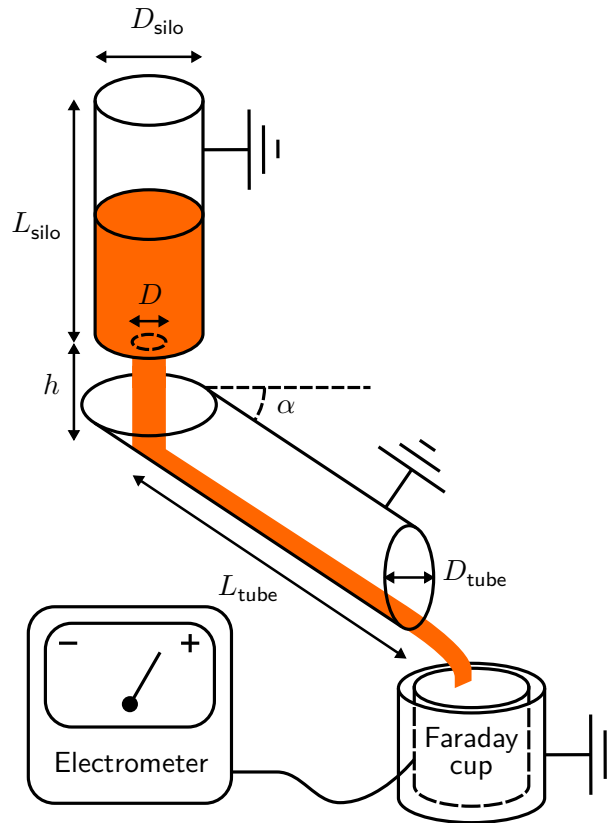


**Figure 60:** Experimental setup to measure the charge of granular materials flowing in an inclined tube. A granular material is poured in a tube inclined of an angle  $\alpha$  and falls in a Faraday cup to measure its net charge.

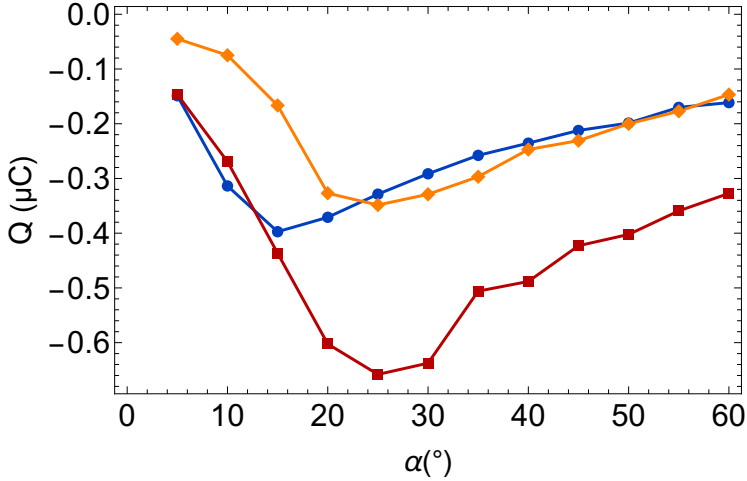


**Figure 61:** Net charge of granular materials flowing in an inclined tube with  $\alpha$  the angle of the tube (numerical simulations). For these simulations,  $p = 0$  and  $p_D = 1$  to maximize the transfers of charges between the particles and the drum. Simulations have been performed with parameters of reference of the rolling friction coefficient  $\mu_{r,0}$  and the maximum charge per patch  $q_0^{\max}$  ( $\bullet$ ), with a higher maximum charge per patch  $q^{\max} = 2q_0^{\max}$  ( $\blacksquare$ ) and with a higher rolling friction coefficient  $\mu_r = 20\mu_{r,0}$  ( $\blacklozenge$ ). All the grains have been considered to measure  $Q$ .

the particles and the drum is sufficient to overcome gravity. Consequently, as the particles cease rolling on the tube, fewer contacts occur between the particles and the drum, resulting in minimal charging of the granular material. This behavior is even more important with an increase in either the rolling friction coefficient of the grains,  $\mu_r$ , or the maximum charge per patch,  $q^{\max}$ . When  $\mu_r$  is increased,  $\alpha^*$  increases, because more grains adhere to the tube at low angles. Similarly, when  $q^{\max}$  increases, the interactions with the tube also increases leading to enhanced adherence of the grains on the tube. When  $\alpha$  is larger than  $\alpha^*$ , the granular materials' net charge decreases in agreement with the experimental results presented in section 2.2.3. It has been proposed that particles bounce off the tube to explain this effect. This interpretation also works with the patch model as when particles bounce, less contacts occur between the particles and the drum. Particles' patches are thus less charged.

In our experiments using a metallic grounded inclined tube, the charge increases with the angle of the tube as can be seen in figure 62 which is contrary to the

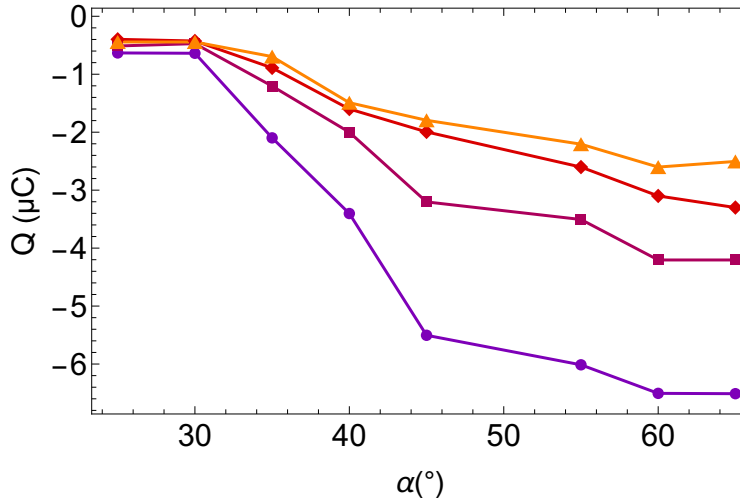


**Figure 62:** Charge of glass beads flowing in a grounded inclined tube obtained in experiments (tube: aluminum,  $L = 300$  mm) with  $D = 4$  mm (●),  $D = 8$  mm (■),  $D = 12$  mm (◆) and  $D = 18$  mm (▲).

numerical results and previous studies [106, 107, 109]. However, when considering only the grains reaching the bottom of the tube to measure the charge in the numerical simulations, we observe that the granular material's charge actually increases with  $\alpha$ , as shown in figure 63. To obtain this result, only the charge of grains close to the bottom end of the tube is taken into account to measure  $Q$ , grains beyond a distance of  $8R$  from this end cap are disregarded. This suggests that the charge increases with the tube angle because an increasing number of charged grains reach the bottom of the tube in simulations or the Faraday cup in experiments. However, above  $50^\circ$ , the charge still decreases, a phenomenon explained by Ireland's interpretation [110]. At larger angles of the tube, the number of contacts between the grains and the tube decreases, leading to a reduction in grain charge due to fewer charge transfers between the grains and the tube.

If the length of the tube is varied in the experiments, it can be seen in figure 64 that granular materials charge more when the tube is longer. This result has also been obtained in numerical simulations as shown in figure 65 and can be explained in light of the patch model. When the tube is longer, the particles will have the opportunity to get in contact with much more patches from the tube and therefore charge more. It also seems in the experiments that the diameter of

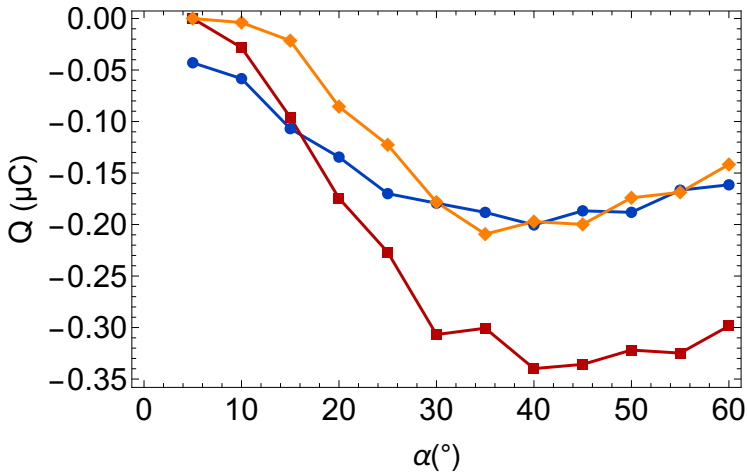


**Figure 63:** Net charge of only the grains that have reached the bottom of an inclined tube with  $\alpha$  the angle of the tube (numerical simulations). For these simulations,  $p = 0$  and  $p_D = 1$  to maximize the transfers of charges between the particles and the drum. Simulations have been performed with parameters of reference of the rolling friction coefficient  $\mu_{r,0}$  and the maximum charge per patch  $q_0^{\max}$  (●), with a higher maximum charge per patch  $q^{\max} = 2q_0^{\max}$  (■) and with a higher rolling friction coefficient  $\mu_r = 20\mu_{r,0}$  (◆).

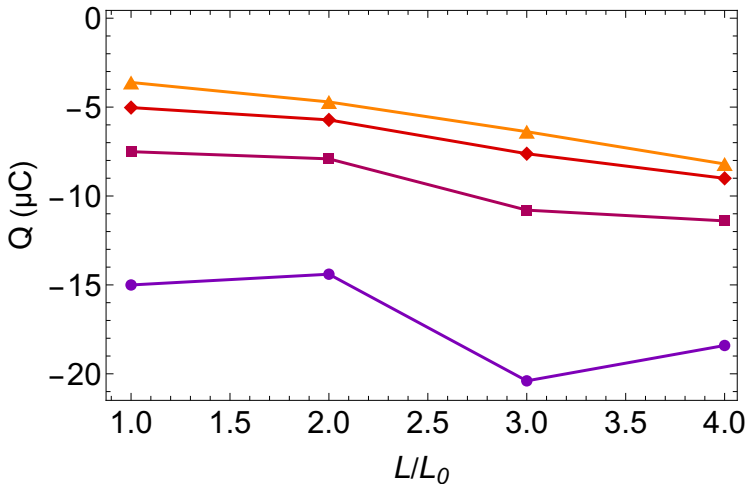


**Figure 64:** Charge of glass beads obtained in experiments by varying the length of the grounded aluminum tube with  $D = 4$  mm (●),  $D = 8$  mm (■),  $D = 12$  mm (◆) and  $D = 18$  mm (▲).

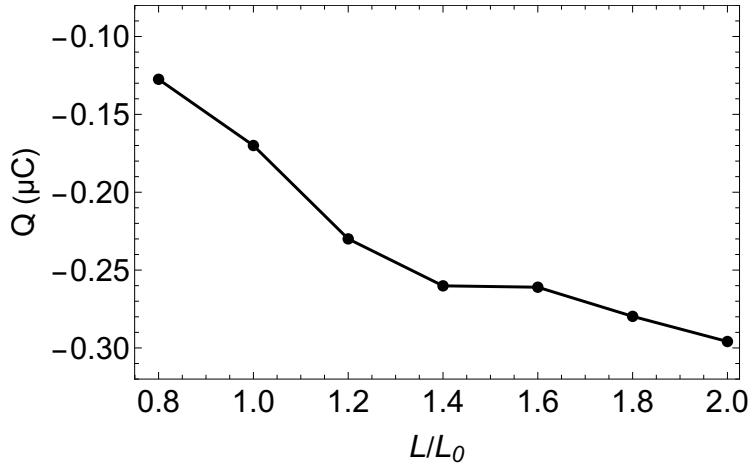


**Figure 65:** Net charge of granular materials flowing in an inclined tube with  $L$  the length of the tube and  $L_0 = 10R_d$  with  $R_d$  the radius of the tube (numerical simulations). The tube is inclined at  $25^\circ$ . Donor densities are  $p = 0$  and  $p_D = 1$ .

the silo output has an influence on charging as can be observed in figures 62 and 64. This effect can be interpreted as follows. A smaller output diameter results in a thinner stream of glass beads flowing through the tube. In this configuration, most beads make contact with the tube, facilitating charge exchange. Conversely, a larger output diameter allows for a thicker layer of beads within the tube, where many beads primarily interact with each other rather than with the tube. These inter-bead contacts do not contribute to the net charge collected in the Faraday cup. Therefore, as the output diameter increases, the number of bead-tube contacts is reduced and the measured charge decreases.

The numerical simulation model employed allows for the investigation of the influence of the quantity of charges exchanged during contact—a parameter that is particularly challenging to control in experiments. Figure 66 illustrates that the charge collected at the bottom of the tube initially increases with  $q_{\max}$ , but remains constant when grains are highly charged. This phenomenon can be explained by considering the adherence of grains to the tube. With an increase in the charge of the grains, their interaction with the tube intensifies. Consequently, although the grains become more charged, the charge of all the collected grains does not increase further due to an increasing number of grains adhering to the tube.

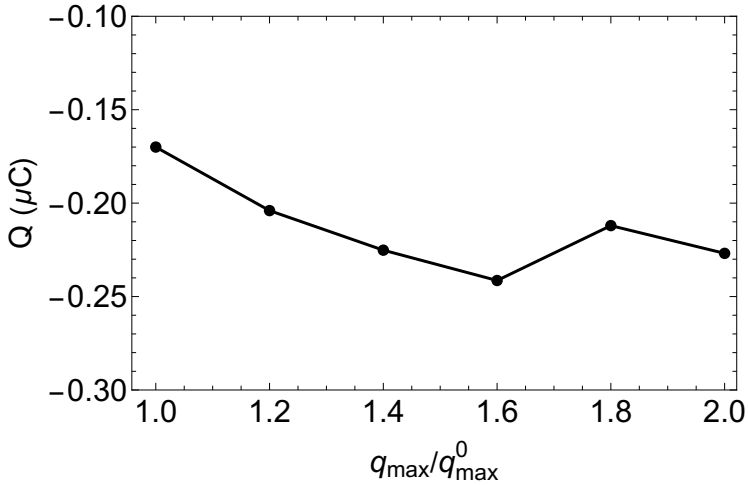


**Figure 66:** Charge of grains that have reached the bottom end of a grounded inclined tube, obtained through numerical simulations by varying the maximum charge of the grains' patches.

### 6.3 Conclusions

The charging of granular materials because of the triboelectric effect has been reproduced in numerical simulations using the patch model. The charging of identical insulators in contact characterized by a rapid increase of their charge during the first contacts followed by a saturation has also been obtained in the numerical simulations with 100 mono-disperse particles. This result was generally explained in other studies by the condenser model that considers the contacts between identical insulating objects like a capacitor. The patch model provides an alternative explanation, based on the density of donors at the surface of the objects. Indeed, it has been shown that the saturation charge of mono-disperse granular materials is determined by  $p$  that defines the maximum number of patches that can possibly exchange charge, thus the maximum charge of the system. Evaluating this number of patches yields analytical expressions that predicts the saturation charge of granular materials.

It has been shown in the state of the art section on the triboelectric effect that the transfer of ions from water patches at the surface of objects is consistent with the patch model and could possibly explain the contact charging of identical

insulators. In this context, the donor patches that exchange a negative amount of charges with acceptors in our numerical simulations could be compared to these water patches that exchange  $\text{OH}^-$  ions with dry patches. Our results then suggest that the saturation charge of identical materials depends on the coverage of the objects' surfaces with water islands. If 50% of the surface is covered with water, then the saturation charge is maximum. If there is a little or a large amount of water on the objects' surface, then charging is less pronounced.

When two types of particles having different sizes are mixed together in the rotating drum, it has been observed in the numerical simulations that the saturation charge of large and small particles depends again on  $p$ . Large particles charge positively while small particles charge negatively only if  $p < 0.5$ . This corresponds to experimental observations as discussed in the state of the art. The numerical simulations also show that the opposite charging of large and small particles could also be possible if the density of donors was larger than 0.5. Once again, the maximum saturation charge of granular materials' large and small particles is determined by the number of patches that can possibly charge. Analytical expressions could be obtained to fit the numerical results and indicate that the charging of bi-disperse granular materials is defined by the species of patches in excess on the small particles. When  $p < 0.5$ , small particles charge negatively (resp. large particles charge positively) because they have an excess of acceptor patches that are charged by large particles' donor patches. When  $p > 0.5$ , small particles charge positively (resp. large particles charge negatively) because they have an excess of donor patches that are charged by large particles' acceptor patches. Compared to the hypothetical ion transfer from wet to dry patches, the numerical results suggest that the specific charging of bi-disperse granular materials observed in nature and in experiments could result from the presence of water patches on less than 50% of the particles' surface.

Granular materials could have a non-zero net charge in the numerical simulations by implementing patches on the container which has its own patch donor probability  $p_D$ . A global net charge of the granular material could be obtained only when  $p \neq p_D$ . It charges positively in average when  $p > p_D$  because there is larger density of donor patches on the particles that get charged by the container's

acceptor patches. It charges negatively when  $p < p_D$  because there is a larger density of acceptor patches on the particles that get charged by the container's donor patches. The fact that non-zero global net charges only appear when different donor densities are used for the particles and for the container can be compared to different materials tribocharging. In particular, regarding the role of water and the transfer of ions from wet to dry patches, the difference in hydrophobicity of the materials would be the critical parameter that controls the global charging of granular materials. For example, a large hydrophobicity would mean that the material's surface is covered with less water which correspond to a low  $p$ . If two materials with different hydrophobicities get in contact, the results obtained with the numerical simulations suggest that the material with the larger hydrophobicity will charge negatively which is indeed what is observed in experiments [48]. These results could thus provide an explanation to the reason why charge seems to fluctuate so much in experiments, sometimes even changing sign. They suggest that small differences in the distribution of patches at the surface of objects could be responsible for an inversion of the polarity.

Finally, the patch model that has been implemented in the simulations also correctly reproduces the charging of granular materials flowing in inclined tubes. It has been observed in experiments that the angle of the tube and its length influences the charge of granular materials. Similar observations have been made in the simulations and explained by the fact that if the angle is larger or if the tube is shorter, the particles undergo less contacts with the drum and thus charge less. The fact that particles could adhere to the tube because of electrostatic interaction also considerably influence their charge.

To sum up the results obtained while investigating the validity of the patch model used for the simulations, I have shown that granular materials obtain a global net charge if (1) there is a polydispersity in the particles' size or if (2) they flow on a different material. All of the experimental observations that have been presented in the state of the art section on the tribocharging of granular materials have been reproduced and explained by looking at the density of donors on the particles.



---

## 7 Influence of electrostatic charges on granular flow

---

Work published in:

Nicolas Preud'homme, Geoffroy Lumay, Nicolas Vandewalle and Eric Opsomer. Tribocharging of granular materials and influence on their flow. *Soft Matter*, 19(45):8911–8918, 2023.

### 7.1 Motivations

The results obtained in the previous section show that the tribocharging of granular materials can be reproduced accurately with the numerical simulations. They even offer a way to control the charging by varying  $p$  which has a physical interpretation as it could be related to the coverage of the grains' surface with water. As discussed in section 2.3.4 *Influence of cohesion*, it has not been possible yet to investigate the flow of cohesive granular materials by varying the intensity of the electrostatic interaction between the particles as the mechanisms of the triboelectric effect are still debated.

Now that the simulations have been validated by comparison to experiments and that the parameters of the patch model are well understood, they can be used to investigate the flow of tribocharged granular materials. It is known thanks to the results I obtained on cohesive granular flows that cohesive granular materials are characterized by an intermittent flow which can be analyzed with the fluctuations of the interface. Moreover, it has been shown that there exists a proportionality between the interface fluctuations and the granular Bond number. In this section, the analysis performed in section 5 on cohesive granular materials is repeated on tribocharged granular materials to finally answer this thesis' central question, **How does the triboelectric effect influence the flow of granular materials?** The answer is not straightforward as some particles repel each other because of electrostatic repulsion. So, is there any cohesion at all in granular materials where particles are covered with positively and negatively charged patches? If so, how do the properties of the patches such as  $p$  or  $q^{\max}$  influence the intensity of cohesion?

To investigate the flow of tribocharged granular materials, numerical simulations with 800 particles have been performed. The radius of these particles have been chosen so that the rotating drum is half filled. Particles are all covered with 8 patches and the rotation speed is set to  $\pi \text{ rad/s} = 30 \text{ rpm}$ . Numerical simulations of granular flows with and without tribocharging can be visualized for comparison using the QR code shown in figure 67. To characterize the flow by measuring the dynamic angle of repose and the fluctuations of the interface, the analysis code described in section 4.3 has been adapted to 3D. Brewster *et al.*'s way of measuring



**Figure 67:** Numerical simulations performed to investigate the flow of tribocharged granular materials in the rotating drum. Two simulations are shown for comparison, one with tribocharging and one without tribocharging.

the dynamic angle of repose with one angle at the top of the flowing layer  $\theta_{\text{top}}$  and at the bottom  $\theta_{\text{bottom}}$  has been used as shown in figure 68. Each simulation is repeated 3 times with the same set of parameters to reduce statistical variations by measuring the mean angle and the mean fluctuations from the 3 simulations.

The parameters investigated are  $p$ ,  $q^{\text{max}}$  and their influence on the flow of tribocharged granular materials is evaluated by measuring the velocity profile and the dynamic angle of repose. Moreover, it is well-known that if granular materials are composed of smaller particles, they are more cohesive as discussed in section 2.3.4. The possibility that it could be due to electrostatic charges is also investigated here by increasing the size of the particles while decreasing the number of particles to keep the drum half filled. The maximum charge per patch and the size of the patches are kept constant to reproduce the flows of granular materials composed of particles that have different sizes but are made of the same materials and have the same surface properties.

## 7.2 Results

By varying the particles' donor density  $p$  between 0 and 1, it can be seen in figure 69(a) that  $\theta_{\text{bottom}}$  is the highest when  $p = 0.5$  while  $\theta_{\text{top}}$  is the lowest. A high

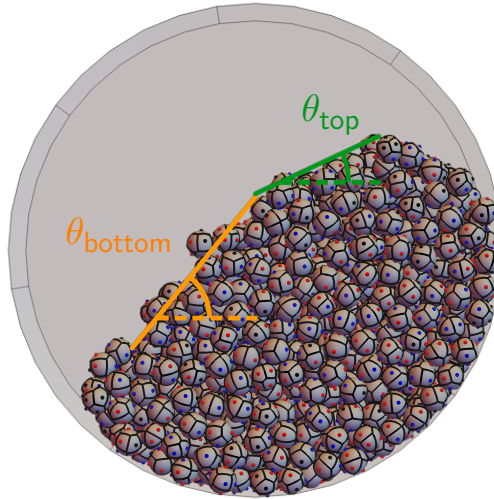


**Figure 68:** Method for measuring the dynamic angles of repose at the top and at the bottom of the flowing layer. These angles are obtained by fitting the interface between  $-R_d/2$  and  $0$  for  $\theta_{\text{bottom}}$  and between  $0$  and  $R_d/2$  for  $\theta_{\text{top}}$ .

$\theta_{\text{bottom}}$  and a low  $\theta_{\text{top}}$  corresponds to a convex interface which is characteristic of cohesive granular materials flows as discussed in section 5. The difference  $\Delta\theta = \theta_{\text{bottom}} - \theta_{\text{top}}$  between the two angles has also been measured and it can be seen that  $\Delta\theta$  is the highest around  $p = 0.5$ . As discussed by Brewster *et al.* [150], the larger  $\Delta\theta$ , the larger the cohesion. The high cohesion of granular materials at  $p = 0.5$  can also be observed in the measurement of the interface fluctuations shown in figure 70(a). The interface fluctuates the most around  $p = 0.5$  which is another indication that granular materials are the most cohesive when  $p = 0.5$ . Compared to the measurement of transferred charge between the particles of mono-disperse granular materials that has been previously discussed and which is shown in figure 53, it can be inferred that cohesion and charge transfer are related as cohesion is high when the transferred charge is high. As the particles' charge is zero on average but display a large distribution when  $p = 0.5$ , attractive electrostatic interaction explains why granular materials are cohesive.

When the maximum charge per patch increases,  $\theta_{\text{bottom}}$  increases while  $\theta_{\text{top}}$

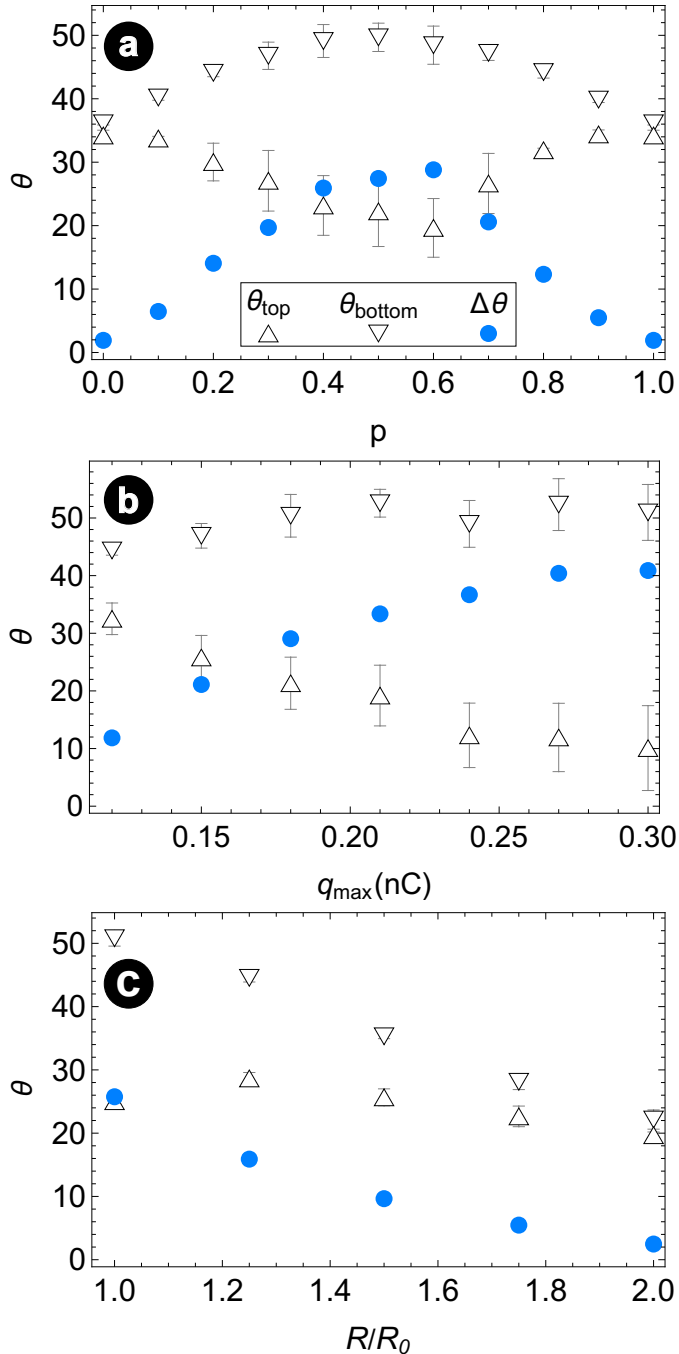


**Figure 69:** The dynamic angles of repose at the top  $\theta_{\text{top}}$ , at the bottom  $\theta_{\text{bottom}}$  of the flowing layer and the difference  $\Delta\theta = \theta_{\text{bottom}} - \theta_{\text{top}}$ . Measurements have been performed in simulations with different donor densities  $p$  (a), different maximum charges per patch  $q^{\text{max}}$  (b) and larger particles (c). Default values are  $p = 0.5$ ,  $q^{\text{max}} = 0.18$  nC and  $R_0$  is the radius of the particles that is used to fill the drum half with 800 particles.

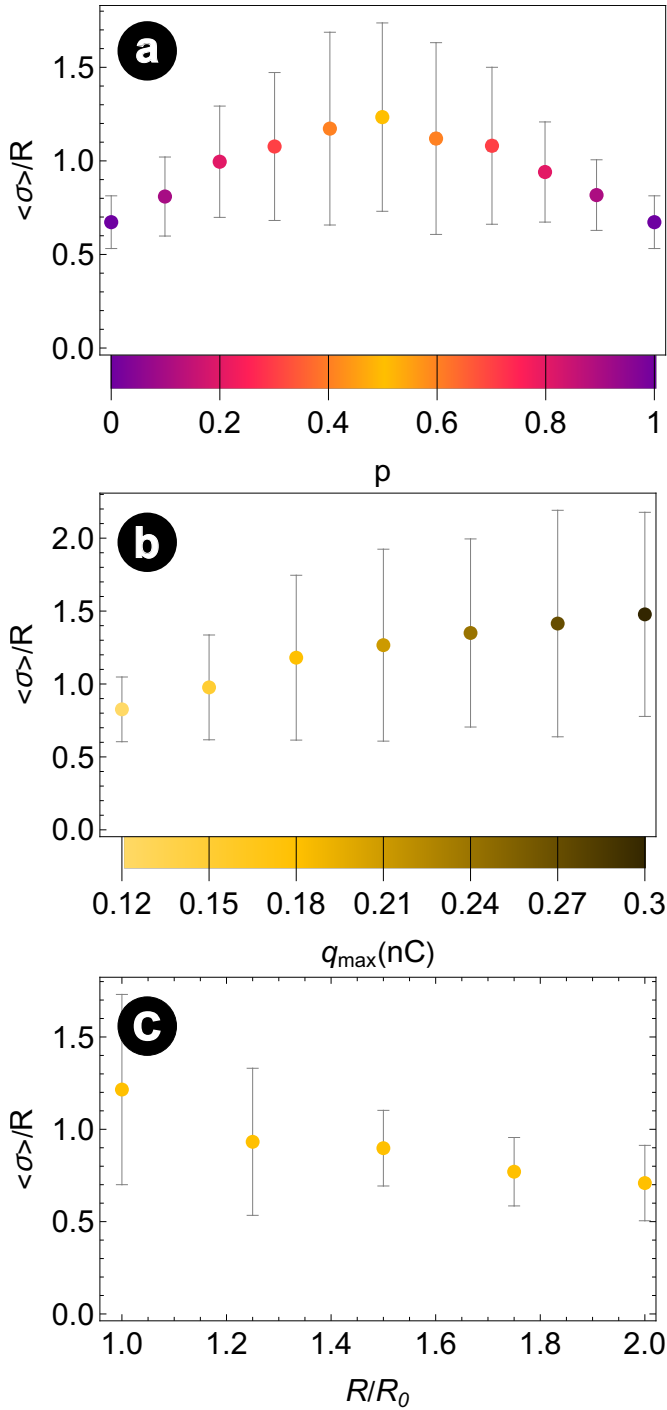


**Figure 70:** The mean fluctuations of the interface obtained in simulations with different donor densities  $p$  (a), different maximum charges per patch  $q^{\max}$  (b) and larger particles (c). Default values are  $p = 0.5$ ,  $q^{\max} = 0.18$  nC and  $R_0$  is the radius of the particles that is used to fill the drum half with 800 particles.

decreases and  $\Delta\theta$  increases as can be seen in figure 69(b). Moreover, the size of the fluctuations increases with  $q^{\max}$  as can be seen in figure 70(b). Granular materials are thus more cohesive if their patches have a higher charge. Granular materials' cohesion increases with the patches' charge because when  $q^{\max}$  is larger, the interactions between the particles are becoming more and more important which leads to larger cohesion. Even though repulsion between patches that have equal signs also increases when  $q^{\max}$  increases, as particles are locally charged, attractive forces seem to prevail and cohesion increases.

The size of the particles has finally been increased to verify whether the flow of tribocharged granular materials was influenced by the size of the particles. As discussed in section 2.3.4, cohesion should increase when particles are smaller. It can be seen in figure 69(c) that when the particles are larger,  $\theta_{\text{top}}$  and  $\theta_{\text{bottom}}$  both decrease but  $\theta_{\text{bottom}}$  decreases faster so that both angles almost have the same values when the particles are two times larger than original. Consequently,  $\Delta\theta$  also decreases and reaches almost 0 for  $R = 2R_0$ . The interface is convex for small particles which is a characteristic feature of cohesive granular materials while it is almost flat for large particles. Even though large particles are still equally charged and even covered with more patches, cohesion is smaller. The same observation can be made by measuring the interface fluctuations shown in figure 70(c). When  $R$  increases, the fluctuations decrease indicating that cohesion is also lower. It can be interpreted as follows, firstly, when the particles are smaller, the total number of patches of the whole granular material increases. Indeed, imagine you have a large sphere, and you cut it into smaller pieces. Each of these pieces now has its own surface area. When you add up the surface areas of all the smaller pieces, you will find that it is greater than the surface area of the original large sphere. This happens because when you cut the sphere into smaller pieces, you create additional surfaces along the cuts. These extra surfaces add to the overall surface area. The total number of patches increases, and so does the transferred charge when particles are smaller. Secondly, the mass of the particles increases when their radius increases but the electrostatic interactions remain constant as  $q_{\max}$  is kept constant. Even if there are more patches on the particles because their surface increases with  $R$ , it seems that attractive forces are not sufficient to keep constant the intensity of cohesion. The ratio between attractive forces and

weight defines the granular Bond number and it should thus be possible to define a Bond number that captures the influence of  $p$ ,  $q_{\max}$  and  $R$ .

The attractive forces exerted between particles is given by Coulomb's law. Particles attract because of their charged patches that are assumed to have a charge  $q^{\max}$ . The mean distance between them,  $r_c$ , has been chosen equal to the cut-off distance of the electrostatic interaction. Therefore an appropriate Bond number for charged particles would be

$$\text{Bo} = \frac{k_e q_{\max}^2}{r_c^2 m g}, \quad (68)$$

where  $m = \rho 4/3\pi R^3$  is the mass of the particles. It has been observed in the simulations that cohesion was the largest when  $p = 0.5$  and nonexistent when  $p = 0$  or  $p = 1$ . The Bond number should include this influence of  $p$ . The previous expression becomes

$$\text{Bo} = \frac{k_e q_{\max}^2}{r_c^2 m g} f(p), \quad (69)$$

where

$$f(p) = \begin{cases} p, & p < 0.5 \\ 1-p, & p > 0.5 \end{cases} \quad (70)$$

expresses the probability that attractive forces exist between charged particles. When  $p = 0$  or  $p = 1$ , no patches are charged so Bo is equal to 0. When  $p < 0.5$ , there is a probability  $p$  that a given patch is in proximity with a charged donor or acceptor and  $1 - p$  when  $p > 0.5$ . If the mean interface fluctuations are expressed as a function of Bo rather than  $p$ ,  $q_{\max}$  or  $R$ , one can see in figure 71 that the data collapses.

### 7.3 Conclusions

It was known from the first study of this thesis on the flow of cohesive granular materials presented in section 5 that measuring the dynamic angle of repose and the fluctuations of the interface can be used to gauge the cohesiveness of granular materials. These measurements have been performed to characterize the flow of tribocharged granular materials and despite the fact that particles repel through their equally charged patches, cohesion has still been observed.



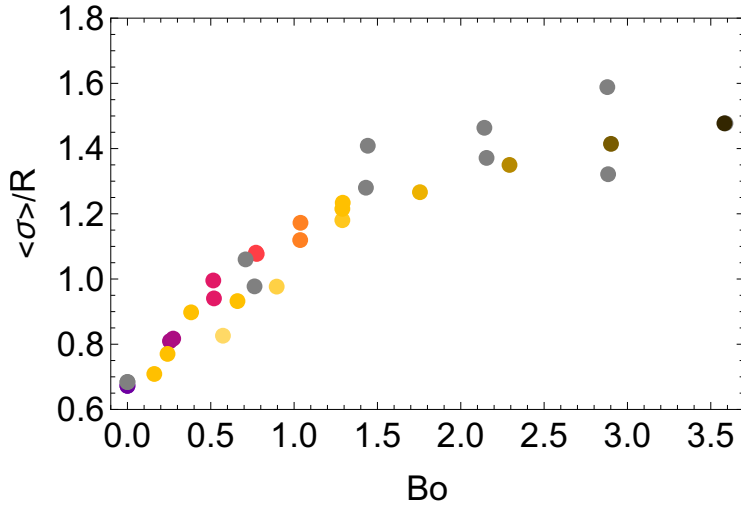


**Figure 71:** Mean interface fluctuations presented in figure 70 rescaled using the granular Bond number defined in equation (69) (see colors for corresponding data). The data has been completed with results obtained with other simulations varying  $p$  while keeping a higher charge per patch constant  $q_{\max} = 0.3$  nC which are represented in gray.

Using the patch model to implement the triboelectric effect in the simulations, it has been observed that cohesion is maximum when the transfer of charges between particles is maximum. It occurs when  $p = 0.5$  which corresponds to a situation where there are as many donor patches than acceptor patches on the particles. If water patches were responsible for the transfers of charges, it would imply that the cohesion which is due to electrostatic interactions could be controlled by humidity. Indeed, as humidity determines the quantity of water adsorbed at the surface of objects, it could be possible to control  $p$  and so the intensity of cohesion by varying humidity.

The cohesion of charged granular materials is also influenced by the amount of charges transferred at contact. It has been observed that cohesion is larger if a larger amount of charges is transferred between the patches at contact. As attractive forces are determined by the charge of the patches, if patches are highly charged, interactions between particles should indeed be stronger.

The last parameter that influences the flow of tribocharged granular materials is

the size of the particles. Similarly than in experiments, it has been observed in the simulations that cohesion is larger if the particles are small. This is caused by the increase of the amount of charge transferred which results from the increase of the total surface area. The fact that the mass of the particles is also smaller when the particles are smaller also explains why cohesion is larger.

The granular Bond number has been determined for tribocharged granular materials. As shown in section 5, it offers a way to interpret the influence of all these parameters on cohesion as a scaling between the mean interface fluctuations and  $Bo$  also exist for tribocharged granular materials.

---

## 8 Influence of grain shape on granular flow

---

Work published in:

Nicolas Preud'homme, Eric Opsomer, Nicolas Vandewalle and Geoffroy Lumay. Effect of grain shape on the dynamics of granular materials in 2D rotating drums. *EPJ Web of Conferences*, 249:06002, 2021.

A presentation video prepared for the Powders and Grains 2021 virtual conference is available at <https://doi.org/10.48448/md56-jy83>.

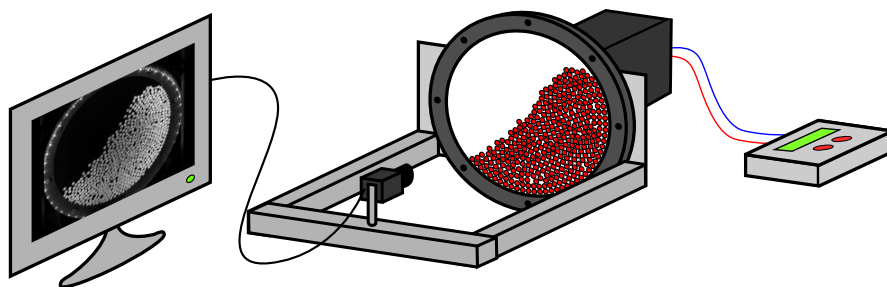


**Figure 72:** Experimental setup to investigate the influence of grain shape on granular flow. All pieces (grains included) are made of 3 mm thick Plexiglas that has been cut using a laser cutter. The 2D rotating drum is filled with one layer of grains and is rotated using a stepper motor. The flow is captured using a monochromatic Thorlabs camera.

### 8.1 Motivations

The grains that compose most of granular materials found in different applications are usually not spherical. As the particles in the numerical simulations are spherical, and the algorithm is based on spherical elements, one must use specific techniques to modify their shape and investigate the dynamics of non-spherical particles in numerical simulations. Several spheres can be stuck together at arbitrary positions to obtain elongated, asymmetric or nonconvex particles [161]. For example, nonconvex particles have been obtained by creating agglomerates of spheres that overlap [162]. The shape of the particles could be controlled by increasing the distance between the central sphere and the overlapping ones. The packing of such particles has been studied in numerical simulations.

As the shape of the particles has not been taken into account in the simulations but it still slightly influences the granular flow in the rotating drum [163–165], I conducted a little experimental investigation on the influence of grain shape on granular flow. The objective is to study how the irregularity of the particles influences the flow of granular materials.

### 8.2 Experimental setup

The setup is represented in figure 72, a 2D rotating drum made of 3 mm thick Plexiglas sheets has been designed by fixing a 20 cm inner diameter annular ring to

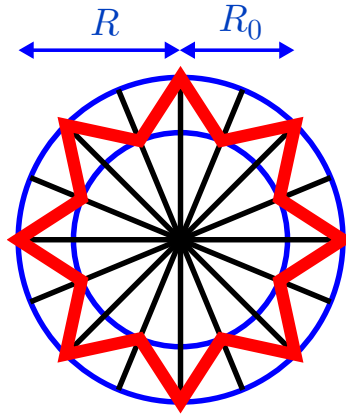


**Figure 73:** The grains used are stars with 8 spikes (in red) whose length is defined using 2 concentric circles (in blue). The ratio  $R/R_0$  allows to control the shape of the grains.

**Table 5:** Parameters of the 2D grains employed for the study of the shape effect on the granular dynamics and their parameters.

	$2R$ (mm)	$\frac{R}{R_0}$	$\mathcal{C}$
●	5.3	1	1.00
⬠	6	6/5	0.89
⬠	6.65	3/2	0.68
⬠	7.75	2	0.46

a circular black back plate. The cell is then closed by a transparent front plate and bolted to a stepper motor to control the rotation speed of the drum. The grains are 8 pointed stars whose irregularity can be controlled by defining 2 concentric circles with radii  $R_0$  and  $R$  for the inner and the outer circles respectively as shown in figure 73. Grains with different circularity  $\mathcal{C}$  could be created by varying  $\frac{R}{R_0}$  while keeping their surface constant. The circularity is defined as the ratio between the perimeter of a circle with an equivalent surface area than the grain and the real perimeter of the grain. The parameters of the grains used for this study are shown in table 5. One single layer of grains is inserted between the two plates of the drum to fill it at half.

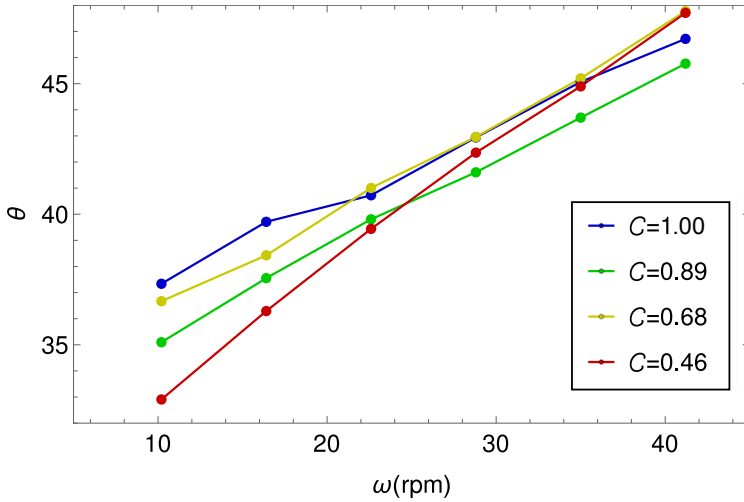


**Figure 74:** The dynamic angles of repose obtained in the 2D experimental rotating drum with different granular shapes (see the shapes corresponding to the different circularity in table 5).

The granular flow is analyzed using a Thorlabs camera. With image analysis, the grain-air interface could be extracted to measure the dynamic angle of repose.

### 8.3 Results

The dynamic angle of repose obtained for all types of grains while varying the rotation speed of the drum is shown in figure 74. At slow rotation speeds, circular particles exhibit a greater dynamic angle of repose compared to highly irregular particles. However, as the rotation speed increases, this trend reverses, with irregular grains displaying the highest angle. This is in agreement with findings from previous experimental and numerical studies on grain shape effects [161,166]. Yet, it is unexpected as irregular grains were anticipated to show a higher angle at lower speeds, as they could form a stronger packing due to interlocking. Conversely, at higher speeds, one would expect a more brittle packing with irregular grains, resulting in a lower angle. Surprisingly, the opposite occurs, possibly explained by dilatancy measurements.

As previously discussed in section 2.2, dilatancy is defined as the ratio of the surface area of a moving granular packing  $S$  to its surface area at rest  $S_0$ . It

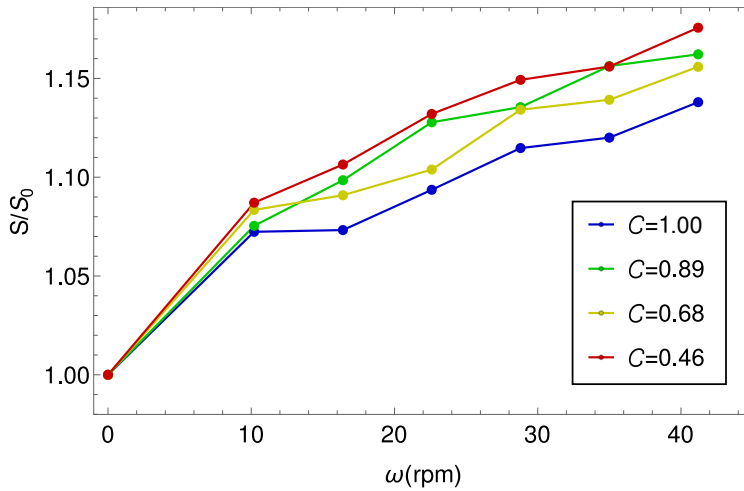


**Figure 75:** Dilatancy of the granular bed in the roasting drum depending on the circularity of the grains  $C$  and the rotation speed of the drum.

can be seen in figure 75 that dilatancy increases for all grain shapes with rotation speed. However, the rate at which dilatancy increases varies with grain shape, with irregular particles exhibiting a faster expansion rate.

Irregular grains thus demonstrate greater dilatancy and a higher dynamic angle of repose at high rotation speeds. This may be attributed to dilatancy acting as a momentum damper. As the granular packing expands, the grains in the flowing layer are more easily trapped in the upward stream of grains. Conversely, when grains are circular, they have a lower dilatancy. The granular bed is denser which allows the grains to flow more easily on the solid bed that lies below, resulting in a smaller angle of repose.

The difference of dilatancy between irregular and circular particles is pronounced at high rotation speeds only, suggesting that another effect is behind the difference of  $\theta$  at low rotation speeds. This could be explained by the packing fraction at rest  $\phi_0$  of the different shapes. It can be seen in figure 76 that circular grains exhibit a higher packing fraction than irregular grains. Consequently, at low rotation speed, circular grains reach the highest angle of repose due to their denser packing fraction. This observation is consistent with findings by Olson et al [167].

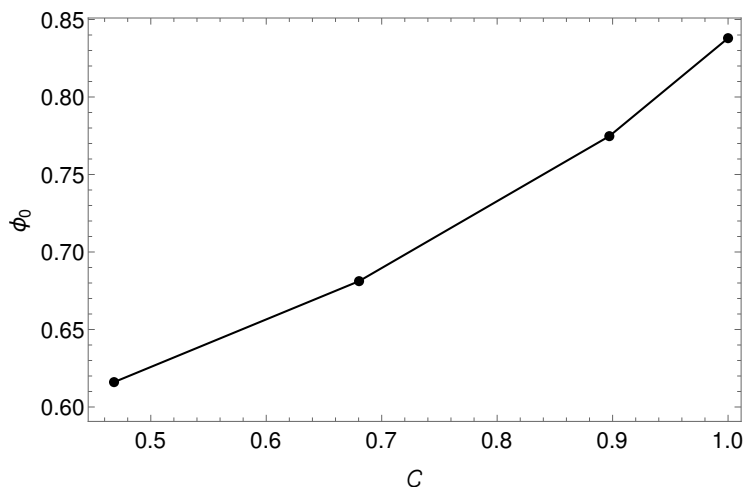


**Figure 76:** Packing fraction at rest in the rotating for each type of particles used for this study.

## 8.4 Conclusions

The influence of the particles' shape on granular flow has been investigated experimentally in a 2D rotating drum made of Plexiglas sheets. The circularity of the grains has been varied to investigate the flow of granular materials made of non circular grains. Two regimes have been observed. At high rotation speed, granular materials dilate more if they are made of non circular particles. This higher dilatancy creates many voids in the granular bed in which the grains of the flowing layer can be trapped. Consequently, the dynamic angle of repose of irregular particles is high at large rotation speeds.

At low rotation speed, the dynamic angle of repose decreases when the grains are not circular because they have a lower packing fraction. The granular bed is thus less stable and flows at a lower dynamic angle of repose when the grains are irregular.



---

## 9 Conclusions and perspectives

---

Granular materials are found in diverse sectors and exhibit intricate behaviors in many applications. Still, our understanding of their full complexity remains incomplete. The granular materials' phase have been investigated in depth using ideal systems to unveil captivating phenomena propelled by inter-particle friction. Notable examples include the Janssen effect, Reynolds dilatancy, force chains, compaction, and the Brazil nut effect, all manifesting in the solid phase. Drawing parallels to the kinetic theory of gases, researchers have adapted it to granular gases, shedding light on clustering phenomena that is observed in strongly agitated granular materials. Moreover, the rheology of granular materials in the liquid phase has been meticulously developed, and various geometries in which granular liquids can be obtained have been characterized precisely.

All of these results as well as the models developed to interpret them are significantly disturbed if more realistic cohesive granular materials are considered instead of ideal systems. In particular, I have shown that the flow of cohesive granular materials that can be obtained in the rotating drum geometry is characterized by an avalanching flow regime that does not exist at all in ideal granular materials. When particles interact through cohesive forces, aggregates are formed in the flowing layer which initiates avalanches periodically and creates large fluctuations at the interface. I have additionally shown that measuring these

fluctuations of the interface is an interesting technique to characterize the flow with respect to the cohesiveness of the powder as the two parameters are directly related.

In this first part of my thesis dedicated to the analysis of cohesive granular material's flow, the mechanisms at the origin of cohesion were not the priority. The attraction between the particles that has been implemented in the Discrete Element Method numerical simulations specifically developed for my thesis consists in a simple attractive force whose intensity and range has been controlled without direct correspondence to real-world phenomena as what causes cohesion in granular materials is still under debate. However, attraction because of the presence of electrostatic charges in granular materials is often mentioned. The reason why the relation between cohesion and charge has not been verified yet is due to the fact that the triboelectric effect, this thousand-year old phenomena responsible of the apparition of electrostatic charges on rubbed objects, is also not fully understood yet. Many fundamental phenomena such as the charging of identical materials remain unclear. Additionally, the consistent acquisition of a positive charge by large particles, the negative charging of small particles, and the consistent negative charging of stretched objects remain puzzling observations.

Still, several models have been proposed to explain the triboelectric effect. Among these, the patch model that considers the existence of charge donor and acceptor patches at the surface of objects seems very promising. I have implemented the patch model in the numerical simulations in place of the simple model of cohesion. Many experimental observations could be retrieved in the numerical simulations and I observed that the density of donor patches is a critical parameter that determines the charge of granular materials. In mono-disperse granular materials, the characteristic rapidly increasing then saturating charging of the system has been obtained in the numerical simulations. The final charge is controlled by the density of donors that limits the maximum number of charge transfers in the system. In bi-disperse granular materials, large particles could charge either positively or negatively while smaller ones charge negatively or positively depending on the density of donors. The positive charging of large particles observed in nature and experiments could be reproduced if there are less

donor than acceptor patches on the particles. Once again, as the density of donors limits the maximum number of charge transfers, the charging could be explained by this parameter. Finally, different materials tribocharging has been reproduced by placing patches on the container. I showed that the difference between the densities of donor patches on the particles and on the container defines the net charge of granular materials. If the density of donor patches on the particles is larger, then granular materials charge positively but if it is smaller than the density of donor patches on the container, it charges negatively. Numerical simulations with inclined tubes also provided results consistent with similar experiments that showed the influence of the angle of the tube.

Considering the various similarities between the numerical simulations and the experiments on tribocharging, it can be assumed that the patch model I use in the simulations correctly reproduces the tribocharging of granular materials and is validated. To potentially show that cohesion originates from the triboelectric effect, the flow of tribocharged granular materials has been investigated. By measuring the fluctuations of the interface, it has been shown that granular materials are indeed cohesive when the patches on the particles are charged. As the charge of the particles depend on the density of donor patches and the quantity of charge exchanged at contact, cohesion is also influenced by these same parameters. Moreover, I have shown that if the size of the particles is decreased, cohesion is also larger as cohesive forces remain constant while the weight of the particles decreases.

It is believed – but still under debate – that the transfer of charges from a donor patch to an acceptor patch could be explained by a transfer of negative ions that are contained in water from a wet patch to a dry patch. The mechanism of charge transfer in the numerical simulations has been implemented so that it is consistent with this transfer of ions from wet to dry patch. Donor patches in the simulations could thus be considered as wet patches while acceptor patches are dry patches. Humidity could then influence the density of donor patches and could thus be directly related to this parameter. Keeping this analogy in mind, the results I obtained suggest that

1. humidity controls the charging of mono-disperse granular materials as the

charge depends on the density of donors. As the presence of electrostatic charges on the particles because of the triboelectric effect induces cohesion, humidity influences cohesion through the triboelectric effect,

2. in bi-disperse granular materials, if particles are covered over less than 50% of their surface area with water patches, then large particles will charge positively while smaller ones charge negatively, as observed in nature and experiments,
3. granular materials acquire in average a non-zero global net charge if the particles have been in contact with a container made of a different material that has a different hydrophobicity than the material of the particles. If the container's material is more hydrophobic, granular materials charge positively but if it less hydrophobic than the particles' material, they charge negatively in average.

In addition to showing the relation between electrostatic charges in granular materials and their cohesion, these results bring new insights into the current active debate concerning the triboelectric effect. Considering the strong consistency between the numerical simulations with the patch model and the experiments, this model now significantly stands out. However, even though some studies have shown the presence of island-like water patches at the surface of objects, no studies relating the distribution of these water patches and materials tribocharging has been performed yet. As the numerical simulations with the patch model provide a rational explanation to the charging of granular materials, if their existence can be proven, then the debate on the triboelectric effect could be closed. In the mean time, the versatility of the numerical simulations could allow to analyze the tribocharging of granular materials in many other system than the rotating drum like granular gases in microgravity or in silos.

---

# References

---

- [1] Heinrich M Jaeger, Sidney R Nagel, and Robert P Behringer. The physics of granular materials. *Physics today*, 49(4):32–38, 1996.
- [2] Pierre-Gilles de Gennes. Granular matter: a tentative view. *Reviews of modern physics*, 71(2):S374, 1999.
- [3] Duane Roller and Duane HD Roller. The prenatal history of electrical science. *American Journal of Physics*, 21(5):343–356, 1953.
- [4] Paul Iversen and Daniel J Lacks. A life of its own: The tenuous connection between thales of miletus and the study of electrostatic charging. *Journal of Electrostatics*, 70(3):309–311, 2012.
- [5] Silvanus Phillips Thompson. *Elementary lessons in electricity and magnetism*. Macmillan, 1921.
- [6] Bern Dibner. Ten founding fathers of the electrical science: li. otto von guericke: And the first electric machine. *Electrical Engineering*, 73(5):396–397, 1954.
- [7] SPARKMUSEUM. Two Kinds of Electrical Fluid: Vitreous and Resinous - 1733. [http://www.sparkmuseum.com/BOOK\\_DUFAY.HTM](http://www.sparkmuseum.com/BOOK_DUFAY.HTM). [Online; accessed 14-November-2023].

## REFERENCES

---

- [8] IOP Resources. Electricity and Magnetism - The two electric fluids. <https://spark.iop.org/two-electric-fluids#:~:text=From%20these%20observations%2C%20Du%20Fay,and%20neutralised%20when%20they%20recombined.> [Online; accessed 14-November-2023].
- [9] Roderick W Home. Franklin's electrical atmospheres. *The British Journal for the History of Science*, 6(2):131–151, 1972.
- [10] Peter E Shaw. The electrical charges from like solids. *Nature*, 118(2975):659–660, 1926.
- [11] Peter E Shaw. Experiments on tribo-electricity. i.—the tribo-electric series. *Proceedings of the Royal Society of London. Series A, Containing Papers of a Mathematical and Physical Character*, 94(656):16–33, 1917.
- [12] PSH Henry. The role of asymmetric rubbing in the generation of static electricity. *British Journal of Applied Physics*, 4(S2):S31, 1953.
- [13] GD Freier. The electric field of a large dust devil. *Journal of Geophysical Research*, 65(10):3504–3504, 1960.
- [14] WD Crozier. The electric field of a new mexico dust devil. *Journal of Geophysical Research*, 69(24):5427–5429, 1964.
- [15] Richard Giles Harrison, KA Nicoll, Z Ulanowski, and TA Mather. Self-charging of the eyjafjallajökull volcanic ash plume. *Environmental Research Letters*, 5(2):024004, 2010.
- [16] Corrado Cimorelli, Sonja Behnke, Kimberly Genareau, Joshua Méndez Harper, and Alexa R Van Eaton. Volcanic electrification: recent advances and future perspectives. *Bulletin of Volcanology*, 84(8):78, 2022.
- [17] Joshua Méndez Harper, Corrado Cimorelli, Valeria Cigala, Ulrich Kueppers, and Josef Dufek. Charge injection into the atmosphere by explosive volcanic eruptions through triboelectrification and fragmentation charging. *Earth and Planetary Science Letters*, 574:117162, 2021.
- [18] John R Leeman and Ernst D Schmitter. Electric signals generated by tornados. *Atmospheric research*, 92(2):277–279, 2009.

- [19] Mihai A Bilici, Joseph R Toth, R Mohan Sankaran, and Daniel J Lacks. Particle size effects in particle-particle triboelectric charging studied with an integrated fluidized bed and electrostatic separator system. *Review of Scientific Instruments*, 85(10), 2014.
- [20] Scott R Waitukaitis, Victor Lee, James M Pierson, Steven L Forman, and Heinrich M Jaeger. Size-dependent same-material tribocharging in insulating grains. *Physical Review Letters*, 112(21):218001, 2014.
- [21] Joseph R Toth III, Amber K Phillips, Siddharth Rajupet, R Mohan Sankaran, and Daniel J Lacks. Particle-size-dependent triboelectric charging in single-component granular materials: role of humidity. *Industrial & Engineering Chemistry Research*, 56(35):9839–9845, 2017.
- [22] Keith M Forward, Daniel J Lacks, and R Mohan Sankaran. Charge segregation depends on particle size in triboelectrically charged granular materials. *Physical review letters*, 102(2):028001, 2009.
- [23] Huiliang Zhao, GS Peter Castle, and Ion I Inculet. The measurement of bipolar charge in polydisperse powders using a vertical array of faraday pail sensors. *Journal of electrostatics*, 55(3-4):261–278, 2002.
- [24] Daniel J Lacks and Troy Shinbrot. Long-standing and unresolved issues in triboelectric charging. *Nature Reviews Chemistry*, 3(8):465–476, 2019.
- [25] Daniel J Lacks, Nathan Duff, and Sanat K Kumar. Nonequilibrium accumulation of surface species and triboelectric charging in single component particulate systems. *Physical review letters*, 100(18):188305, 2008.
- [26] John Turton Randall and Maurice Hugh Frederick Wilkins. Phosphorescence and electron traps ii. the interpretation of long-period phosphorescence. *Proceedings of the Royal Society of London. Series A. Mathematical and Physical Sciences*, 184(999):390–407, 1945.
- [27] J Lowell and WS Truscott. Triboelectrification of identical insulators. ii. theory and further experiments. *Journal of Physics D: Applied Physics*, 19(7):1281, 1986.

- [28] Daniel J Lacks and Artem Levandovsky. Effect of particle size distribution on the polarity of triboelectric charging in granular insulator systems. *Journal of Electrostatics*, 65(2):107–112, 2007.
- [29] Nathan Duff and Daniel J Lacks. Particle dynamics simulations of triboelectric charging in granular insulator systems. *Journal of Electrostatics*, 66(1-2):51–57, 2008.
- [30] Daniel J Lacks and R Mohan Sankaran. Contact electrification of insulating materials. *Journal of Physics D: Applied Physics*, 44(45):453001, 2011.
- [31] H Tarik Baytekin, Alexander Z Patashinski, M Branicki, Bilge Baytekin, S Soh, and Bartosz A Grzybowski. The mosaic of surface charge in contact electrification. *Science*, 333(6040):308–312, 2011.
- [32] Melissa Braga, Carlos Alberto Rodrigues Costa, Carlos Alberto Paula Leite, and Fernando Galembeck. Scanning electric potential microscopy imaging of polymer latex films: detection of supramolecular domains with nonuniform electrical characteristics. *The Journal of Physical Chemistry B*, 105(15):3005–3011, 2001.
- [33] Thiago AL Burgo, Telma RD Ducati, Kelly R Francisco, Karl J Clinckspoor, Fernando Galembeck, and Sergio E Galembeck. Triboelectricity: macroscopic charge patterns formed by self-arraying ions on polymer surfaces. *Langmuir*, 28(19):7407–7416, 2012.
- [34] Felix Pertl, Juan Carlos Sobarzo, Lubuna Shafeek, Tobias Cramer, and Scott Waitukaitis. Quantifying nanoscale charge density features of contact-charged surfaces with an fem/kpfm-hybrid approach. *Physical Review Materials*, 6(12):125605, 2022.
- [35] Troy Shinbrot, Teruhisa S Komatsu, and Q Zhao. Spontaneous tribocharging of similar materials. *Europhysics Letters*, 83(2):24004, 2008.
- [36] Yaroslav I Sobolev, Witold Adamkiewicz, Marta Siek, and Bartosz A Grzybowski. Charge mosaics on contact-electrified dielectrics result from polarity-inverting discharges. *Nature Physics*, 18(11):1347–1355, 2022.



- [37] Tobias Steinpilz, Felix Jungmann, Kolja Joeris, Jens Teiser, and Gerhard Wurm. Measurements of dipole moments and a q-patch model of collisionally charged grains. *New Journal of Physics*, 22(9):093025, 2020.
- [38] Mario M Apodaca, Paul J Wesson, Kyle JM Bishop, Mark A Ratner, and Bartosz A Grzybowski. Contact electrification between identical materials. *Angewandte Chemie International Edition*, 49(5):946–949, 2010.
- [39] Galien Grosjean, Sebastian Wald, Juan Carlos Sobarzo, and Scott Waitukaitis. Quantitatively consistent scale-spanning model for same-material tribocharging. *Physical Review Materials*, 4(8):082602, 2020.
- [40] Galien Grosjean and Scott Waitukaitis. Asymmetries in triboelectric charging: Generalizing mosaic models to different-material samples and sliding contacts. *Physical Review Materials*, 7(6):065601, 2023.
- [41] Shuji Matsusaka, Mojtaba Ghadiri, and Hiroaki Masuda. Electrification of an elastic sphere by repeated impacts on a metal plate. *Journal of Physics D: Applied Physics*, 33(18):2311, 2000.
- [42] Mamadou Sow, Ross Widenor, Ajay Kumar, Seung Whan Lee, Daniel J Lacks, and R Mohan Sankaran. Strain-induced reversal of charge transfer in contact electrification. *Angewandte Chemie*, 124(11):2749–2751, 2012.
- [43] Mamadou Sow, Daniel J Lacks, and R Mohan Sankaran. Dependence of contact electrification on the magnitude of strain in polymeric materials. *Journal of Applied Physics*, 112(8), 2012.
- [44] Andrew E Wang, Phwey S Gil, Moses Holonga, Zelal Yavuz, H Tarik Baytekin, R Mohan Sankaran, and Daniel J Lacks. Dependence of triboelectric charging behavior on material microstructure. *Physical Review Materials*, 1(3):035605, 2017.
- [45] Thiago AL Burgo, Bruno C Batista, and Fernando Galembeck. Electricity on rubber surfaces: a new energy conversion effect. *ACS omega*, 2(12):8940–8947, 2017.
- [46] Leandra P Santos, Yan AS Campo, Douglas S Da Silva, Thiago AL Burgo, and Fernando Galembeck. Rubber surface change and static charging under periodic stress. *Colloids and Interfaces*, 2(4):55, 2018.

- [47] Logan S McCarty and George M Whitesides. Electrostatic charging due to separation of ions at interfaces: contact electrification of ionic electrets. *Angewandte Chemie International Edition*, 47(12):2188–2207, 2008.
- [48] Victor Lee, Nicole M James, Scott R Waitukaitis, and Heinrich M Jaeger. Collisional charging of individual submillimeter particles: Using ultrasonic levitation to initiate and track charge transfer. *Physical Review Materials*, 2(3):035602, 2018.
- [49] André Schella, Stephan Herminghaus, and Matthias Schröter. Influence of humidity on tribo-electric charging and segregation in shaken granular media. *Soft matter*, 13(2):394–401, 2017.
- [50] Ke Xu, Peigen Cao, and James R Heath. Graphene visualizes the first water adlayers on mica at ambient conditions. *Science*, 329(5996):1188–1191, 2010.
- [51] Galien Grosjean and Scott Waitukaitis. Single-collision statistics reveal a global mechanism driven by sample history for contact electrification in granular media. *Physical Review Letters*, 130(9):098202, 2023.
- [52] Antonella Rescaglio, Julien Schockmel, Nicolas Vandewalle, and Geoffroy Lumay. Combined effect of moisture and electrostatic charges on powder flow. In *EPJ Web of Conferences*, volume 140, page 13009. EDP Sciences, 2017.
- [53] Isaac A Harris, Melody X Lim, and Heinrich M Jaeger. Temperature dependence of nylon and ptfe triboelectrification. *Physical Review Materials*, 3(8):085603, 2019.
- [54] Ignaas SM Jimidar, Wojciech Kwiecinski, Gijs Roozendaal, E Stefan Kooij, Han JGE Gardeniers, Gert Desmet, and Kai Sotthewes. Influence of wettability and geometry on contact electrification between nonionic insulators. *ACS applied materials & interfaces*, 15(35):42004–42014, 2023.
- [55] H.A. Janssen. Experiments on corn pressure in silo cells. *Zeitschrift der Vereines Deutsches Ingenieure*, 39:1045, 1895.

- 
- [56] Matthias Sperl. Experiments on corn pressure in silo cells—translation and comment of janssen’s paper from 1895. *Granular Matter*, 8(2):59–65, 2006.
- [57] Yann Bertho, Frédérique Giorgiutti-Dauphiné, and Jean-Pierre Hulin. Dynamical janssen effect on granular packing with moving walls. *Physical Review Letters*, 90(14):144301, 2003.
- [58] CRK Windows-Yule, Sebastian Mühlbauer, LA Torres Cisneros, P Nair, V Marzulli, and T Pöschel. Janssen effect in dynamic particulate systems. *Physical Review E*, 100(2):022902, 2019.
- [59] Trushant S Majmudar and Robert P Behringer. Contact force measurements and stress-induced anisotropy in granular materials. *Nature*, 435(7045):1079–1082, 2005.
- [60] Martin Van Hecke. A tale of tails. *Nature*, 435(7045):1041–1042, 2005.
- [61] David Fischer, Ralf Stannarius, Karsten Tell, Peidong Yu, and Matthias Sperl. Force chains in crystalline and frustrated packing visualized by stress-birefringent spheres. *Soft Matter*, 17(16):4317–4327, 2021.
- [62] Alexandra L Thomas and Nathalie M Vriend. Photoelastic study of dense granular free-surface flows. *Physical Review E*, 100(1):012902, 2019.
- [63] Osborne Reynolds. Lvii. on the dilatancy of media composed of rigid particles in contact. with experimental illustrations. *The London, Edinburgh, and Dublin Philosophical Magazine and Journal of Science*, 20(127):469–481, 1885.
- [64] Emilien Azema, Farhang Radjai, and Jean-Noël Roux. Internal friction and absence of dilatancy of packings of frictionless polygons. *Physical Review E*, 91(1):010202, 2015.
- [65] Frédéric Da Cruz, Sacha Emam, Michaël Prochnow, Jean-Noël Roux, and François Chevoir. Rheophysics of dense granular materials: Discrete simulation of plane shear flows. *Physical Review E*, 72(2):021309, 2005.
- [66] Geoffroy Lumay and Nicolas Vandewalle. Experimental study of granular compaction dynamics at different scales: grain mobility, hexagonal domains, and packing fraction. *Physical review letters*, 95(2):028002, 2005.

## REFERENCES

---

- [67] Salvatore Pillitteri, Geoffroy Lumay, Eric Opsomer, and Nicolas Vandewalle. From jamming to fast compaction dynamics in granular binary mixtures. *Scientific Reports*, 9(1):7281, 2019.
- [68] Salvatore Pillitteri, Eric Opsomer, Geoffroy Lumay, and Nicolas Vandewalle. How size ratio and segregation affect the packing of binary granular mixtures. *Soft Matter*, 16(39):9094–9100, 2020.
- [69] Ishan Prasad, Christian Santangelo, and Gregory Grason. Subjamming transition in binary sphere mixtures. *Physical Review E*, 96(5):052905, 2017.
- [70] James B Knight, Christopher G Fandrich, Chun Ning Lau, Heinrich M Jaeger, and Sidney R Nagel. Density relaxation in a vibrated granular material. *Physical review E*, 51(5):3957, 1995.
- [71] P Philippe and D Bideau. Compaction dynamics of a granular medium under vertical tapping. *Europhysics Letters*, 60(5):677, 2002.
- [72] ER Nowak, JB Knight, ML Povinelli, HM Jaeger, and SR Nagel. Reversibility and irreversibility in the packing of vibrated granular material. *Powder technology*, 94(1):79–83, 1997.
- [73] Troy Shinbrot. The brazil nut effect—in reverse. *Nature*, 429(6990):352–353, 2004.
- [74] Anthony Rosato, Katherine J Strandburg, Friedrich Prinz, and Robert H Swendsen. Why the brazil nuts are on top: Size segregation of particulate matter by shaking. *Physical review letters*, 58(10):1038, 1987.
- [75] J Duran, J Rajchenbach, and E Clément. Arching effect model for particle size segregation. *Physical review letters*, 70(16):2431, 1993.
- [76] James B Knight, Heinrich M Jaeger, and Sidney R Nagel. Vibration-induced size separation in granular media: The convection connection. *Physical review letters*, 70(24):3728, 1993.
- [77] Matthias E Möbius, Benjamin E Lauderdale, Sidney R Nagel, and Heinrich M Jaeger. Size separation of granular particles. *Nature*, 414(6861):270–270, 2001.

- 
- [78] Abhinendra Singh, Vanessa Magnanimo, Kuniyasu Saitoh, and Stefan Luding. Effect of cohesion on shear banding in quasistatic granular materials. *Physical Review E*, 90(2):022202, 2014.
- [79] Runyu Y Yang, AB Yu, Luke McElroy, and Jie Bao. Numerical simulation of particle dynamics in different flow regimes in a rotating drum. *Powder Technology*, 188(2):170–177, 2008.
- [80] Nicolas Vandewalle, Geoffroy Lumay, O Gerasimov, and François Ludewig. The influence of grain shape, friction and cohesion on granular compaction dynamics. *The European Physical Journal E*, 22:241–248, 2007.
- [81] Peter K Haff. Grain flow as a fluid-mechanical phenomenon. *Journal of Fluid Mechanics*, 134:401–430, 1983.
- [82] Bruno Andreotti, Yoël Forterre, and Olivier Pouliquen. *Les milieux granulaires*. EDP Sciences, 2011.
- [83] Isaac Goldhirsch. Rapid granular flows. *Annual review of fluid mechanics*, 35(1):267–293, 2003.
- [84] E Falcon, S Fauve, and C Laroche. Cluster formation, pressure and density measurements in a granular medium fluidized by vibrations. *The European Physical Journal B-Condensed Matter and Complex Systems*, 9(2):183–186, 1999.
- [85] Eric Opsomer, F Ludewig, and N Vandewalle. Phase transitions in vibrated granular systems in microgravity. *Physical Review E*, 84(5):051306, 2011.
- [86] Martial Noirhomme, Annette Cazaubiel, Alexis Darras, Eric Falcon, David Fischer, Yves Garrabos, Carole Lecoutre-Chabot, Simon Merminod, Eric Opsomer, Fabien Palencia, et al. Threshold of gas-like to clustering transition in driven granular media in low-gravity environment. *Europhysics Letters*, 123(1):14003, 2018.
- [87] Jens Teiser, Maximilian Kruss, Felix Jungmann, and Gerhard Wurm. A smoking gun for planetesimal formation: charge-driven growth into a new size range. *The Astrophysical Journal Letters*, 908(2):L22, 2021.

- [88] Chamkor Singh and Marco G Mazza. Early-stage aggregation in three-dimensional charged granular gas. *Physical Review E*, 97(2):022904, 2018.
- [89] T Scheffler and DE Wolf. Collision rates in charged granular gases. *Granular Matter*, 4(3):103–113, 2002.
- [90] Yoël Forterre and Olivier Pouliquen. Flows of dense granular media. *Annu. Rev. Fluid Mech.*, 40:1–24, 2008.
- [91] Pierre Jop, Yoël Forterre, and Olivier Pouliquen. A constitutive law for dense granular flows. *Nature*, 441(7094):727–730, 2006.
- [92] GDR MiDi. On dense granular flows. *The European Physical Journal E*, 14:341–365, 2004.
- [93] L Staron, P Y Lagrée, and S Popinet. Continuum simulation of the discharge of the granular silo: a validation test for the  $\mu(i)$  visco-plastic flow law. *The European Physical Journal E*, 37:1–12, 2014.
- [94] Kiwing To, Pik-Yin Lai, and HK Pak. Jamming of granular flow in a two-dimensional hopper. *Physical review letters*, 86(1):71, 2001.
- [95] Iker Zuriguel, Angel Garcimartín, Diego Maza, Luis A Pugnaloni, and JM Pastor. Jamming during the discharge of granular matter from a silo. *Physical Review E*, 71(5):051303, 2005.
- [96] A Janda, Iker Zuriguel, A Garcimartín, Luis A Pugnaloni, and Diego Maza. Jamming and critical outlet size in the discharge of a two-dimensional silo. *Europhysics Letters*, 84(4):44002, 2008.
- [97] Andrea J Liu and Sidney R Nagel. Jamming is not just cool any more. *Nature*, 396(6706):21–22, 1998.
- [98] Stéphane Dorbolo, Laurent Maquet, Martin Brandenbourger, François Ludewig, Geoffroy Lumay, Hervé Caps, Nicolas Vandewalle, Samuel Rondia, Médéric Mélard, JJWA van Loon, et al. Influence of the gravity on the discharge of a silo. *Granular Matter*, 15:263–273, 2013.

- 
- [99] Dust Safety Science. Incident Database. <https://dustsafetyscience.com/category/incidents/>. [Online; accessed 25-January-2024].
- [100] Martin Glor. Hazards due to electrostatic charging of powders. *Journal of electrostatics*, 16(2-3):175–191, 1985.
- [101] Olivier Pouliquen and Nathalie Renaut. Onset of granular flows on an inclined rough surface: dilatancy effects. *Journal de Physique II*, 6(6):923–935, 1996.
- [102] Leonardo E Silbert, Deniz Ertaş, Gary S Grest, Thomas C Halsey, Dov Levine, and Steven J Plimpton. Granular flow down an inclined plane: Bagnold scaling and rheology. *Physical Review E*, 64(5):051302, 2001.
- [103] Richard M Iverson and Roger P Denlinger. Flow of variably fluidized granular masses across three-dimensional terrain: 1. coulomb mixture theory. *Journal of Geophysical Research: Solid Earth*, 106(B1):537–552, 2001.
- [104] Richard M Iverson and David L George. A depth-averaged debris-flow model that includes the effects of evolving dilatancy. i. physical basis. *Proceedings of the Royal Society A: Mathematical, Physical and Engineering Sciences*, 470(2170):20130819, 2014.
- [105] GB Crosta, S Imposimato, and DG Roddeman. Numerical modelling of large landslides stability and runout. *Natural Hazards and Earth System Sciences*, 3(6):523–538, 2003.
- [106] Peter M Ireland. Triboelectrification of particulate flows on surfaces: Part i—experiments. *Powder Technology*, 198(2):189–198, 2010.
- [107] Michael D Hogue, Carlos I Calle, DR Curry, and PS Weitzman. Discrete element modeling (dem) of triboelectrically charged particles: revised experiments. *Journal of Electrostatics*, 67(4):691–694, 2009.
- [108] Janne Peltonen, Matti Murtomaa, and Jarno Salonen. Measuring electrostatic charging of powders on-line during surface adhesion. *Journal of Electrostatics*, 93:53–57, 2018.
- [109] Shivangi Naik, Saurabh Sarkar, Vipul Gupta, Bruno C Hancock, Yuri Abramov, Weili Yu, and Bodhisattwa Chaudhuri. A combined experimental

## REFERENCES

---

- and numerical approach to explore tribocharging of pharmaceutical excipients in a hopper chute assembly. *International journal of pharmaceutics*, 491(1-2):58–68, 2015.
- [110] Peter M Ireland. Dynamic particle-surface tribocharging: The role of shape and contact mode. *Journal of Electrostatics*, 70(6):524–531, 2012.
- [111] Mathieu Renouf, Daniel Bonamy, Frédéric Dubois, and Pierre Alart. Numerical simulation of two-dimensional steady granular flows in rotating drum: On surface flow rheology. *Physics of fluids*, 17(10), 2005.
- [112] Ashish V Orpe and DV Khakhar. Rheology of surface granular flows. *Journal of Fluid Mechanics*, 571:1–32, 2007.
- [113] Ashish V Orpe and DV Khakhar. Solid-fluid transition in a granular shear flow. *Physical review letters*, 93(6):068001, 2004.
- [114] Eric Clement, Jean Rajchenbach, and Jacques Duran. Mixing of a granular material in a bidimensional rotating drum. *Europhysics Letters*, 30(1):7, 1995.
- [115] F Cantelaube and D Bideau. Radial segregation in a 2d drum: an experimental analysis. *Europhysics Letters*, 30(3):133, 1995.
- [116] Nitin Jain, Julio M Ottino, and Richard M Lueptow. An experimental study of the flowing granular layer in a rotating tumbler. *Physics of Fluids*, 14(2):572–582, 2002.
- [117] DJ Parker, AE Dijkstra, TW Martin, and JPK Seville. Positron emission particle tracking studies of spherical particle motion in rotating drums. *Chemical Engineering Science*, 52(13):2011–2022, 1997.
- [118] S-Y Lim, JF Davidson, RN Forster, DJ Parker, DM Scott, and JPK Seville. Avalanching of granular material in a horizontal slowly rotating cylinder: Pept studies. *Powder Technology*, 138(1):25–30, 2003.
- [119] Christian M Dury, Gerald H Ristow, Jamie L Moss, and Masami Nakagawa. Boundary effects on the angle of repose in rotating cylinders. *Physical Review E*, 57(4):4491, 1998.



- [120] Masami Nakagawa, Stephen A Altobelli, Arvind Caprihan, E Fukushima, and E K Jeong. Non-invasive measurements of granular flows by magnetic resonance imaging. *Experiments in fluids*, 16:54–60, 1993.
- [121] Akwase A Boateng and Peter V Barr. Granular flow behaviour in the transverse plane of a partially filled rotating cylinder. *Journal of Fluid Mechanics*, 330:233–249, 1997.
- [122] Nicolas Taberlet, Patrick Richard, and E John Hinch. S shape of a granular pile in a rotating drum. *Physical Review E*, 73(5):050301, 2006.
- [123] Nicholas A Pohlman, Julio M Ottino, and Richard M Lueptow. End-wall effects in granular tumblers: From quasi-two-dimensional flow to three-dimensional flow. *Physical review E*, 74(3):031305, 2006.
- [124] Nicholas A Pohlman, Steven W Meier, Richard M Lueptow, and Julio M Ottino. Surface velocity in three-dimensional granular tumblers. *Journal of Fluid Mechanics*, 560:355–368, 2006.
- [125] Pengfei Chen, Julio M Ottino, and Richard M Lueptow. Subsurface granular flow in rotating tumblers: A detailed computational study. *Physical Review E*, 78(2):021303, 2008.
- [126] Geoffroy Lumay, Frédéric Boschini, Karl Traina, Sébastien Bontempi, J-C Remy, R Cloots, and N Vandewalle. Measuring the flowing properties of powders and grains. *Powder technology*, 224:19–27, 2012.
- [127] Hani Henein, James K Brimacombe, and Alan P Watkinson. Experimental study of transverse bed motion in rotary kilns. *Metallurgical transactions B*, 14:191–205, 1983.
- [128] Jochen Mellmann. The transverse motion of solids in rotating cylinders—forms of motion and transition behavior. *Powder technology*, 118(3):251–270, 2001.
- [129] Daniel Bonamy, F Daviaud, and L Laurent. Experimental study of granular surface flows via a fast camera: a continuous description. *Physics of fluids*, 14(5):1666–1673, 2002.

## REFERENCES

---

- [130] S Longo and A Lamberti. Grain shear flow in a rotating drum. *Experiments in Fluids*, 32(3):313–325, 2002.
- [131] Ashish V Orpe and DV Khakhar. Scaling relations for granular flow in quasi-two-dimensional rotating cylinders. *Physical review E*, 64(3):031302, 2001.
- [132] Xiao Yan Liu, Eckehard Specht, and Jochen Mellmann. Experimental study of the lower and upper angles of repose of granular materials in rotating drums. *Powder Technology*, 154(2-3):125–131, 2005.
- [133] Nicholas A Pohlman, Benjamin L Severson, Julio M Ottino, and Richard M Lueptow. Surface roughness effects in granular matter: Influence on angle of repose and the absence of segregation. *Physical Review E*, 73(3):031304, 2006.
- [134] Jean Rajchenbach. Flow in powders: From discrete avalanches to continuous regime. *Physical Review Letters*, 65(18):2221, 1990.
- [135] Daniel J Hornbaker, Réka Albert, István Albert, A-L Barabási, and Peter Schiffer. What keeps sandcastles standing? *Nature*, 387(6635):765–765, 1997.
- [136] JE Fiscina, Geoffroy Lumay, François Ludewig, and Nicolas Vandewalle. Compaction dynamics of wet granular assemblies. *Physical review letters*, 105(4):048001, 2010.
- [137] Ahmed Jarray, Vanessa Magnanimo, Marco Ramaioli, and Stefan Luding. Scaling of wet granular flows in a rotating drum. In *EPJ web of conferences*, volume 140, page 03078. EDP Sciences, 2017.
- [138] Ahmed Jarray, Hao Shi, Bert J Scheper, Mehdi Habibi, and Stefan Luding. Cohesion-driven mixing and segregation of dry granular media. *Scientific reports*, 9(1):13480, 2019.
- [139] Arshad Kudrolli. Sticky sand. *Nature materials*, 7(3):174–175, 2008.
- [140] Albert W Alexander, Bodhisattwa Chaudhuri, AbdulMobeen Faqih, Fernando J Muzzio, Clive Davies, and M Silvina Tomassone. Avalanching flow of cohesive powders. *Powder Technology*, 164(1):13–21, 2006.

- [141] P Tegzes, T Vicsek, and P Schiffer. Avalanche dynamics in wet granular materials. *Physical review letters*, 89(9):094301, 2002.
- [142] Peiyuan Liu, Casey Q LaMarche, Kevin M Kellogg, Stuart Leadley, and Christine M Hrenya. Cohesive grains: bridging microlevel measurements to macrolevel flow behavior via surface roughness. *AIChE Journal*, 62(10):3529–3537, 2016.
- [143] Antonio Castellanos. The relationship between attractive interparticle forces and bulk behaviour in dry and uncharged fine powders. *Advances in physics*, 54(4):263–376, 2005.
- [144] Hao Shi, Sudeshna Roy, Thomas Weinhart, Vanessa Magnanimo, and Stefan Luding. Steady state rheology of homogeneous and inhomogeneous cohesive granular materials. *Granular matter*, 22:1–20, 2020.
- [145] Adam J Forsyth, SR Hutton, Martin J Rhodes, and Charles F Osborne. Effect of applied interparticle force on the static and dynamic angles of repose of spherical granular material. *Physical Review E*, 63(3):031302, 2001.
- [146] Adam J Forsyth, S Hutton, and Martin J Rhodes. Effect of cohesive interparticle force on the flow characteristics of granular material. *Powder Technology*, 126(2):150–154, 2002.
- [147] Geoffroy Lumay and Nicolas Vandewalle. Flow of magnetized grains in a rotating drum. *Physical Review E*, 82(4):040301, 2010.
- [148] Antonio Castellanos, José Manuel Valverde, Alberto T Pérez, Antonio Ramos, and P Keith Watson. Flow regimes in fine cohesive powders. *Physical review letters*, 82(6):1156, 1999.
- [149] Tobias Kronlachner, Stefan Pirker, and Thomas Lichtenegger. A block-movement-based analysis for cohesive powders in a rotating drum experiment. *Powder Technology*, 399:117209, 2022.
- [150] Robert Brewster, Gary S Grest, and Alex J Levine. Effects of cohesion on the surface angle and velocity profiles of granular material in a rotating drum. *Physical Review E*, 79(1):011305, 2009.

- [151] M Wojtkowski, Ol Imole, M Ramaioli, E Chávez Montes, and S Luding. Behavior of cohesive powder in rotating drums. *AIP Conference Proceedings*, 1542(1):983–986, 2013.
- [152] ERL Espiritu, A Kumar, A Nommeots-Nomm, JA Muñiz Lerma, and M Brochu. Investigation of the rotating drum technique to characterise powder flow in controlled and low pressure environments. *Powder Technology*, 366:925–937, 2020.
- [153] Hongming Li and JJ McCarthy. Controlling cohesive particle mixing and segregation. *Physical review letters*, 90(18):184301, 2003.
- [154] Peter A Cundall and Otto DL Strack. A discrete numerical model for granular assemblies. *Geotechnique*, 29(1):47–65, 1979.
- [155] Farhang Radjai and Frédéric Dubois. *Discrete-element modeling of granular materials*. Wiley-Iste, 2011.
- [156] J Schäfer, S Dippel, and DE Wolf. Force schemes in simulations of granular materials. *Journal de physique I*, 6(1):5–20, 1996.
- [157] Cecily Sunday, Naomi Murdoch, Simon Tardivel, Stephen R Schwartz, and Patrick Michel. Validating n-body code chrono for granular dem simulations in reduced-gravity environments. *Monthly Notices of the Royal Astronomical Society*, 498(1):1062–1079, 2020.
- [158] Atsuyuki Okabe, Barry Boots, Kokichi Sugihara, and Sung Nok Chiu. *Spatial tessellations: concepts and applications of Voronoi diagrams*. John Wiley & Sons, 2009.
- [159] Wolfram Research, Inc. Mathematica, Version 13.0. Champaign, IL, 2024.
- [160] Ganna Yablokova, Mathew Speirs, Jan Van Humbeeck, J-P Kruth, J Schrooten, Rudi Cloots, Frédéric Boschini, Geoffroy Lumay, and Jan Luyten. Rheological behavior of  $\beta$ -ti and niti powders produced by atomization for slm production of open porous orthopedic implants. *Powder Technology*, 283:199–209, 2015.

- 
- [161] Guang Lu, JR Third, and CR Müller. Discrete element models for non-spherical particle systems: From theoretical developments to applications. *Chemical Engineering Science*, 127:425–465, 2015.
- [162] François Ludewig and N Vandewalle. Strong interlocking of nonconvex particles in random packings. *Physical Review E*, 85(5):051307, 2012.
- [163] Olivier Dubé, Ebrahim Alizadeh, Jamal Chaouki, and François Bertrand. Dynamics of non-spherical particles in a rotating drum. *Chemical Engineering Science*, 101:486–502, 2013.
- [164] Nan Gui, Xingtuan Yang, Jiyuan Tu, Shengyao Jiang, and Zhen Zhang. Numerical simulation of tetrahedral particle mixing and motion in rotating drums. *Particuology*, 39:1–11, 2018.
- [165] Dyrney A Santos, Marcos AS Barrozo, Claudio R Duarte, Fabian Weigler, and Jochen Mellmann. Investigation of particle dynamics in a rotary drum by means of experiments and numerical simulations using dem. *Advanced Powder Technology*, 27(2):692–703, 2016.
- [166] Domink Höhner, Siegmund Wirtz, and Viktor Scherer. A study on the influence of particle shape and shape approximation on particle mechanics in a rotating drum using the discrete element method. *Powder Technology*, 253:256–265, 2014.
- [167] J Olson, M Priester, J Luo, S Chopra, and RJ Zieve. Packing fractions and maximum angles of stability of granular materials. *Physical Review E*, 72(3):031302, 2005.

